Rapid Detection and Accurate Discrimination of Microorganisms by Liquid Chromatography, High-Resolution Ion Mobility, and Tandem Mass Spectrometry

by

Orobola Emmanuel Olajide

A dissertation submitted to the Graduate Faculty of
Auburn University
in partial fulfillment of the
requirements for the Degree of
Doctor of Philosophy

Auburn, Alabama
May 4, 2024

Keywords: Ion Mobility Spectrometry, Collision cross section measurements, Ambient ionization, Bacterial discrimination, Multidimensional separation techniques

Approved by

Ahmed M. Hamid, Chair, Assistant Professor, Dept. of Chemistry & Biochemistry
Christopher J. Easley, Dr. & Mrs. Charles Dent Williams Professor, Dept. of Chemistry& Biochemistry
Steven Mansoorabadi, J. Milton Harris Associate Professor, Dept. of Chemistry & Biochemistry
Angela Calderón, Gilliland Professor, Dept. of Drug Discovery & Development
Jingyi Zheng, Assistant Professor, Dept. of Mathematics & Statistics

Abstract

Determining bacterial identity at the strain level is crucial for public health to enable appropriate medical treatment and reduce hospitalization times and antibiotic resistance. To achieve this goal, we have reported the coupling of ambient ionization techniques with a commercial drift tube ion mobility mass spectrometer and demonstrated their ability to rapidly separate constitutional and geometric isomers. After successful rapid isomer separation, we investigated paper spray – IM – MS/MS to discriminate five *Bacillus* species. We optimized several parameters, such as the incubation time and the spray solvent. We found that a 4 h-incubation time is sufficient for detection and that isopropyl alcohol (IPA) gives a longer spray time and higher intensities of the observed biomarkers than methanol (MeOH, typical spray solvent in PS – MS experiments). Numerical multivariate statistics (principal component analysis followed by linear discriminant analysis) allowed discrimination at the species level with a prediction rate of 92.4 % and 97.6 % using the negative and positive ion information from PS – MS/MS, respectively. However, when including the corresponding drift times of the biomarkers, i.e. PS – IM – MS/MS, prediction rates of 99.7% and 100% were obtained using the negative and positive ion information, respectively. We attribute the improvement in prediction rates to the ability of IM separations to resolve isomers.

When analyzing seven *E. coli* strains by PS – IM – MS/MS, the prediction rate was 80.5% after numerical data fusion of negative and positive ion modes. Therefore, we combined liquid chromatography with IM – MS/MS as LC – IM - MS/MS to accurately discriminate the seven *E. coli* strains. Numerical multivariate statistics demonstrated the ability of this method to perform

strain-level discrimination with prediction rates of 96.1% and 100% using the negative and positive ion information, respectively. This work demonstrates the great potential to accurately detect pathogenic and antibiotic-resistant bacteria in agrochemical screening, disease diagnostics, etc. Moreover, this work can pave the way for developing standalone ion mobility spectrometers which can be used in several medical, environmental, and security applications.

Acknowledgments

Before I acknowledge my advisor and others who have contributed to my success, I would like to begin with my own quote: “No man is born with great worth, it is your choice to be great or not, and the price of greatness is hard work, discipline, consistency, patience, and focus. My difficult childhood and adolescence led me to strive for greatness academically with the main goal of advancing health equity through innovative analytical techniques. Hence, my undying passion for analytical chemistry, which led me to pursue a PhD in analytical chemistry.

As with any dissertation, I must take credit where credit is due. I would like to thank my supervisor, Dr. Ahmed Hamid, for the immeasurable support and guidance you have given me over the last few years, almost half a decade. Surprisingly, even though I had done my Masters in Analytical Chemistry in Nigeria, I was still very scared to go to a new laboratory, mainly because there were no senior students to guide me in the techniques. However, after showing interest in your lab, my confidence was boosted after you told me that you would operate the equipment yourself and teach me these techniques. I remember that we both solved the solvent contamination problem together by taking apart different parts of the instrument, from the UHPLC to the ion mobility funnels. I thank you for the trust you placed in me by sending me to various mass spectrometry training courses that solidified my knowledge of separation science and mass spectrometry. Most importantly, thank you for entrusting me with several projects over the past 4 years, such as isomer discrimination with paper spray – IM, species-level discrimination, bacterial strain level discrimination, Alzheimer’s projects (diagnosis and treatment), method development for pesticides and etodolac. It has been exhausting but incredibly rewarding and I feel very well

prepared for whatever the future holds. I cannot stress enough how good it was to have the freedom and space to learn the tools and concepts I needed to be successful in this program. Attending various conferences such as the American Society of Mass Spectrometry (ASMS), the Pittcon conference, the National Organization for the Professional Advancement of Black Chemists and Chemical Engineers (NOBCChE), and SERMACS has strengthened my view of science after intellectual discussions with other graduate students, post-docs, and distinguished scientists from academia and industry. Your support is immeasurable, even outside of academia. You have given me numerous recommendations that have led to several awards, including Outstanding International Student, Auburn University. Your advice and unwavering support were instrumental in getting my EB2 National Interest Waiver approved for my permanent residency in the United States. I am very proud to be your first doctoral student, and I firmly believe that other students like me have chosen a great mentor to guide them on their path to a doctorate.

I am equally grateful to my committee members Dr. Christopher Easley, Dr. Steven Mansoorabadi, and Dr. Angela Calderón for their time and scholarly contributions to my doctoral degree. I cannot thank you enough, Dr. Angela Calderón, for how your two courses - Separation Science and Mass Spectrometry of Organic Compounds - expanded my knowledge of mass spectrometry techniques. Not only were my fundamentals of liquid and gas chromatography solidified, but my method development skills and experience after your courses have greatly improved my research.

I am also deeply indebted to the scientists, donors, and sponsors who have supported the work presented in this thesis. I thank Michael Zirpoli, Dr. Yuyan Yi, and Dr. Jingyi Zheng from the Department of Mathematics and Statistics at Auburn University for their tremendous contributions to my work. Their collaboration during this Ph.D. journey was crucial to the success

of many projects; two publications and a manuscript that is yet to be published. Thank you, Benedicta Donkor, for your scientific contribution to the first publication in the lab, which served as the basis for further publications. Many thanks to Dr. Steven Mansoorabadi, who was not only my committee member but also provided me with the microorganisms needed for my studies. I would like to thank Dr. Mark Liles from the Department of Biological Sciences for providing me with the non-pathogenic *Escherichia coli* strains. I also greatly appreciate the financial support from Auburn University and NIH grant 1R35GM147225.

To my lab colleague Kimberly Kartowikromo, with whom I spent most of my time within the lab, thank you for your scientific support and the friendly environment you created. To Dr. Jessica dos Santos Pizzo, Sheba Paul Maaji, Austin Clance, and Iffat Jerin: I may have only spent a few months with you, but those few months look like years with many valuable experiences. I can say with confidence that you all have made the lab a more productive and work-friendly environment.

To my friend, soon-to-be Dr. Segun Obisesan, my unpaid therapist, you have made the journey to a PhD an unforgettable experience, despite the great difficulties it entails. Talking about our failures and successes in the lab not only kept me going until the end of my PhD but also made me realize that the journey was less mentally taxing thanks to your supportive friendship. Amazing that we did not know each other in Nigeria, only communicated via the internet and then lived together for the last 4 years and the funny thing is that almost everyone thinks we are twins. Thank you so much for your mental support and the genuine friendship we built during this Ph.D. journey.

To my parents, Omolayo and Grace Olajide, thank you for your support, the frequent calls from Nigeria and the constant reminder that I will be the first-generation Ph.D. graduate of the family and therefore should keep pushing boundaries. I greatly appreciate your support not only

as parents but also as friends and thanks to my siblings who are always there to lift me up spiritually and mentally.

These acknowledgments not only serve to recognize those who have contributed to my success throughout my graduate career, but they also reflect the support it takes to achieve monumental greatness. Hard work, discipline, consistency, long-suffering, patience, and focus will make you great, but the power of support and mentoring cannot be underestimated.

Table of Contents

List of Tables

List of Figures

List of Abbreviations

UTIs	Urinary Tract Infections
cUTI	Complicated Urinary Tract Infections
CDC	Centers for Diseases Control and Prevention
STEC	Shiga toxin-producing *Escherichia coli*
AMR	Antimicrobial Resistance
VBNC	Viable but non-culturable
ELISA	Enzyme-linked Immunosorbent Assay
PCR	Polymerase Chain Reaction
PFGE	Pulsed-field Gel Electrophoresis
MS	Mass Spectrometry
MALDI	Matrix-assisted Laser Desorption Ionization
FDA	Food and Drug Administration
LC-MS	Liquid Chromatography – Mass Spectrometry
RPLC	Reversed Phase Liquid Chromatography
DESI	Desorption Electrospray Ionization
LTP	Low Temperature Plasma
LMJ-SPP	Liquid Micro-junction Surface Sampling Probe
REIMS	Rapid Evaporative Ionization Mass Spectrometry
LAESI	Laser Ablation Electrospray Ionization
PS	Paper Spray
TS	Touch Spray
LS	Leaf Spray
DART	Direct Analysis in Real Time
ESI	Electrospray Ionization
PE	Phosphatidylethanolamines
PG	Phosphatidylglycerol
CL	Cardiolipins

FAs	Fatty Acids
PCA	Principal Component Analysis
LDA	Linear Discriminant Analysis
PCs	Principal Component
CV	Cross-validation
IMS	Ion Mobility Spectrometry
MS/MS	Tandem MS
RT	Retention Time
DT	Drift time
CCS	Collision Cross Section
DTIMS	Drift Tube Ion Mobility Spectrometry
TWIMS	Travelling Wave Ion Mobility Spectrometry
TIMS	Trapped Ion Mobility Spectrometry
FAIMS	Field Asymmetric Ion Mobility Spectrometry
DMA	Differential Mobility Analyzers
ACN	Acetonitrile
MeOH	Methanol
IPA	Isopropyl alcohol
QTOF	Quadrupole Time of Flight
CID	Collision Induced Dissociation
CE	Collision Energies
m/z	Mass to charge ratio
DFT	Density Functional Theory
NBO	Natural Bond Orbital Analysis
TJ	Trajectory Method
MD	Molecular Dynamics
LAMMPS	Large-scale Atomic/Molecular Massively Parallel Simulator
VCap	Capillary Voltage
ATD	Arrival Time Distribution
RSD	Relative Standard Deviation
R_p	Resolving power

cTWIMS	Cyclic Traveling Wave Ion Mobility Spectrometry
SLIM	Structure for Lossless Ion Manipulations
CHAPS	3-[(3-Cholamidopropyl)-dimethylammonio]-1-propanesulfonate
LB	Luria Broth
DDA	Data Dependent Acquisition
DIA	Data Independent Acquisition
HRdm	High Resolution Demultiplexing
EIM	Extracted Ion Mobilogram
EIC	Extracted Ion Chromatogram

Chapter 1. Methods for the Detection of Bacterial Pathogens: Principles, Applications, Advantages, And Limitations

1.1. Health and Economical Burden of Bacterial Infections

Bacteria are an essential component of the human microbiome, colonizing tissues including the gastrointestinal tract and skin. Although majority of bacteria are harmless with some strains providing benefits in digestion and competition with opportunistic pathogens, bacterial infections are among the most common human illnesses [1, 2]. Among the most common bacterial infections worldwide are urinary tract infections (UTIs), foodborne illnesses, pneumonia, meningitis, etc. [3]. Not only do these bacterial infections increase health burden, but they also contribute massively to the economic burden. Complicated urinary tract infections (cUTI) are among the most frequent bacterial infections in the community and were the 14th ranked principal diagnosis for hospital admissions in the 2018 Healthcare Cost and utilization Project [4]. Recently, a U.S. national database study indicated that there are over 2.8 million cases of cUTI per year, resulting in annual 30-day total costs of more than $6 billion [4]. According to report from Centers for Diseases Control and Prevention (CDC), approximately 48 million people in the United States get ill, 128,000 people are hospitalized, and 3,000 people die annually due to foodborne diseases despite United States has the safest food supplies in the world [5, 6]. These health and economic burdens highlight the need for rapid and accurate diagnosis of these bacterial infections.

The common bacterial infections causative agents are *Listeria monocytogenes*, *Escherichia coli O157:H7*, *Staphylococcus aureus*, *Salmonella enterica*, *Bacillus cereus*, *Vibrio spp.*, *Campylobacter jejuni*, *Clostridium perfringens*, *Streptococcus agalactiae*, *Bacillus cereus*, *Klebsiella pneumoniae*, *Shiga toxin-producing Escherichia coli (STEC)*, etc. [6, 7]. Unequivocal

identification of bacteria is essential for several clinical and biological applications, such as the treatment of disease in animals and plants, where accurate diagnosis is required for an efficient and effective strategy to eradicate infectious microorganisms. Accurate diagnosis is also important in limiting the possibility of toxicity to host cells as well as reducing the risk of developing antimicrobial resistance (AMR). If the accurate discrimination of bacteria is left unaddressed, AMR in bacteria could kill 10 million people per year by 2050, which would surpass current cancer mortality [8]. A 2019 report by CDC on antibiotics as effective treatment for uncomplicated UTIs found that more than 2.8 million cases of infections are caused by antibiotic-resistance pathogens at any anatomic location occur in the US annually, resulting in approximately 35,000 deaths. This shows a marked increase in infection rate and deaths from the equivalent 2013 CDC report (previously 2 million cases of antibiotic-resistant infections, and 23,000 resultant deaths) [9]. Hence, highly sensitive and specific discrimination methods are required that would discriminate bacteria not only at the genus level but up to the strain level which is more challenging due to the close genetic similarity of the strains. Therefore, effective treatments would depend on rapid and accurate identification of the causative strain, leading to strain-specific therapy that would shorten hospitalization periods, improve patient recovery, and lower antibiotic resistance.

1.2. Traditional Methods for Diagnosis of Bacterial Infections

The conventional methods for detecting bacterial infections in urine, blood, food samples are based on culturing the microorganisms on agar plates followed by standard biochemical identifications [10]. These methods are cost effective and very simple however they are time consuming as they are hugely dependent on the ability of the microorganisms to grow in different culture media such as pre-enrichment media, selective enrichment media, and selective plating

media. Usually the processing associated with conventional methods typically requires about 2 to 3 days for preliminary identification and more than a week for confirmation of the species of the pathogens [11]. During this period patients received broad spectrum antimicrobial treatments. Although this strategy is efficient for most cases, it is also known to have a strong impact on the development of antimicrobial resistance. Indeed, among patients' urine samples tested for UTI, a large proportion are found not infected. For others, the prescription of broad-spectrum antibiotics, rather than species-specifics antibiotics, might lower the efficiency of the therapy [12, 13]. But in all cases, this misuse of antibiotics increases the emergence of multi-drug resistant bacteria [14-18]. False negative results may occur due to viable but non-culturable (VBNC) pathogens [18]. The failure to detect these pathogens would increase the transmission risk of the pathogens. Therefore, there is a need for the development of fast, robust, and accurate methods for bacterial identification, to improve therapies and guide rational use of antibiotics.

Many new methods have emerged for the rapid diagnosis of bacterial infections including immuno-assays such as the enzyme-linked immunosorbent assay (ELISA). ELISAs are a widely used immunological approach that is less expensive; however, it has some significant disadvantages such as the need for highly specific antibodies and prior knowledge which has made it direct application in medical field limited [11, 19]. Genotyping methods, which are based on the sequencing of partial (16S small subunit ribosomal [rRNA] gene sequencing) or entire (Whole Genome Sequencing) genomes of the microorganisms contained in a sample, are promising because they do not require bacterial culture and can be applied to complex samples containing several species [7, 20, 21]. However, the cost and the time required to get identification by sequencing methods preclude their use in routine laboratories. In addition, if 16S rRNA sequencing can provide a quite rapid identification (typically 24 h), the high conversation of 16S gene

sequences across bacterial families and species often limits the precision of identification to the genus level [7, 22, 23]. By contrast, Whole Genome Sequencing can provide an efficient species and even strain typing, but it is costly and time consuming to get the results is strongly extended by the sequencing itself and by the data analysis. Examples of these methods include polymerase chain reaction (PCR) and pulsed-field gel electrophoresis (PFGE) [8, 24]. PCR methods are sensitive, often eliminating the need for cultural enrichment, but lacking the required specificity to be considered confirmatory at the strain level [24]. Hence, alternative analytical methods that ensure minimal time consumption, and provide high sensitivity and specificity at the strain level are needed. The advantages and disadvantages of traditional methods used to characterize bacteria are summarized in Table 1.1.

Table 1.1. Advantages and disadvantages of traditional methods used to characterize bacteria [8]

Methods	Advantages	Disadvantages
ELISA	• Reliability • Specificity • Sensitivity	• Labor-intensive • Need for highly specific antibodies and prior knowledge
PFGE	• Extremely powerful in the analysis of large molecules from a variety of sources • DNA restriction patterns generated by PFGE are stable and reproducible	• Time consuming • Bands are not independent • High cost
PCR	• Sensitive • Precise • Accurate	• Target DNA sequence must be known • Small amounts of contaminants within samples interfere with experiments • Cannot different between live versus dead bacteria • Time consuming • Requires expertise

1.3. Mass Spectrometry for Clinical Diagnosis of Bacterial Diseases

The combined advantages of sensitivity, specificity, and speed make mass spectrometry (MS) an attractive analytical platform for the analysis of intact microorganisms. The analysis of microbial proteins leading to effective bacterial identification has achieved a breakthrough in routine clinical microbiology laboratories with the introduction of matrix-assisted laser desorption ionization mass spectrometry (MADLI-MS) [25, 26]. In MALDI-MS, molecular ions are generated when a laser beam hits analytes that are mixed with a matrix and dried in air before analysis [27]. Since MALDI is a very soft ionization technique, proteins in whole bacterial cells can be measured directly without fragmentation [28, 29]. In these methods, most of the proteins that can be identified are ribosomal proteins, which are quite easy to detect due to their small size and high abundance [30]. One of the advantages of the measured ribosomes is that they are always produced under all growth conditions and are therefore not susceptible to variable phenotypic effects during bacterial cultivation; this may be the reason why the method is very stable and routinely used in many clinical microbiology laboratories. In addition, the MALDI-MS method is very simple in sample preparation and timesaving, which makes it a good substitute for conventional phenotype-based methods as it reduces the time required for identification from 2 or 4 days to less than 50 hours. For these reasons, two mass spectrometers, the Biotyper (Bruker) and the Vitek-MS (Shimadzu-BioMerieux), were approved for clinical use in 2013 by the health organizations of most countries, including the US Food and Drug Administration (FDA) [31]. Identification of bacteria by MADLI-MS at the genus or species level is usually based on the protein mass patterns obtained together with a library-based approach or bioinformatic analysis [32]. In both methods, the analyst compares distinguished and discriminated peaks (biomarkers) in the MADLI-MS profiles of the analyzed bacteria with publicly available databases [33, 34].

Despite its numerous advantages, bacterial identification by MALDI-TOF MS has several disadvantages: 1) It requires a lengthy culture step to isolate bacterial colonies, as the detection is based on a comparison with a spectral database acquired on pure colonies. For the same reason, it is not able to identify polymicrobial infections (i.e. when multiple species are present in the same sample) without analyzing multiple types of colonies visually selected on the culture plate [35]; 2) due to minimal sample preparation, the information contained in the spectra is limited to the most abundant molecules, limiting the specificity of the method and its ability to identify specific species or subspecies [26, 30]; 3) it is not quantitative, potentially important information for certain samples where pathogens need to be differentiated from the normal microbiota, or when a certain level of infection must be reached to require anti-biotherapy [7]; and 4) relatively low selectivity due to the inability of MS to separate isomers [36]. While identification using MALDI-TOF (BioTyper and Vitek) relied on reference databases to identify and classify microorganisms according to their mass spectra fingerprint, MALDI-TOF/TOF uses peptide ion fragment from MS/MS scans which facilitate more accurate bacteria identification. Even with the introduction of MADLI TOF/TOF, bacterial identification using MALDI suffers a major drawback which is the small number of identified proteins per sample. These identified proteins are ribosomal proteins which are often highly conserved and similar within a species limiting the performance of MALDI TOF/TOF for strain or serotype differentiation [37]. In contrast to MALDI-TOF MS, front-end separations with MS, such as liquid chromatography-mass spectrometry (LC-MS), have high dynamic sensitivity, i.e., increased protein signals with a concomitant increase in taxonomic resolution, and high selectivity due to the ability of LC to provide isomer separation [38, 39]. In fact, LC-MS methods have differentiated strains of *Enterobacter sakazakii* [40], Shiga-toxigenic *Escherichia coli* [41], *Vibrio parahaemolyticus* [42], and *Bacillus cereus* [43]. Although

LC-MS methods could differentiate strains, this method is labor-intensive and time-consuming, primarily because of the extensive sample preparation and long LC acquisition times. Therefore, alternative techniques with minimal sample preparation and rapid analysis are needed as early detection of bacteria allows quick clinical intervention.

1.4. Ambient Ionization for Rapid Detection of Bacteria

Ambient ionization MS is a technique for direct analysis by ionizing analytes at ambient pressure and temperature conditions without sample preparation. Advantages of ambient ionization techniques include minimal sample preparation, low sample and solvent volumes utilization, and direct rapid analysis [44]. Ambient ionization can be largely categorized into three main classes primarily based on their desorption methods: liquid extraction, plasma desorption, and laser ablation [45]. An extensive description of each ambient ionization technique under each classification and their applications in forensics, biomedical, environmental, bioanalysis, in vivo analysis, food and agriculture, and reaction monitoring and catalysis have been detailed in previous reviews [45, 46].

Several ambient ionization mass spectrometry methods have been developed and reported to be efficient in discriminating various microorganisms, such as desorption electrospray ionization (DESI) [47], low temperature plasma (LTP) [48], nanospray desorption electrospray ionization (nanoDESI) [49], liquid microjunction surface sampling probe (LMJ-SSP) [50], rapid evaporative ionization MS (REIMS) [51], laser ablation electrospray ionization (LAESI) [52], paper spray (PS) [53], touch spray (TS) [54], and direct analysis in real-time (DART) [55]. DESI was employed to measure lipids directly from sixteen bacteria samples without extraction or another sample preparation. Differentiation of the different bacterial species was achieved using either the positive

or the negative ion mode DESI mass spectra covering the mass/charge range up to *m/z* 1000. The data was confirmed by electrospray mass spectrometry (ESI-MS) of lipid extracts from the same bacterial samples. Although the signals were lower, the quality of the direct ionization DESI spectra compared favorably with that of the ESI spectra extracts prepared using chloroform/methanol. The unit of mass resolution in these experiments allows for overlaps of nominally isobaric lipids at particular *m/z* values. Tandem mass spectrometry was performed to validate the presence of particular lipids falling into several classes of phospholipids, including phosphatidylethanolamines (PE), phosphatidylglycerols (PG) and lysophospholipids. The data from the different bacteria were compared using principal component analysis (PCA), which indicated that the different species are readily distinguished, and that different growth media do not prevent bacterial differentiation in the cases examined [56]. From the same laboratory, sixteen different bacteria representing eight genera from Gram-positive and Gram-negative bacteria were separated using paper spray mass spectrometry. The lipid information in the negative ion mass spectra proved useful for species level differentiation of the investigated Gram-positive bacteria, while Gram-negative bacteria were differentiated at the species level by using a numerical data fusion strategy of positive and negative ion mass spectra as shown in Figure 1.1 [53].

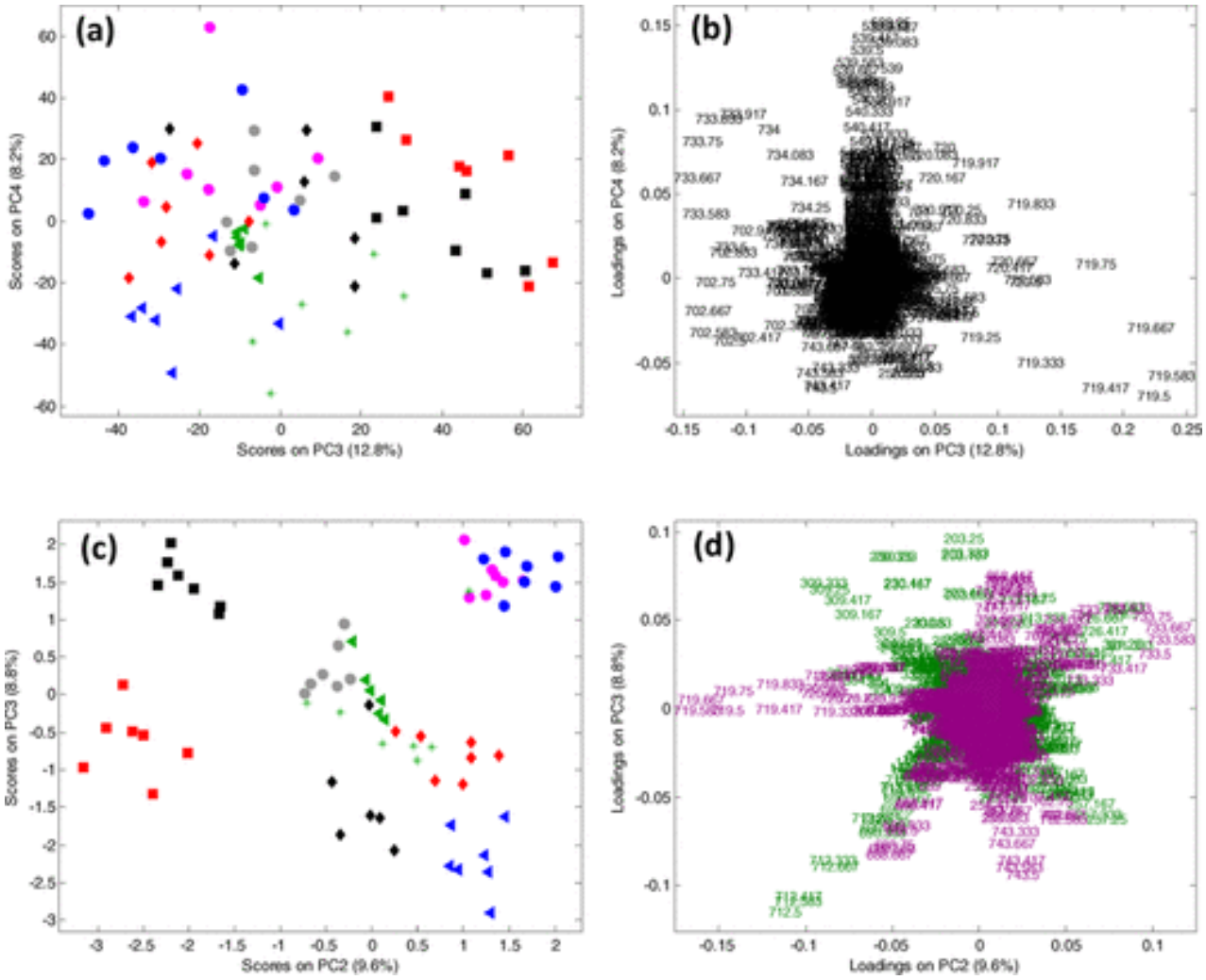

Figure 1.1. PCA of Gram-negative bacteria: *C. farmeri* (black squares), *C. freundii* (red squares), *E. aerogenes* (gray circles), *E. asburiae* (pink circles), *E. cloacae* (blue circles), *P. penneri* (black diamond), *P. vulgaris* (red diamond), *E. coli* (green stars), *P. aeruginosa* (green triangles), and *P. fluorescens* (blue triangles). Negative ions: (a) PC3 versus PC4 score plot. (b) PC3 versus PC4 loading plot. Fused positive and negative ions: (c) PC2 versus PC3 score plot. (d) PC2 versus PC3 original loading plots labeled in terms of m/z ratio. Violet, negative ions, green, positive ions.

The paper spray mass spectrometry was challenged to discriminate eight closely related *Candida* species with clinical relevance and known phylogeny. The discrimination of the *Candida* species was solely based on the characteristic's lipid profiles of the individual species; *Candida albicans, Candida krusei, Candida dubliniensis, Candida lusitaniae, Candida glabrata, Candidia*

parapsilosis, Candida tropicalis, and *Candida guilliermondii.* Visual differences in the mass spectra in the negative ion mode are evident between some of the species, namely *Candida glabrata*, *Candida guilliermondii*, and *Candida krusei.* On the other hand, the spectra of *Candida albicans* and *Candida dubliniensis* are nearly identical. The spectra of *Candida lusitaniae, Candidia parapsilosis,* and *Candida tropicalis* appear to have slight differences in the relative abundances of major ions [57]. However as shown in Figure 1.2, there is poor separation of the *Candida* species even with the fusion of positive and negative ion mode information. This implies that more selective analytical techniques for discrimination of species is needed.

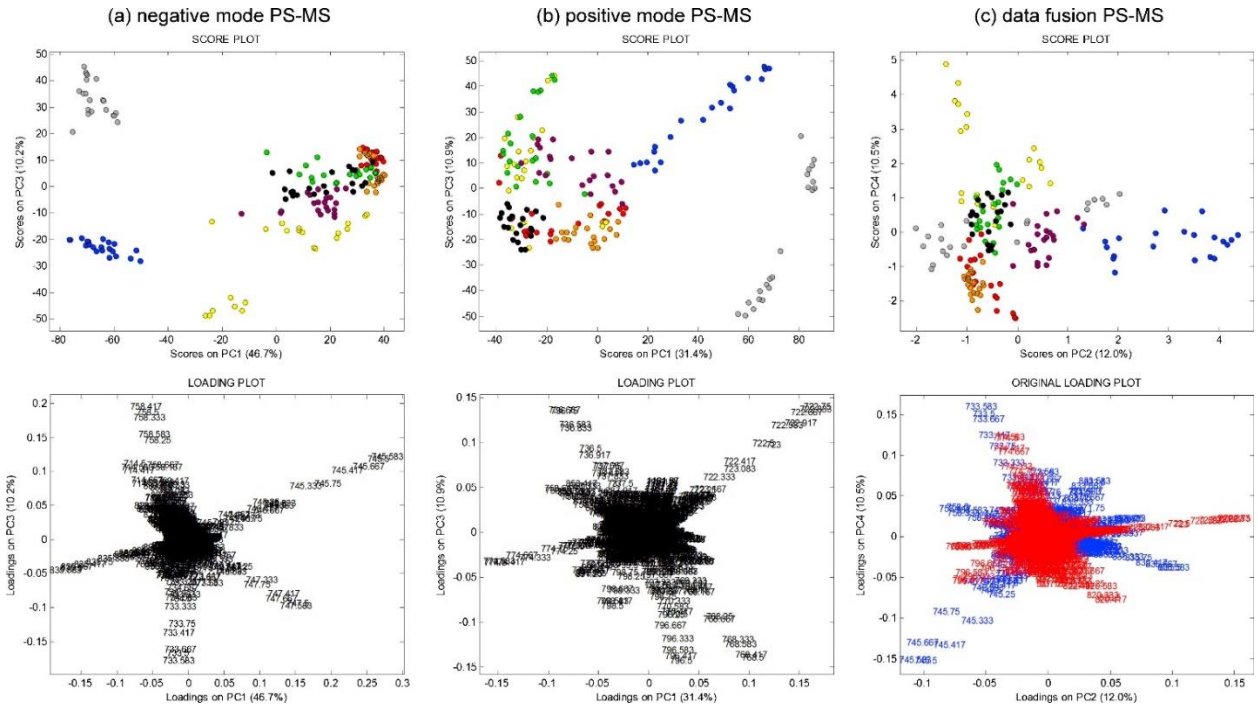

Figure 1.2. (a) Negative mode PCA score and loading plot, upper and lower respectively, of *Candida* species. (b) Positive mode PCA score and loading plot. (c) PCA score and loading plot (negative ions, blue and positive ions, red) after data fusion. Species are indicated by color: *C. albicans* (red), *C. dubliniensis* (orange), *C. glabrata* (grey), *C. guilliermondii* (yellow), *C. krusei* (blue), *C. lusitaniae* (green), *C. parapsilosis* (dark violet), *C. tropicalis* (black). (For interpretation of the references to color in this figure legend, the reader is referred to the web version of this article.)

1.5. Ion Mobility Spectrometry for Accurate Discrimination of Bacteria through Isomeric Biomarker Discovery

The reduced selectivity of ambient ionization MS methods which is caused by the inability of MS to distinguish isomers with identical chemical formulae poses a challenge for the analysis of complex samples and reduction in its capability to differentiate bacteria species and strains. [58, 59]. Ion mobility spectrometry (IMS) is particularly suited to address the structural challenges endemic to isomers. IMS is a gas phase separation technique in which structurally distinct compounds are distinguished based on collisions between analyte ions and inert buffer gas molecules under the influence of a weak electric field [60]. Since separations based on IM can improve the selectivity of ambient ionization techniques, they have been increasingly used to overcome problems associated with the analysis of complex samples by ambient ionization techniques [58, 61, 62]. Noteworthily, most of the ambient ionization techniques utilized membrane lipids (e.g. phospholipids) as diagnostic biomarkers to discriminate various microorganisms [45, 63]. However, phospholipids can have a variety of isomers through the variations in headgroup, chain length, sn-position, double bond position, and configuration of double bonds (i.e., *cis* versus *trans*) which causes their structural analyses to be very challenging [64, 65].

Previous MS-based studies have been utilized in the characterization of diagnostic lipids utilizing liquid chromatography (LC), tandem mass spectrometry (MS/MS), and derivatization experiments which are labor-intensive and time-consuming [64-67]. LC-MS alone cannot resolve all the lipid isomer types and does not provide comprehensive structural annotation of lipid isomers in untargeted analyses [43]. These challenges limit the application of LC-MS for bacteria species and strain level differentiation since the identity of the isomeric lipid biomarkers that distinguish

the bacteria species and strains are unknown. Tandem mass spectrometry (MS/MS) doesn't only provide structural information about the isomeric lipid biomarkers but also serves as a "fingerprint" used to confirm the identity of each microorganism [39, 68]. However, the problem of similar fragmentation patterns in some isomer types (e.g., geometric isomers) limits the discriminatory power of tandem MS for species and strain-level differentiation. Clear separation between diagnostic lipid isomer biomarkers is required to discriminate and identify bacteria species and strains reliably.

In IM, structurally different lipid ions rapidly separate in the gas phase due to numerous collisions between lipid ions and inert buffer gas molecules under the influence of an electric field [60]. IMS separates ions based on their mobility rates (K or K_0; K is usually reported as K_0 under standard pressure and temperature) through the combined action of an electric field and neutral buffer gas. The mobility of the ions depends on characteristics of the ions such as mass, size, shape, and charge number, leading to the separation of compounds with the same *m/z* but different structures (isomers) due to the influence of the neutral buffer gas and electric field. Although IMS can detect the size of an ion, it cannot determine its exact molecular weight. Therefore, IM-MS is more valuable, combining complementary size selection and quality mass separation into a single analysis platform [69]. IMS separations typically occur on a timescale of 10^{-3}-10^{-2} s, hence, are well-suited for incorporation between LC (10^{2}-10^{3} s timescale) and mass spectrometry techniques (10^{-6}-10^{-4} s timescale), thereby providing three orthogonal dimensions of separation: polarity, size, and mass. This results in a four-dimensional dataset including RT, drift time (DT), *m/z*, and fragmentation pattern, all captured in a single sampling event [69-71]. The supplementary advantages of IMS separation when coupled with MS, such as separation of isomers, signal filtering, and CCS fingerprinting, depends on the resolution of the IMS technique and the accuracy

of collision cross section (CCS) measurement by the IMS technique. These parameters must be considered when selecting IMS instruments.

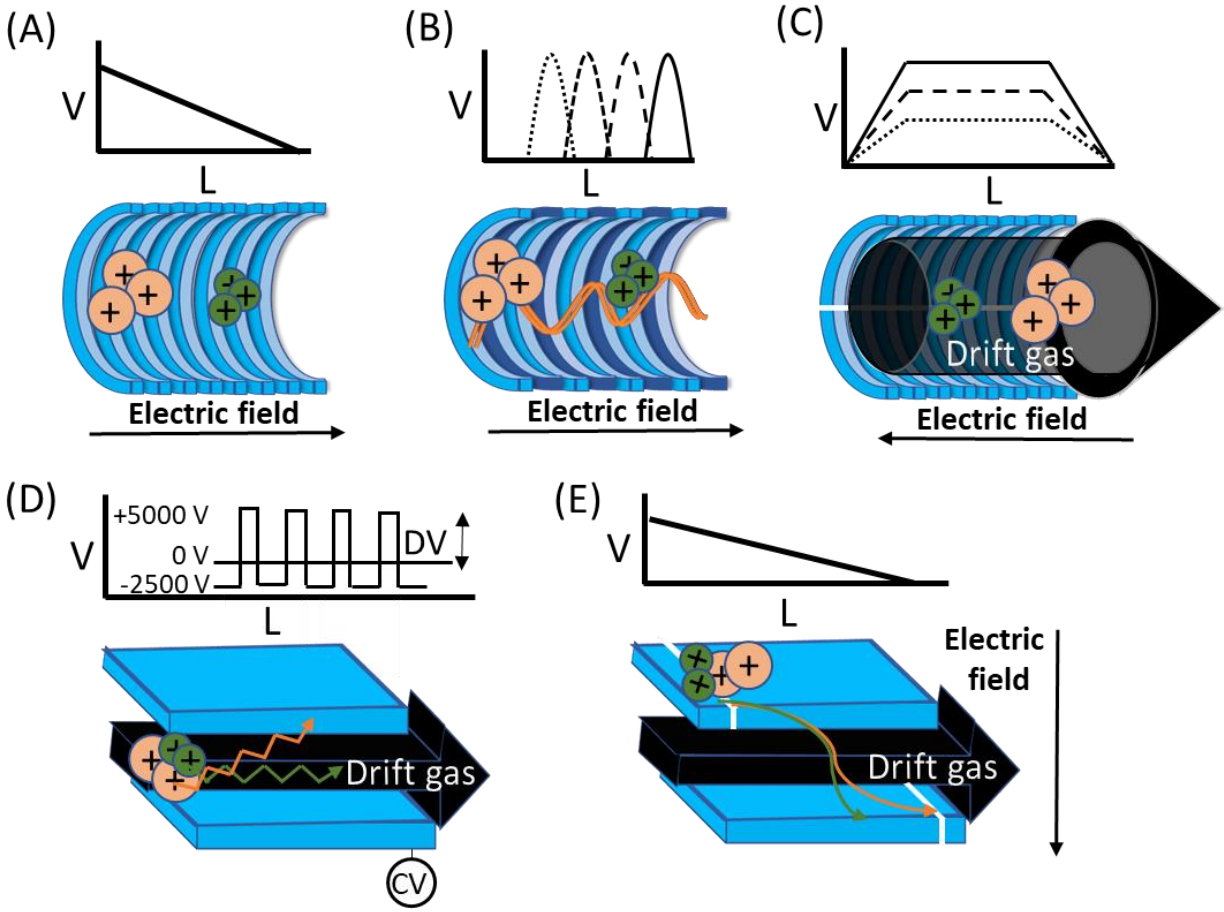

Figure 1.3. Schematic diagram of various IMS technology and separation mechanisms (A) DTIMS (B) TWIMS (C) TIMS (D) FAIMS (E) DMA

According to separation mechanisms, IMS can be classified into temporal dispersive, spatial dispersive, and confinement and selective release; and based on electric field applications, it can be classified into static and dynamic fields [72-75]. In temporal dispersive, all ions drift along similar paths colliding with the neutral buffer gas under the influence of electric fields, resulting in different arrival times (mainly DTIMS and TWIMS), while in spatial dispersive, ions are separated along different drift paths (mainly DMS, FAIMS, Aspiration IMS (AIMS), and

DMAs). In confinement and selective release IMS (mainly TIMS), ions are trapped within a pressurized region by a precisely adjustable electrodynamic field and are then selectively released based on differences in their mobility [69]. Static field IMS instruments employ linear and constant electric fields (mainly DTIMS and DMA), whereas dynamic field IMS instruments utilizes non-uniform electric field (mainly FAIMS, TWIMS, and TIMS) (Figure 1.3) [73].

Chapter 2. Liquid Chromatography Ion Mobility Quadruple Time of Flight Mass Spectrometer (Agilent 6560): Instrumentation and Theoretical Calculations

2.1. Liquid Chromatography System

Our ion mobility mass spectrometry instrument (Agilent 6560, Santa Clara, CA) is coupled with an ultra-high-performance liquid chromatography (UHPLC) platform (Agilent 1290, Santa Clara, CA). Therefore, our platform provides the combined separation power and selectivity of LC, IMS, and MS techniques. The LC system consists of a binary pump, multi-sampler, and a column compartment [76]. It can be operated in different modes including Normal Phase (NP), Reversed Phase (RP), Hydrophilic Interaction LC (HILIC) and so many more [77, 78]. We utilized the most common mode of separation, reversed phase, in this dissertation since the analytes are moderately polar to non-polar. In reversed phase, the analytes are dissolved in a polar mobile phase such as H_2O, MeOH, IPA, and ACN and then separated based on their hydrophobicity between the polar mobile phase and the non-polar stationary phase (e.g., C18, C8, C4, etc.) [77]. Hence, the polar analytes are eluted first followed by the non-polar analytes that are strongly retained on the non-polar stationary phase. Organic modifiers such as formic acid, ammonium acetate, etc., can be used to improve separation or signal intensities. In fact, the LC system offers fast chromatographic separation with sub-two-micron particle size columns with internal diameter from 1 to 5 mm with operation at pressure up to 1200 bar [76]. The Agilent 1290 Infinity binary pump contains new technology to overcome the problems of pumping LC solvents at ultra-high pressure and high flow rates. It can deliver flow in the range of 0.05 – 5 mL/min at pressures up to 1200 bar [76]. The binary pump delivers accurate percentage composition of the mobile phase

needed to ensure optimal separation in the stationary phase. The eluted analytes are then ionized in the ionization source as described in the next section.

2.2. Electrospray Ionization Source

Electrospray ionization (ESI) relies in part on chemistry to generate analyte ions in solution before the analyte reaches the mass spectrometer. As shown in Figure 2.1A, the LC eluent is sprayed (nebulized) into a spray chamber at atmospheric pressure in the presence of a strong electrostatic field and heated drying gas [79, 80]. The electrostatic field occurs between the nebulizer and the capillary. The spray occurs at right angles to the capillary. This design reduces background noise from droplets, increasing sensitivity, and keeps the capillary cleaner for a longer period [79]. The ESI consists of four steps, namely, (1) formation of ions, (2) Nebulization, (3) Desolvation and ion evaporation.

A special type of Electrospray ionization source named Agilent Jet Stream (AJS) Thermal Gradient Technology is utilized in this research work. The AJS ESI source enhances analyte desolvation by collimating the nebulizer spray and creating a dramatically increased signal. The addition of a collinear, concentric, super-heated nitrogen sheath gas to the inlet assembly significantly improves ion drying from the electrospray plume and leads to increased mass spectrometer signal to noise ratios. Parameters for the AJS Technology are the superheated nitrogen sheath gas temperature and flow rate, and the nozzle voltage. The generated ions are then transmitted through a capillary into the ion mobility drift tube for separation based on size, shape, and charge [79].

2.3. Agilent 6560 Ion Mobility Separation Dimension

2.3.1. Front Funnel

Ions generated in the source region are carried into the front funnel through a single bore capillary. The front funnel (Figure 2.1C) improves the sensitivity by efficiently collimating the ion beam and transferring the gas-phase ions into the trapping funnel while it pumps away excess gas and neutral molecules. The front funnel operates at high pressure of ~5.0 Torr [79].

2.3.2. Trapping Funnel

The trapping funnel (Figure 2.1D) accumulates and releases ions into the drift tube. The continuous ion beam from the electrospray process has to be converted into a pulsed ion beam prior to ion mobility separation. The trapping funnel first stores and then releases discrete packets of ions into the drift tube [79]. Also, a tapered section at the exit region of the trapping funnel is designed to focus the ion packets into the drift cell to avoid ion losses and improve resolution and sensitivity [79]. High abundance, well-confined packet of ions enters the drift tube which results in high resolution and high sensitivity. The parameters on the MassHunter data acquisition software controlling the accumulation and release of the ions by the trapping funnel are Trap filling time and Trap release time.

2.3.3. Drift Tube

The drift tube (Figure 2.1E) is approximately 80 cm long and generally operated at 20 V/cm or less drift field [79]. Ions are separated as they pass through the drift tube based on their collision cross section (CCS) which is defined to be the average rotational surface area of the molecule as a result of collision with the inert buffer gas. Ions with larger CCS values undergo a higher number of collisions with drift gas molecules compared to ions with smaller collision cross section. Therefore, larger ions travel through the drift tube slower than the smaller ions. Also, ions

with higher charge state experience a higher electric field, and hence travel at a higher velocity, compared to ions with lower charge states [75]. The drift tube is operated under low field conditions that allow the instrument to generate accurate structural information for compounds. In addition to separating ions based on their structures, experiments can be performed to measure the CCS values.

2.3.4. Rear funnel

As the ions leave the drift tube, they enter the rear funnel (Figure 2.1F), which efficiently refocuses and transfers ions to the mass analyzer through a hexapole ion guide [79].

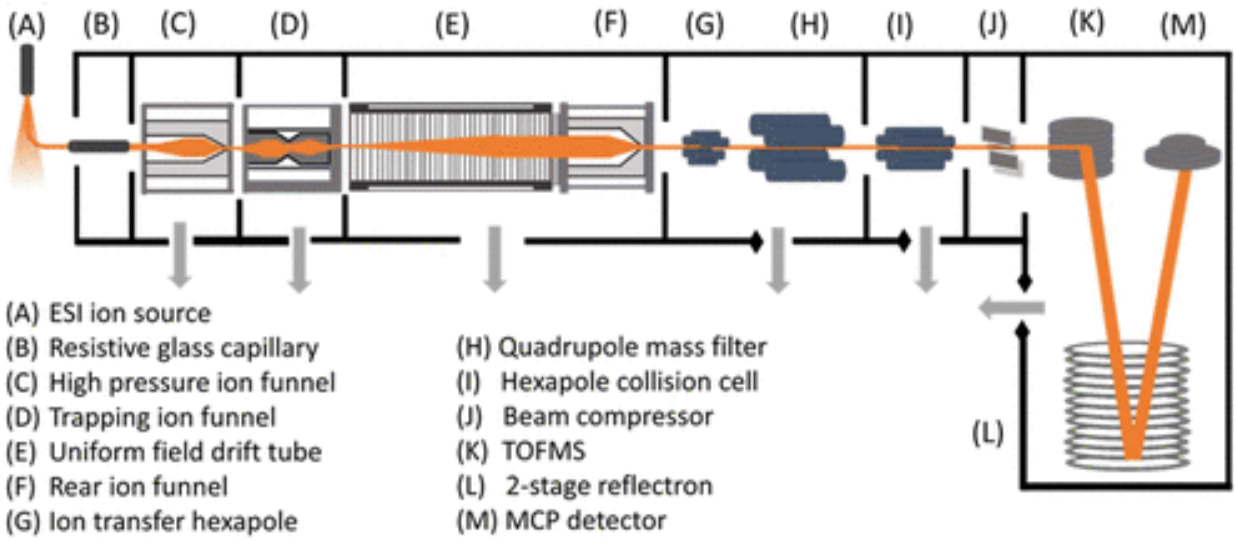

Figure 2.1. Schematic and photographic illustrations of IM-QTOF-MS Agilent 6560 instrument

2.4. Agilent 6560 Quadruple Time of Flight – MS

Ions exiting the rear funnel are guided and transmitted through front end optics including ion transfer hexapole. Following the hexapole, ions are introduced into the QTOF-MS system which incorporates a quadruple mass filter, collision cell, and time of flight mass analyzer (Figure

2.1). The quadruple consists of four hyperbolic rods that optimize ion transmission and spectral resolution. Ions selected by quadruple are then passed to the collision cell where they are fragmented. The collision cell is a high pressure hexapole assembly containing high purity nitrogen gas for fragmentation [79]. The geometry of a hexapole provides advantages in two domains: ion focusing and ion transmission. Hence, hexapole is chosen for the collision cell because overall, it is the best for both ions focusing and ion transmission [79]. The ions then enter the ion beam compressor (Figure 2.1J). Ion beam compression provides up to a 10-fold compression and cooling which helps in creating a much denser and thinner ion beam that passes through a narrower slit leading into the slicer and pulser region.

The narrow ion beam passes into the time-of-flight ion pulser. To start the flight of the ions to the detector, a high voltage (HV) pulse is applied, and the applied pulse accelerates the ions through the stack of pulser plates, acting as a rapid-fire ion gun. The ions leave the ion pulser and travel through the flight tube. Because the ions entered the ion pulser with a certain amount of forward momentum orthogonal to the flight direction in the flight tube, they never return to the ion pulser, but move to where the ion detector is mounted [79]. The ion mirror which is the 2-stage reflectron increases the resolving power of the instrument by effectively doubling the flight distance (from one meter to two meters) in the same space, and by performing a refocusing operation so that ions having different initial velocities still arrive simultaneously at the detector. Because the calculation for the mass of each ion depends on its flight time in the flight tube, the background gas pressure must be very low. Any collision of an ion with residual gas slows the ion on its path to the detector and affects the accuracy of the mass calculation [79].

At the surface of the ion detector is a microchannel plate (MCP), a very thin plate containing a set of microscopic tubes that pass from the front surface to the rear of the plate. When

an ion hits the front surface of the MCP, an electron escapes and begins the process of electrical signal amplification. As freed electrons collide with the walls of the microscopic tubes, an ever-increasing cascade of electrons travels to the rear of the plate. Roughly 10 times more electrons exit the MCP than incoming ions contact the surface. These electrons are then focused onto a scintillator, which when struck by electrons, produces a flash of light. The light from the scintillator is focused through two small lenses onto a photomultiplier tube (PMT), which produces the electrical signal read by the data system [79].

2.5. Fragmentation modes in Agilent 6560 Quadruple Time of Flight – MS

The quadruple can be operated in two modes during fragmentation: (1) total ion transmission and (2) isolation. In the total ion transmission (TTI), as the name implies, all the ions are transmitted through the quadruple to the collision cell. When collision energy is applied, fragmentation of the precursor ions will occur. This type of fragmentation is called Data Independent Acquisition (DIA) popularly known as All-ions fragmentation (AIF) [81]. In the second mode, the quadruple is operating within a particular isolation window and ions that are within these isolation windows are fragmented in the collision cell, this type of fragmentation is referred to as Data Dependent Acquisition (DDA) [82]. The DDA can be further divided into two fragmentation modes: (1) Auto-MS/MS and (2) Targeted MS/MS. In the Auto MS/MS, the precursors are selected based on user-designated settings including abundance and charge state, while in the targeted MS/MS, the precursors are determined by the user and are entered into a targeted list. There are three width options when operating the quadruple in the isolation windows: (1) Wide, 9 Da, (2) Medium, 4 Da, and (3) Narrow, 1.3 Da [79]. For narrow isolation widths, the isolation window is centered on the monoisotopic peak of a cluster, and the ion is isolated.

However, for the medium and the wide isolation widths, the range is not evenly applied. Once the monoisotopic ion is determined 0.3 *m/z* is subtracted from that mass. This is then the beginning of the isolation window. Then for the medium isolation 2 *m/z* is added to the now-determined subtracted mass, and this ion is then used as the center point of the isolation window [79].

2.6. Ion Mobility Collision Cross Section Experimental Measurements

The CCS measurements in IM experiment can be performed using the single-field (calibrant-dependent) and stepped-field (calibrant-independent) methods [83]. The stepped-field method, implemented in DTIM–MS measurements such as the Agilent 6560 instrument, is the only calibrant-independent method in which the IM experiments use multiple drift fields to estimate the CCS values by building a linear regression between the measured arrival times and the inversed drift voltages [83, 84]. In stepped-field method, the sample solutions would be infused directly using a nanospray source, and the analytes' CCS values would be measured using seven electric fields by increasing the entrance potential from 1100 V to 1700 V in 100 V increments every 30 seconds, corresponding to a drift field of 10.8 - 18.5 V/cm. In contrast, one drift field (18.5 V/cm) is utilized to measure the CCS values in the single-field method. The single field measurement is made using mobility calibrants (Agilent tune mix composed of phosphazine ions) that have known CCS values. These calibrants are used to create a linear calibration curve between the arrival times and their corresponding CCS values. This calibration curve allows the experimental CCS values of the analytes to be obtained from their arrival times [85]. In addition, a new approach to single-field CCS measurements was developed and evaluated in this research work to minimize the needed analysis time while increasing accuracy [86].

2.7. Theoretical Approaches to Collision Cross Sections Calculations

Density functional theory (DFT) calculations were carried out to identify the lowest energy structures of various isomers using the Gaussian 16 software package [87]. Geometry optimization, vibrational frequency analysis, and natural bond orbital analysis (NBO) were performed using hybrid density functional B3LYP method in combination with 6-31G(d,p) basis set. A zero-point energy correction was performed for all calculated structures. The possible protonation sites were selected based on NBO charge distribution and the protonated structures were optimized accordingly [88, 89]. The trajectory method (TJ) using the IMoS software package was used to compute the CCS values associated with the lowest energy structures at 3.95 Torr and 300 K [90, 91].

Moreover, classical molecular dynamics (MD) simulations were performed to model and predict the structural changes of S-(-)-verapamil in vacuum. The simulations were performed using a Large-scale Atomic/Molecular Massively Parallel Simulator (LAMMPS). NVT (constant number, volume, and temperature) molecular dynamics simulations were performed using a Nosé-Hoover thermostat at 300 K [92]. The system was pre-equilibrated for 100 ps and the conformations were sampled every 1 ps from the 200 ps simulations. Like the DFT structure calculations, the TJ method using IMoS was used to compute the CCS values of the 200 structures at 3.95 Torr and 300 K. Single-point energy calculations at B3LYP/6-31G(d,p) level were used to calculate the energies of the 200 structures.

2.8. Resolution Improvement in Drift tube IMS using post-processing software

The IMS resolving power (R_p) of the Agilent 6560 in the single pulse mode is ~60 R_p (CCS/ΔCCS). In a single pulse experiment, a single packet of ion is accumulated and release for

a single IM experiment which is typically 60 ms (Figure 2.2B). This results in a characteristically low instrument utilization efficiency, or duty cycle, that is typically less than 1% [93]. For instance, a release time of 250 μs (0.25 ms/60 ms) would results in a low duty cycle of 0.4%. The implication of this is that no ions is released into the drift tube for the remaining ~59.75 ms resulting in lowered sensitivity due to a single packet of ions being released and other ion losses. Multiplexing strategies have been utilized to enhance the sensitivity and duty cycle of IMS instruments (Figure 2.2C). Ion multiplexing is a strategy where multiple ion pulses are introduced to the IMS during each data acquisition cycle. A pseudorandom binary sequence is applied to the ion gate to introduce multiple ion pulses into the drift tube during each IMS measurement cycle [71, 93]. For instance, as shown in the Figure 2.2C, an extended Hadamard Sequence derived from a 4-bit maximal linear feedback register sequence was used. The sequence has 15 logical elements (8 open, 7 closed). This sequentially gated ion packets at predetermined intervals (i.e., eight packets injected during one scan interval) results in improved *S/N* and instruments sensitivity.

The overlapping spectra from the multiplexing processing are deconvoluted and combined post-acquisition based on the pseudorandom gate timing using the PNNL PreProcessor software package developed at Pacific Northwest National Lab (PNNL, omics.pnl.gov) [94]. The multiplexing processing only improve instrument sensitivity and does not affect IMS resolution, hence, the IMS resolving power (*R*p) of the Agilent 6560 in the single pulse or multiplex mode is ~ 60 R_p (CCS/ΔCCS) [95].

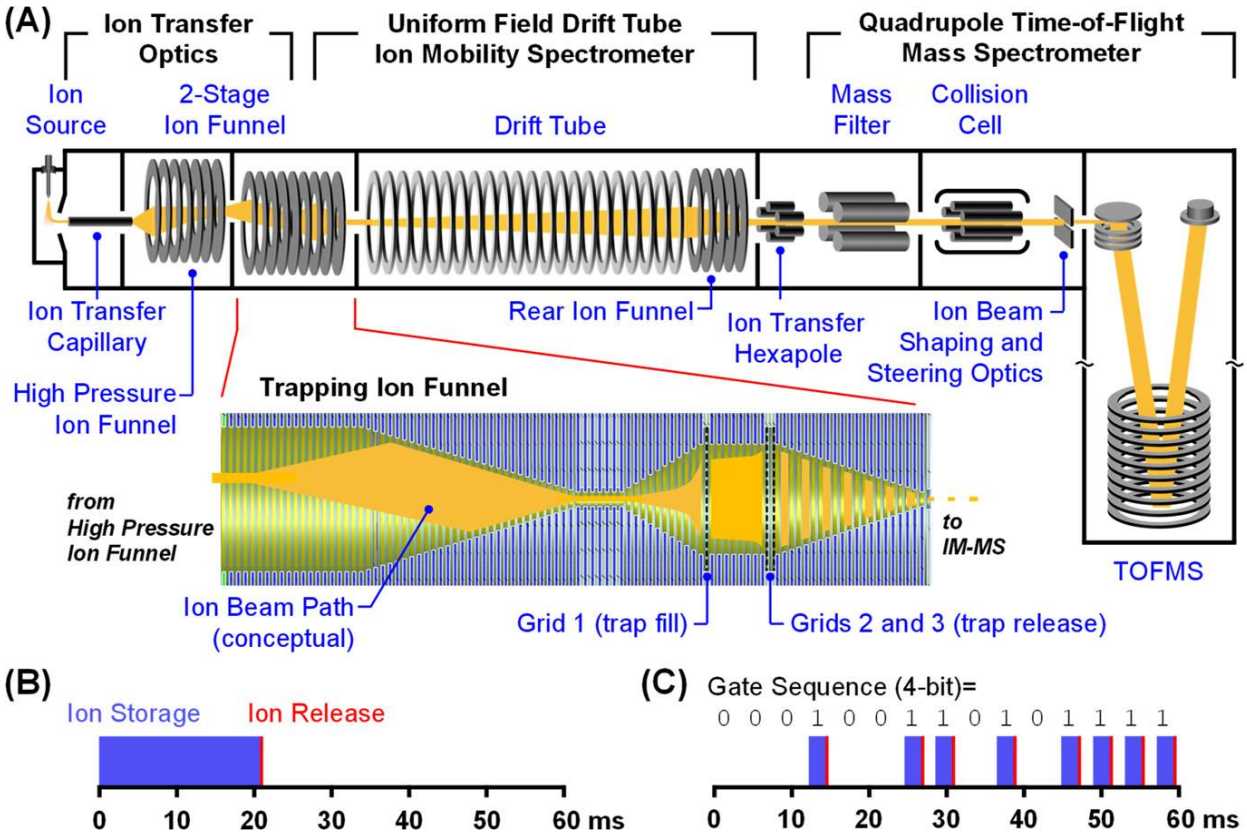

Figure 2.2. (A) Schematic of the IM-MS instrument used in this work. Ion multiplexing is implemented in the trapping ion funnel (inset), where the ion trap release gate (grids 2 and 3) is modulated with a binary sequence. (B) In conventional single pulse operation, a (generally) long ion storage time is followed by a single, quick release of the ion gate for each IM measurement cycle. (C) Ion multiplexing utilizes a series of short store-and-release sequences to introduce multiple, low density ion pulses to the drift tube during each IM cycle.

2.8.1. High-Resolution Demultiplexing (HRdm)

The multiplexing strategy has the advantage that many more data points are added to each measurement cycle compared to "pulse-and-wait" DTIMS. It has been recognized that this additional data can be used in a postprocessing step to improve the effective IMS resolution [93]. The HRdm utilizes a Hadamard transform to enhance the IMS spectra and is only available for use when data are collected in multiplexed mode improving the resolving power from ~60 to between

100 and 200, depending on the ion drift time and signal saturation [93, 95]. The processing of IM data collected in a multiplexed mode with Agilent IM QTOF-MS to improve resolution is described below [77];

1. MassHunter Data Acquisition is used to acquire ion multiplexed data files.
2. The ion multiplexed data file is reconstructed using the PNNL PreProcessor.
3. A targeted feature is generated using MassHunter IM-MS Browser using the ion mobility feature extraction (IMFE) algorithm.
4. Finally, the HRdm is used which utilizes the targeted feature list, the raw multiplexed data, and the reconstructed demultiplexed data in order to perform the peak deconvolution.

Chapter 3. Systematic Optimization of Ambient Ionization Ion Mobility Mass Spectrometry for Rapid Separation of Isomers

3.1. Introduction

Current methods typically used for metabolite screening and disease diagnosis often require extensive sample preparation, which increases analysis time and associated costs. Ambient ionization techniques enable the analysis of various samples in complex matrices with little or no sample preparation in a short time, typically within a minute. Ambient ionization techniques combined with the powerful analytical capabilities of mass spectrometry (MS) have been used for qualitative detection and semi-quantitation of metabolites in complex matrices [96-98], identification of microorganisms [53, 57, 99], therapeutic drug monitoring [100], and rapid agrochemical screening [101]. Although rapid and direct analysis of different samples in complex matrices is possible using ambient ionization-MS techniques, their reduced selectivity poses a challenge for the analysis of complex samples. The reduced selectivity is due to the inability of MS to distinguish isomeric compounds with identical chemical formulae, for instance, constitutional and geometric isomers [58]. Separations based on IM can improve the selectivity of ambient ionization techniques such as paper spray (PS) and leaf spray (LS). Coupling IM with either PS-MS or LS-MS platforms will not only improve the selectivity as a result of separation of isomers but also provide CCS values that act as unique physicochemical properties that can be used for confident identification of metabolites and lipids.

While a few studies have investigated the combination of PS with IM-based separation platforms for various applications such as breast cancer prediction [102], and forensic applications [59, 103-105], there are no reported studies on the coupling of PS or LS with commercially

available DTIMS instruments. In this study, we optimized and demonstrated the coupling of the PS ionization technique with a commercial DTIM–MS instrument for the rapid separation of constitutional pesticide isomers and geometric lipid isomers analyzed separately in the positive and negative ion modes, respectively. Systematic optimization and characterization of the ionization and transmission parameters are reported here. The workflow was extended further to leaf samples by developing the LS–IM–MS platform to enable rapid analysis of pesticide isomers in a leaf matrix with high sensitivity and selectivity. In addition, a new approach to single-field CCS measurements was developed to increase throughput and accuracy and minimize the required measurement time. In addition, ion structures were calculated using computational tools and their associated CCS values were compared with their corresponding experimental values, resulting in reliable identification of the analytes' structures.

3.2. Experimental

3.2.1. Materials and sample preparation

Ultrapure acetonitrile (ACN) and water (H_2O) solvents were purchased from Agilent Technologies (Santa Clara, CA). LC-MS grade chloroform ($CHCl_3$) was purchased from VWR Chemicals (Radnor, PA) while LC-MS grade methanol (MeOH) was purchased from Honeywell (Muskegon, MI). 1,2-dioleoyl-sn-glycero-3-phospho-(1'-rac-glycerol) (sodium salt) PG (18:1(Δ9)/18:1 (Δ9))-Cis, 1,2-dielaidoyl-sn-glycero-3-phospho-(1'-rac-glycerol) (sodium salt) PG (18:1(Δ9)/18:1 (Δ9))-Trans, and 1,2-distearoyl-sn-glycero-3-phospho-(1'-rac-glycerol) (sodium salt) PG (18:0/18:0) were purchased from Avanti Polar Lipids, Inc. (Alabaster, AL). S-(-)-Verapamil Hydrochloride, 6-chloro-2-N,4-N-di(propan-2-yl)-1,3,5-triazine-2,4-diamine (propazine), and 2-N-tert-butyl-6-chloro-4-N-ethyl-1,3,5-triazine-2,4-diamine (terbuthylazine)

were purchased from Sigma-Aldrich (St. Louis, MO). Moreover, low concentration electrospray ionization (ESI) tuning mix was purchased from Agilent Technologies (Santa Clara, CA). All reagents and chemicals were used without additional purification. Whatman grade 1 filter papers were purchased from GE Healthcare Life Sciences (Buckinghamshire, UK) while copper clips were purchased from McMaster-Carr (Chicago, IL).

Stock solutions of the lipid standards (1 μg μL^{-1}) were prepared in $CHCl_3$: MeOH (2:1, v/v) and stored at -20°C for analysis. Then, the stock solutions were diluted in IPA: ACN: H_2O (2:1:1, v/v/v) to a final concentration of 1 ng μL^{-1}. Moreover, 1 μg μL^{-1} stock solution of S-(-)-verapamil was prepared in MeOH: H_2O (50:50, v/v) and diluted to a final solution concentration of 1 ng μL^{-1}. Stock solutions of propazine and terbuthylazine (1 mg mL^{-1}) were prepared in ACN where subsequent dilution was used to reach a final concentration of 1 μg mL^{-1} using 75: 25 ACN: H_2O.

3.2.2. Instrumentation

All experiments were performed using the Agilent 6560 IM–QTOF instrument (Agilent Technologies, Santa Clara, CA) which has been described extensively in Chapter 2. Negative (-) and positive (+) ion spectra were recorded over the range of *m/z* 100 – 1700 in the profile mode, with the TOF operated in high sensitivity mode at ~25,000 resolution. Spectra were acquired using MassHunter Acquisition Software B.09.00 (Agilent Technologies, Santa Clara, CA). The data were first visualized and analyzed using IM–MS Browser B.10.0 before being exported to a spreadsheet (Microsoft Excel) for further analysis. The IM–MS settings used herein are as follows: 0.9 frames/s; 18 IM transients/frame; 60 ms maximum drift time; 600 TOF transients/IM transients; 30,000 μs trap fill time; and 250 V drift tube exit voltage. An Agilent tune mix solution was used

for the daily mass calibration of the instrument and transmission tune to optimize the MS parameters. To study fragmentation patterns, gas-phase ions are analyzed after collision-induced dissociation (CID) in the collision cell using different collision energies (See Table 3.1).

Table 3.1 Collision energies (CE) employed for different ions in the present study.

m/z	CE (Volts)
230.1172	15
455.2904	25
773.5338	35
777.5651	35

3.2.3. Ion sources

Since our commercial instrument uses an ESI source that employs gases at high flow rates and temperatures, we needed to optimize various operational settings to ensure that the ambient ionization sources operate at high efficiency in conjunction with our IM-MS instrument. For the optimization, we used a custom-made nano-ESI source (shown in Figure 3.1A). Briefly, the nanospray tip (New Objective Inc, Littleton, MA) was held by a custom-built holder mounted onto a 3-dimensional moving stage (Thorlabs Inc, Newton, NJ). Sample solutions were infused directly into the instrument using a syringe pump (Fusion 100, Chemyx Inc, Stafford, TX) and a gastight syringe (2.5 mL, Hamilton Corporation, Reno, NV) at a flow rate of 200 nL/min. Different commercially available spray shields were tested because high flow rates and temperatures of the drying gas are expected to hinder the ambient ionizations sources (Figure 3.2) (Agilent Technologies, Santa Clara, CA).

Figure 3.1. Schematic and photographic illustrations of **(A)** custom-made nano-ESI ion source. **(B)** Paper spray ambient ionization source. **(C)** Leaf spray ambient ionization source.

Figure 3.2. Pictures of various nanospray shields used in this work.

For the optimization of the PS ion source, a Whatman grade 1 filter paper was cut into a triangle (10 mm high and 8 mm base width). A copper clip holding the paper triangle was mounted onto a 3-dimensional moving stage with the tip of the paper held in line with the instrument inlet. 1 µL of the sample was spotted directly onto the center of the paper triangle using a micropipette, and the paper was allowed to air dry. The voltage application in this study contrasts previous PS–MS studies where high voltages were applied to the paper clip. We applied a zero V to the paper

via the copper clip connected to the grounded outlet of the mass spectrometer, and the capillary voltage was set to an optimized value of –3.5 kV and +3.5 kV for positive and negative ionization modes, respectively.

Ten microliters of MeOH were then applied to the paper at once using a micropipette, and a new strip of paper was used for each analysis. A photographic detail of the paper spray source is shown in Figure 3.1B. The paper spray parameters optimized include various spray shields, distance from IM-MS inlet, drying gas temperature and flow rate, and capillary voltage. The optimization was performed in three replicates, and the evaluation was based on the intensity of the mass spectra signal and the corresponding spray time.

Red maple (*Acer rubrum*) leaves were collected from the Auburn University campus for LS experiments. The plant leaves were cut into triangles and attached with copper clips, as shown in Figure 3.1C. As with PS, a zero V was applied to the leaf via the copper clip connected to the grounded outlet of the mass spectrometer, while the capillary voltage was set to an optimized value of -3.5 kV for operation in positive ion mode. 1 µL of the pesticide sample solution was spotted onto the triangular leaves, and then various measurements were made.

3.3. Results and Discussion

3.3.1. Optimization of Nano-electrospray ion source

The experimental parameters of the custom-built nano-ESI source were optimized so that it could serve as a continuous ion source for instrument calibration and as a preparation for optimization of ambient ionization sources. Both positive and negative ionization modes were investigated using verapamil and saturated PG (18:0/18:0) lipid, respectively, as they are strongly ionized in these modes. For instance, the PG (18:0/18:0) lipid contains two fatty acyl side chains

and a glycerophosphate head group that can be easily deprotonated, resulting in a strong $[M-H]^-$ signal in the negative ion mode. In the positive ion mode, the PG lipids are only weakly ionized, therefore we chose verapamil, which contains tertiary amine, nitrile, and a phenolic group. These functional groups are easily protonated, resulting in an intense $[M+H]^+$ signal. Experimental parameters for the optimization process included: spray shield, distance from IM–MS inlet capillary voltage (Vcap), the temperature of drying gas, and its flow rate. Several spray shields, were tested, including a single bore inline, an end cap, and a multi bore vortex shield. These spray shields contain radial gas diverters that disperse the drying gas, preventing heated gas from flowing directly to the nanospray tip. The spray shield used for our IM-QTOF (Jet Stream ESI source) does not contain a radial gas diverter making it unsuitable for nano-ESI and ambient ionization sources, as it leads to rapid sample evaporation and poor ion transmission. We found that the vortex spray shield provided the highest ion signals due to its design. It has a wide inlet for an improved ion transmission and two side ports to further deflect the drying gas away from the nano-ESI tip, allowing effective ion transmission without immediate sample evaporation.

An ion signal was observed immediately on the application of the capillary voltage, and the signal disappeared reproducibly once the spray voltage was turned off, as shown in Figure 3.3A. In addition, we varied Vcap (i.e., spray voltage) between -0.5 kV and -4.5 kV in the positive ion mode (Figure 3.3B). We found that the signal intensity associated with verapamil increased gradually with increasing Vcap from -0.5 kV to -3.5 kV. Further increase in Vcap led to a decrease in the detected ion signal which agrees with a previous study [106]. The distance between the nanospray tip and the IM–MS inlet was varied in the range of 5-10 mm (Figure 3.3C). We found that 6 mm was the optimal distance at which the highest ion intensities were obtained, while electrical discharge occurred at a distance of less than 2 mm. At the optimized distance (6 mm),

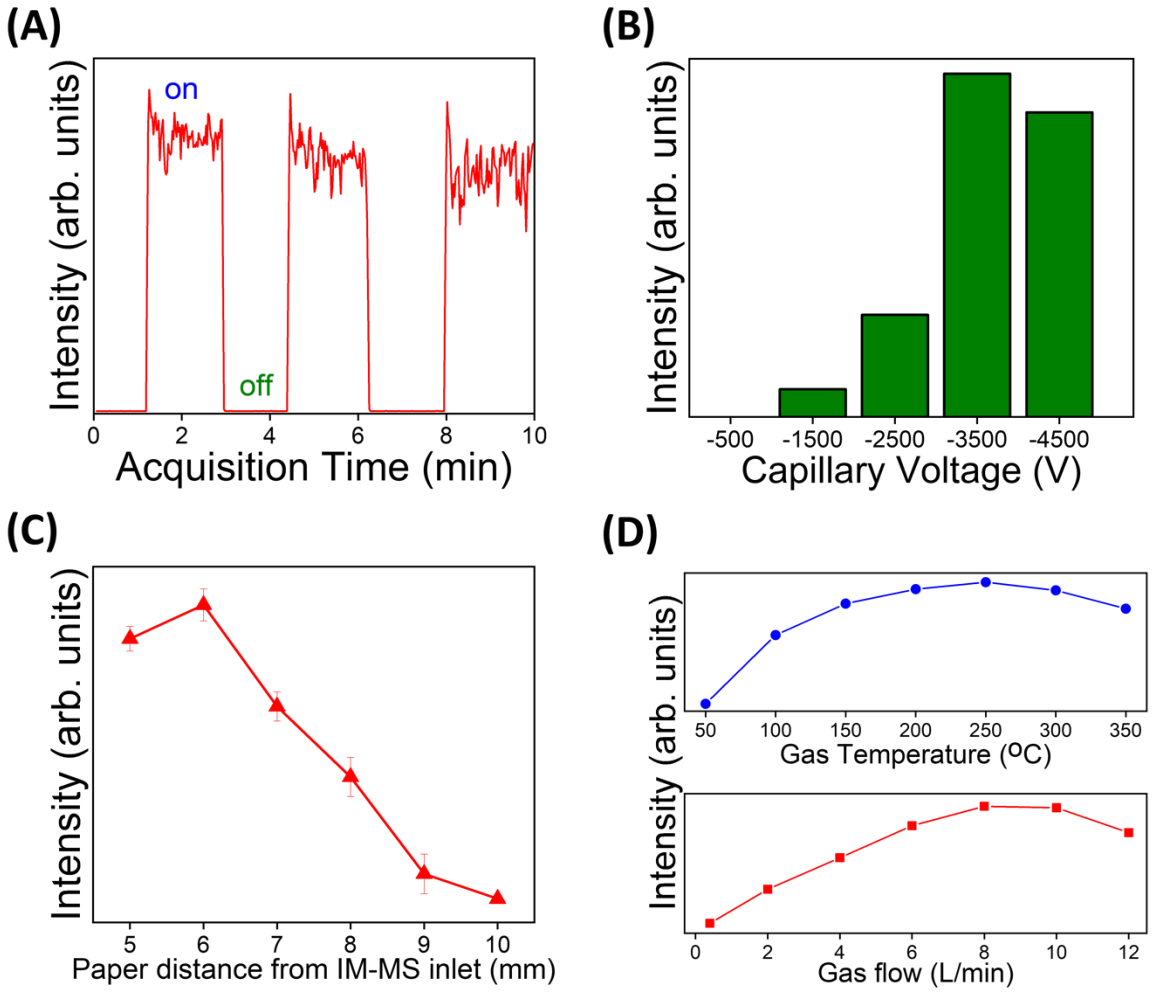

Figure 3.3. Nano-ESI source optimization using S-(-)-verapamil in the positive ion mode under various conditions which include: **(A)** with (On) and without (Off) applied voltage gradient. **(B)** various capillary voltages (Vcap). **(C)** different distances of nano-ESI tip from IM-MS inlet tested. **(D)** various drying gas temperature (top) and flow rates (bottom) on signal intensity.

we observed no signal in the absence of a voltage gradient, while a weak ion signal intensity was observed when he nano-ESI tip was placed at a 2 mm distance from the IM–MS inlet. This weak ion signal was generated by the suction of droplets due to the pneumatic forces of the mass spectrometer vacuum at the inlet [107].

Drying gas temperature and flow rate were the next parameters that we optimized. In the studied gas temperature range of 50℃ to 350℃, the ion signal intensity increased gradually until 250℃ was reached (Figure 3.3D, Top). A further increase in the drying gas temperature to 350℃ resulted in a slight decrease in the ion signal intensity. We attributed this observation to the reduction in ionization efficiency at extremely high temperatures [106]. Furthermore, we investigated the effect of the drying gas flow rate while varying it in the range (0.4-12 l/min) on the detected ion signal (Figure 3.3D, Bottom). Increasing the flow rate of the drying gas is expected to improve the ionization efficiency by enhancing desolvation efficiency. However, very high flow rates reduce ion transmission. 8 L/min was observed as the optimal gas flow rate as it resulted in the highest signal intensities. Noteworthily, the optimization studies that we performed using PG (18:0/18:0) in the negative ion mode resulted in similar observations and conclusions to the positive ion mode studies, as shown in Figure 3.4.

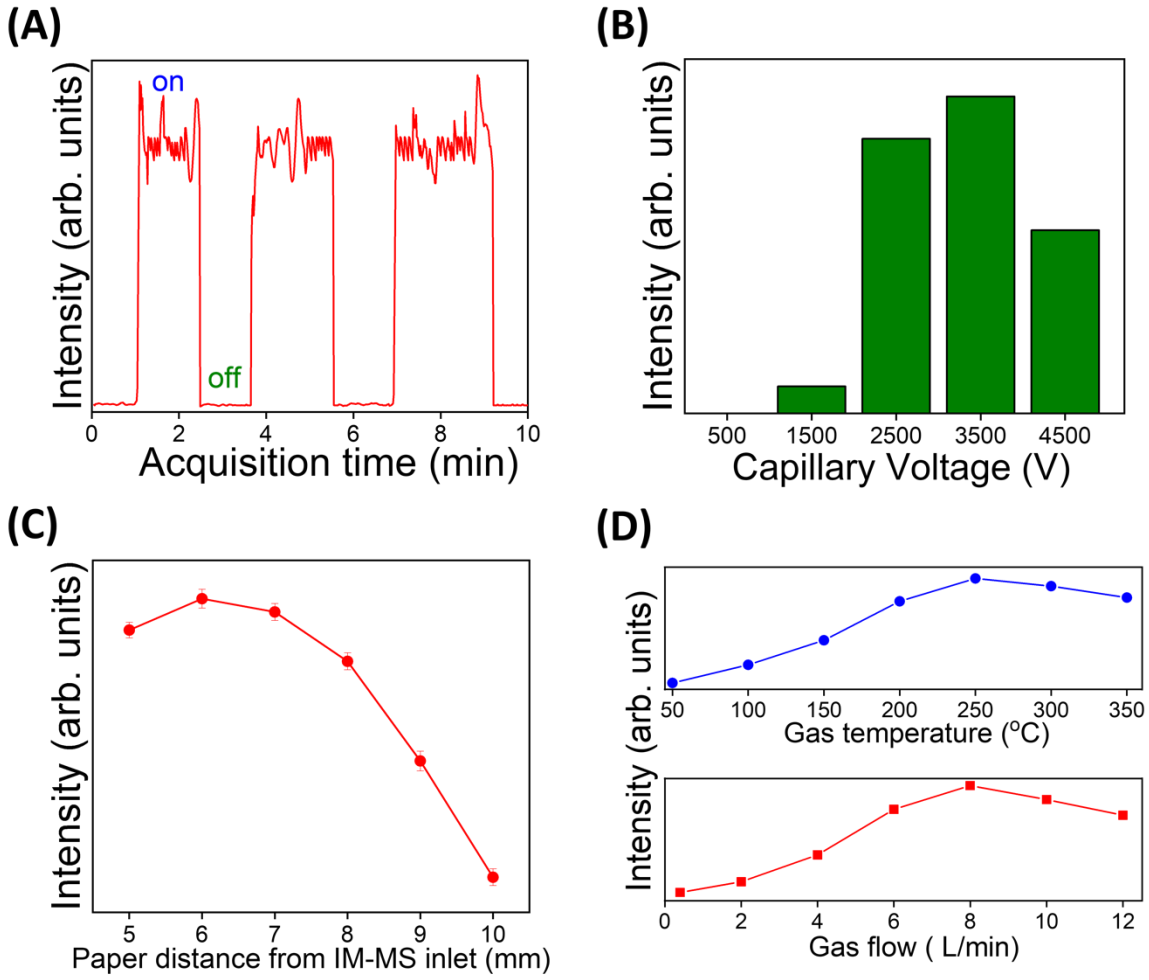

Figure 3.4. Nano-ESI source optimization using PG (18:0/18:0) in the negative ion mode under various conditions which include: **(A)** with (On) and without (Off) applied voltage gradient. **(B)** various capillary voltages (Vcap). **(C)** different distances of nano-ESI tip from IM-MS inlet tested. **(D)** various drying gas temperature (top) and flow rates (bottom) on signal intensity.

3.3.2. Optimization of paper spray ion mobility mass spectrometry workflow

The nano-ESI source was switched to the PS ion source by replacing the nanospray tip with the copper clip paper, extending the parameters optimized for the nano-ESI–IM–MS to the PS–IM–MS platform. The experimental parameters of the PS–IM–MS workflow were further optimized to establish a sensitive, rapid, and robust ionization source for the analysis of various isomers, such as isomeric lipids and pesticides. (S)-(-)-verapamil and PG (18:0/18:0) lipid were

separately examined in the positive and negative ion modes, respectively, because of their strong ionization efficiency in these modes, as explained above. The PS experimental parameters that we optimized include spray shield, distance from IM–MS inlet, Vcap, and drying gas temperature and flow rate. **Figure 3.5** shows the effects of the various experimental parameters on the signal intensity and spray time of (S)-(-)-verapamil in the positive mode.

An ion signal was observed immediately on the application of the spray solvent and voltage, and the signal disappeared reproducibly once the spray voltage was turned off, as shown in Figure 3.5A. In addition, we varied the magnitude of the applied capillary voltage between -0.5 kV and -4.5 kV. As shown in Figure 3.5B, the ion signal reached the highest intensity at an applied voltage of -3.5 kV selected as the optimized voltage for further optimization steps. A significant decrease in the ion signal was observed similar to previous reports upon increasing the Vcap beyond the optimum voltage [108]. Our observations on the effect of varying the spray shield with the paper spray source are consistent with those obtained with the nano-ESI source. The vortex spray shield allowed the transmission of more ions while deflecting more drying gas away from the paper substrate, resulting in higher ion signals and longer spray times than the other spray shields examined in the present study. The end cap and inline spray shields do not have side openings that divert the drying gas from the paper triangle. Therefore, the sample and spray solvent evaporate rapidly which explains their decreased ion signals compared to those observed with the vortex spray shield. Noteworthily, the end cap spray shield resulted in higher ion signals than the inline spray shield, which may be caused by its wider inlet resulting in higher gas-phase ion transmission. As shown in Figure 3.5C, the optimal distance between the IM–MS inlet and the paper spray tip along the x-axis was ~6 mm, and thus was used for further optimization steps. Of

note, electrical discharge occurred at a distance of less than 2 mm, which is consistent with previous studies [109].

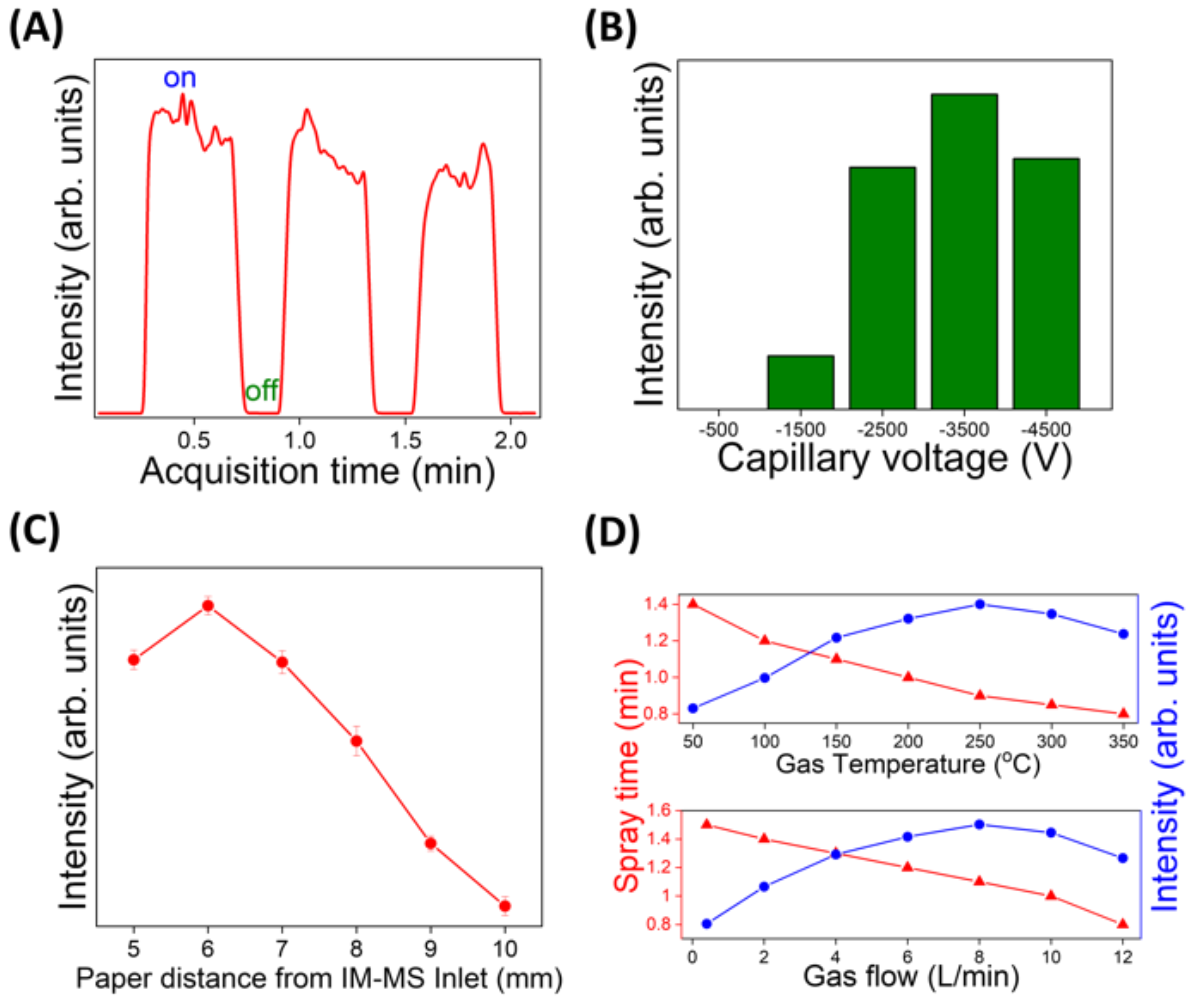

Figure 3.5. Paper spray (PS) ambient ionization source optimization using S-(-)-verapamil in the positive ion mode under various conditions which include: **(A)** with (On) and without (Off) applied voltage gradient. **(B)** various capillary voltages (Vcap). **(C)** different distances of PS tip from IM-MS inlet. **(D)** various drying gas temperatures where the drying gas flow rate was maintained at 5 L/min (top) and flow rates where the drying gas temperature was maintained at 250°C (bottom) on

In addition, the effects of varying the drying gas temperature and flow rate on the analyte ion intensity and spray time were examined as shown in Figure 3.5D. During the spray process, a

portion of the solvent is consumed to transport the samples to the IM–MS inlet while the other portion evaporates [110]. On increasing the drying gas temperature from 50℃ to 350℃, the signal intensity increased gradually until 250℃ was reached (Figure 3.5D, top). The reported increase in the ion signal intensity is associated with the increased evaporation of the solvent from the solvent droplets, which undergoes a subsequent desolvation process that generates more gas-phase ions transmitted into the IM–MS inlet. A slightly reduced ion signal intensity was observed upon a further increase in the drying gas temperature to 350℃.

In addition, upon increasing the drying gas flow rate from 0.4 to 12 L/min, the detected ion signal increased gradually until 8 L/min (Figure 3.5D, bottom). The increase in the ion signal intensity is attributed to the enhancement in solvent evaporation from the solvent droplets by the heated drying gas leading to a subsequent desolvation process generating more gas-phase ions transmitted into the IM–MS inlet. In this study, the optimized drying gas temperature and the flow rate were 250 °C and 8 L/min, respectively. Moreover, the spray time decreased when the drying gas temperature and flow rate increased due to the rapid evaporation of the sample by the drying gas flow. Of note, our optimization studies of PS–IM–MS in the negative ion mode utilizing PG (18:0/18:0) lipid yielded similar results as the studies performed in positive ion mode (Figure 3.6).

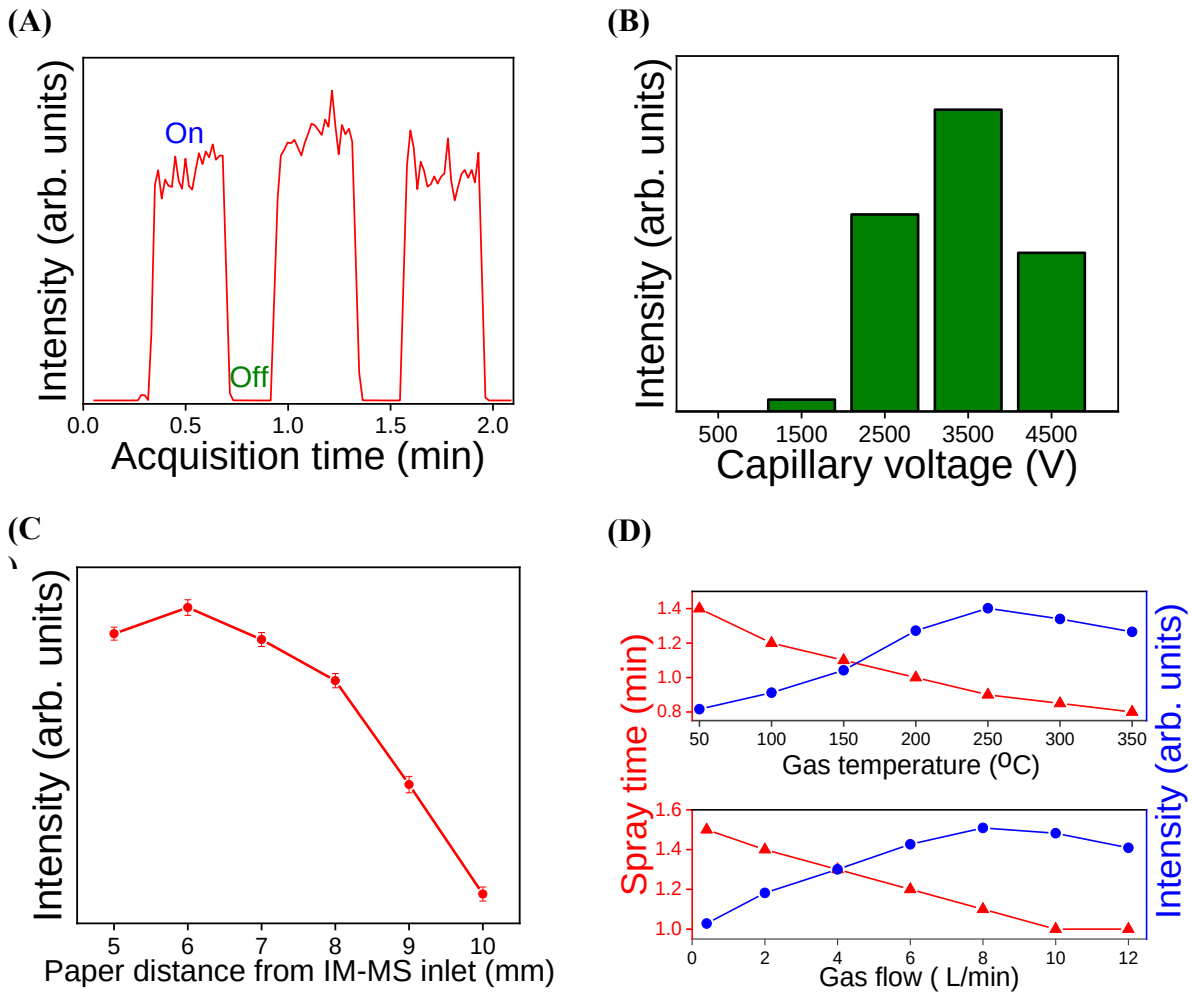

Figure 3.6. Paper spray (PS) ionization source optimization in the negative mode under various conditions which include: **(A)** with (On) and without (Off) applied voltage gradient. **(B)** various capillary voltages (Vcap). **(C)** different distances of PS tip from IM-MS inlet. **(D)** various drying gas temperature (top) and flow rates (bottom) on spray time (red triangles) and signal intensity (blue circles). The sample used for optimization is PG (18:0/18:0) lipid.

We utilized the optimized paper spray source workflow (PS-IM-MS) for the rapid analysis (<1 min) of S-(-)-verapamil and PG (18:0/18:0) in positive and negative ion modes, as shown in Figure 3.7 and Figure 3.8, respectively. The mass spectrum shown in Figure 3.7A shows the verapamil protonated ion as the base peak. We further confirmed the identity of verapamil by CID

experiments, revealing the unique fragment ions as shown in Figure 3.7B [111-113]. The fragment ion at *m/z* 303 was formed by the cleavage of the single bond between α- and β-carbons to the tertiary amine group, resulting in the loss of 152 Da, corresponding to [$C_9H_{12}O_2$]. Successive cleavage of the two longer side chains of the tertiary amino group yielded other fragments, i.e., *m/z* 260 and *m/z* 165 which was the most abundant fragment ion. The subsequent loss of the methyl group from the *m/z* 165 ion resulted in *m/z* 150. Interestingly, the IM analysis of verapamil shown in Figure 3.7D revealed two peaks with drift times of 25.30 ms and 25.90 ms. This bimodal arrival time distribution (ATD) of verapamil is associated with the presence of two different structures in

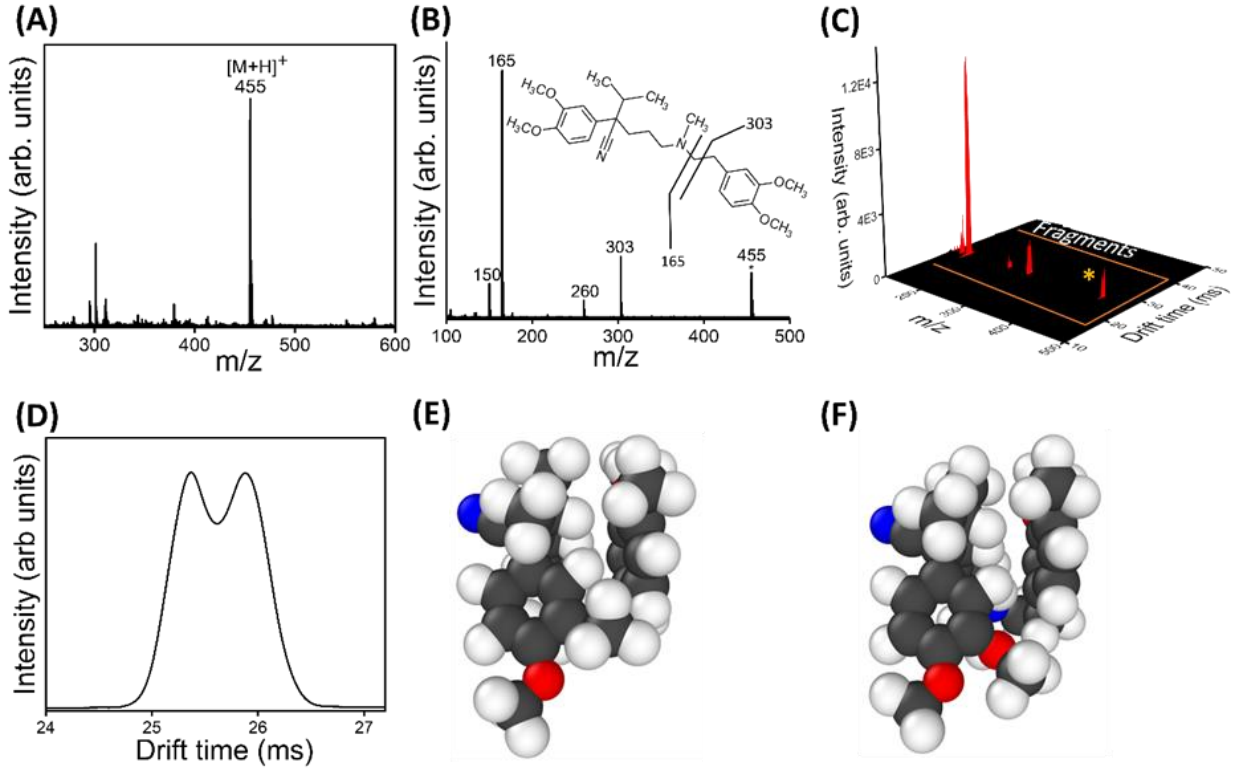

Figure 3.7. The analysis of S-(-)-verapamil using PS–IM–MS in the positive ion mode resulting in: **(A)** mass spectrum. **(B)** tandem mass spectrum. **(C)** ion mobility tandem mass spectra of the drift time aligned fragments and the precursor ion (*m/z* 455, asterisk). **(D)** ion mobility spectrum. Molecular dynamics (MD) structures associated with **(E)** CCS of 214.8 $Å^2$ and **(F)** CCS of 219.9 $Å^2$.

the verapamil ions. The CCS values of the two structures were 205.9 ± 0.6 $Å^2$ and 210.3 ± 0.8 $Å^2$, consistent with previous reports [90, 114, 115]. This suggests a contribution from two distinct conformational structures as our tandem IM-MS analysis (Figure 3.7C) shows the same fragmentation patterns suggesting that these two peaks do not represent protomers [116].

Previous computational studies reported that verapamil is a flexible molecule and recommended using MD simulations to identify its structures [115]. Therefore, we used MD simulations to computationally assign potential theoretical structures to the two experimentally observed IM peaks. As described in the experimental section, we investigated various conformational changes in the 200 theoretically generated structures where two subsets of structures with similar energies were found. Their average CCS values were estimated to be 215.5 ± 2.6 $Å^2$ and 219.9 ± 2.9 $Å^2$. The difference in the theoretically determined CCS values between the 2 clusters is ~4.4 $Å^2$, which is consistent with the CCS difference in the experimental values. Figure 3.7E and Figure 3.7F show the two lowest zero-point energy structures selected to represent the two subsets of MD structures. Verapamil has two ortho-methoxyl anisole groups at opposite ends connected by a 7-atoms backbone chain. In the smaller CCS structure (Figure 3.7E), one of the methoxyl substituents projects outward relative to the vertical plane of the benzene group, resulting in the two methoxyl substituents being 90º to each other and forming a more compact structure with a CCS of 214.8 $Å^2$. In the larger CCS structure, the two methoxyl substituents were fully extended in the downward orientation along the vertical plane of the benzene group, forming a more elongated structure with a CCS value of 219.9 $Å^2$ (Figure 3.7F). The theoretical CCS values agree with the corresponding experimental CCS values resulting in a difference of ~5 %, which lies in the acceptable range of such measurements.

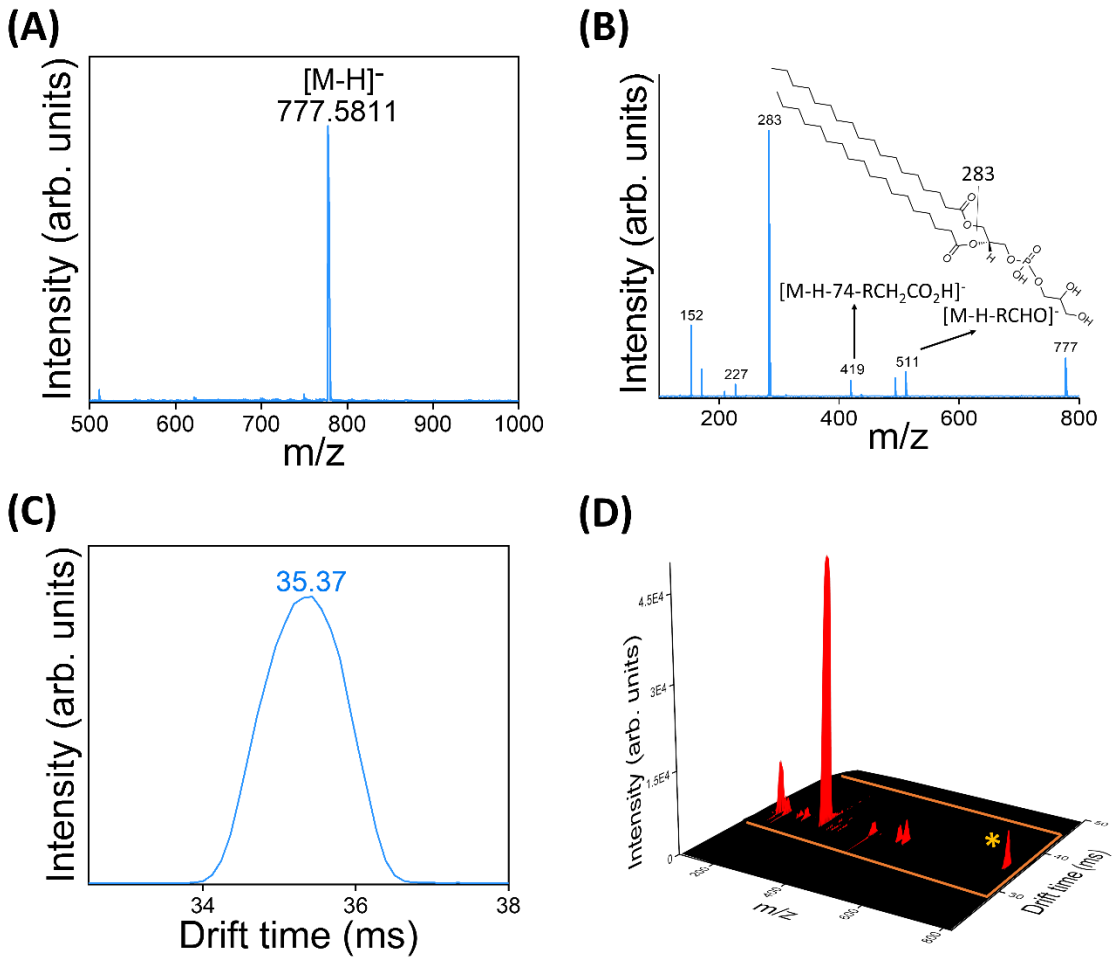

Figure 3.8. The analysis of PG (18:0/18:0) using PS–IM–MS in the negative ion mode resulting in: **(A)** Mass spectrum. **(B)** Tandem mass spectrum (MS/MS). **(C)** Ion mobility spectrum (CCS = 279.5 Å^2). **(D)** Ion mobility tandem mass (IM-MS/MS) spectrum of the drift time aligned fragments and the precursor ion 777.5 m/z (asterisk)

The optimized paper spray source workflow (PS-IM-MS) was also used for the analysis of PG (18:0/18:0) in the negative ion mode. As shown in Figure 3.8A, the peak at *m/z* 777.5811 represents the PG (18:0/18:0) deprotonated ion. The fragmentation pattern is consistent with previous reports of glycerophospholipids (Figure 3.8B) [65]. The product ion at *m/z* 283 corresponds to sn-1 or sn-2 fatty acids (FAs) while the peak at *m/z* 511 results from ketene elimination from the sn-1 or sn-2 position, followed by a neutral loss of water that produces an

additional fragment ion at *m/z* 493. Successive neutral elimination of the head group (glycerol, 74 Da) and one of the FA residues yielded *m/z* at 419. The ion mobility analysis of PG (18:0/18:0), as shown in Figure 3.8C, resulted in a single IM peak at a drift time of 35.37 ms, and using our IM single-field experiment, we measured the CCS value as 279.5 $Å^2$. Our value differs by ~1% from the Lipid CCS Predictor value, which is 276.7 $Å^2$ [117].

3.3.3. Separation of isomers by paper spray and leaf spray ion mobility mass spectrometry

To evaluate the effectiveness of our optimized PS-IM-MS platform in the rapid separation of isomers, we applied it to the analysis of isomeric pesticides (propazine and terbuthylazine) and lipids (cis and trans) in the positive and negative ion modes, respectively. From the mass spectra shown in Figure 3.9, it is clear that measurements based on MS without complementary separations were unable to distinguish these isomers because they have identical chemical formulae leading to the same masses. Although previous reports using LC-MS demonstrated effective separation of these isomers, LC-based analyses require long analysis time, high solvent consumption, and extensive sample preparation [118-121]. Therefore, we used our optimized PS–IM–MS platform to analyze pesticide isomers in the positive ion mode and lipid isomers in the negative ion mode. The analysis using PS–IM–MS was performed in less than 30 seconds, which is sufficient for a complete IM scan and CID measurements.

In positive ion mode, propazine and terbuthylazine were analyzed to investigate the rapid separation of pesticide isomers by the PS–IM–MS platform. Propazine and terbuthylazine are constitutional isomers whose molecular structures differ only in the presence of a methyl group at different positions, resulting in a similar shape and size. Propazine has two isopropyl groups, while

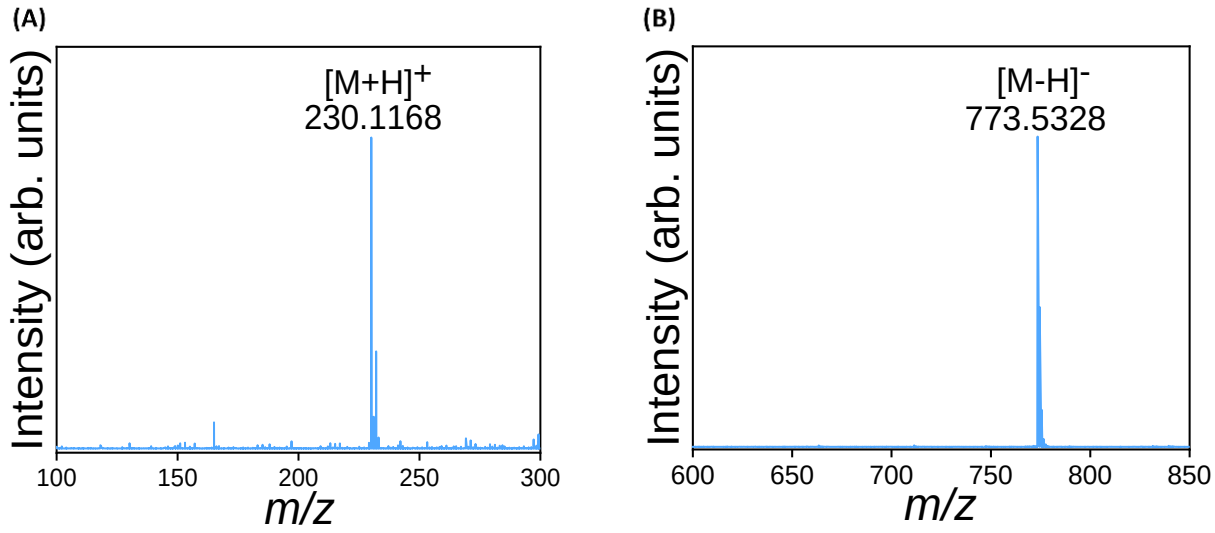

Figure 3.9. Mass spectra obtained from the PS-MS analysis of **(A)** a mixture of constitutional isomeric pesticides (terbuthylazine and propazine) in the positive ion mode. **(B)** a mixture of geometrical isomeric lipids (cis and trans) PG (18:0/18:0) in the negative ion mode

terbuthylazine has one tert-butyl and one ethyl group (Figure 3.10A). As shown in Figure 3.10B, the drift times of terbuthylazine and propazine were 18.63 ms and 18.74 ms, respectively. The two pesticides had a drift time difference of ~0.6%, which corresponds to a CCS difference of less than 1.0%, resulting in a slight separation in the IM dimension. We attribute the IM separation to the larger molecular size of the two isopropyl groups of propazine, leading to more collisions with the buffer gas molecules and thus a longer drift time than for terbuthylazine. This observation was also confirmed by computational studies of the gas-phase structures, as discussed below.

Extensive characterization of isomeric lipids is crucial because previous studies have linked altered lipid metabolism to several important human diseases, including obesity [122], diabetes [123], neurodegenerative disorders [124], and autoimmune diseases [124]. Geometric isomers, particularly the industrially produced, *trans* isomers, have been associated with individual risks for the development of metabolic disease, cardiovascular disease, stroke, and colon cancer in contrast to naturally occurring *cis* isomers [118, 125]. Geometric isomers differ in their structures

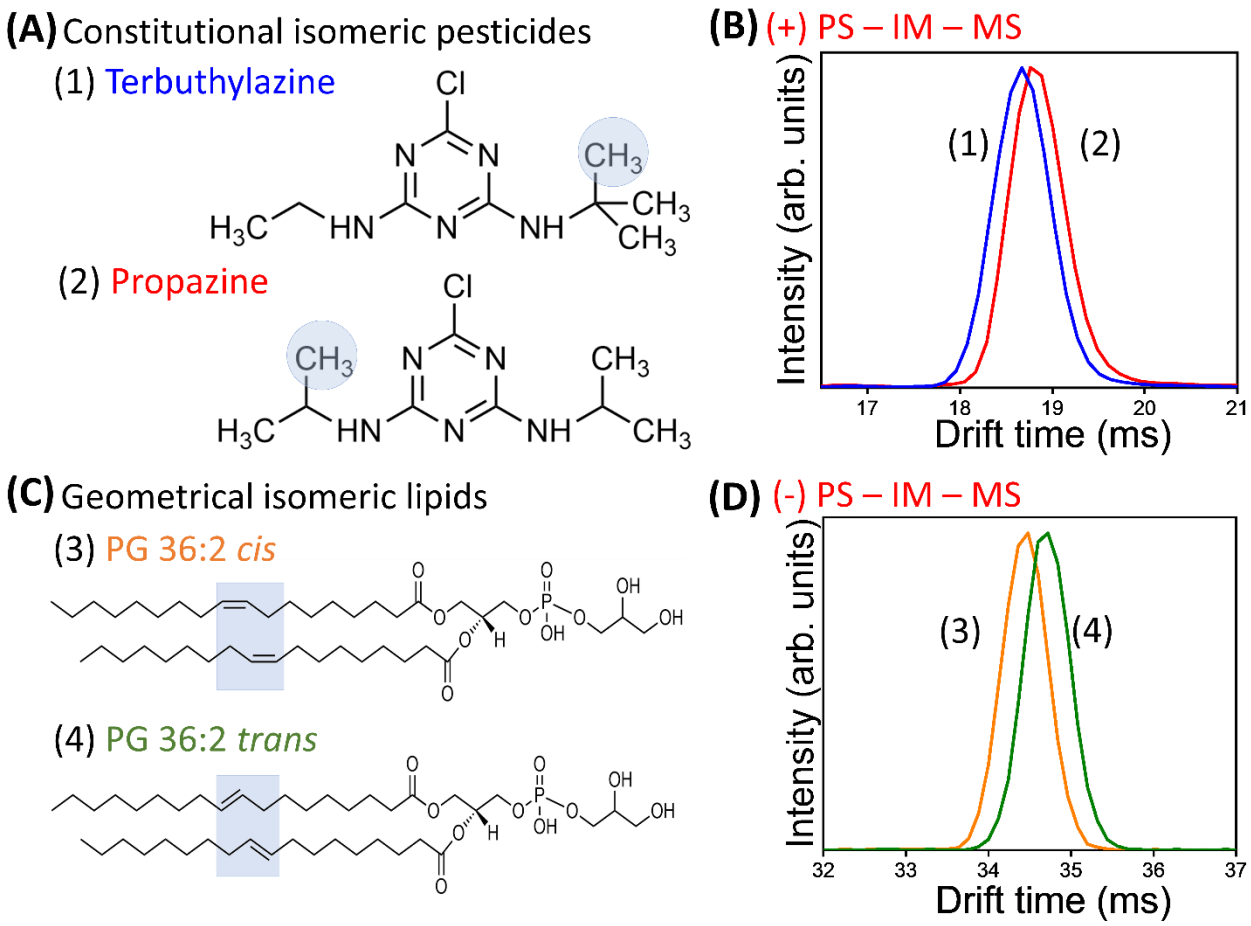

Figure 3.10. **(A-B)** PS–IM–MS analysis of constitutional isomeric pesticides (terbuthylazine and propazine) where the structures are shown in **(A)**, and the IM separation is shown in **(B)**. **(C-D)** PS–IM–MS analysis of geometric isomeric lipids (cis and trans PG (18:1/18:1)) where the structures are shown in **(C)**, and the IM separation is shown in **(D)**.

by the configuration of the double bonds. To examine the capability of our PS–IM–MS platform to separate the geometric isomers, the PG (18:1/18:1) Δ9-cis and PG (18:1/18:1) Δ9-trans isomeric lipids were analyzed separately in the negative ion mode (Figure 3.10C and Figure 3.10D). We observed the IM–peaks of the cis and trans isomers at 34.67 ms and 34.92 ms, respectively. From our single-field IM experiment, CCS of 276.2 ± 0.4 $Å^2$ and 278.3 ± 0.6 $Å^2$ were obtained for PG (18:1/18:1) Δ9-cis and PG (18:1/18:1) Δ9-trans isomeric lipids, respectively. The IM separation

between the *cis* and *trans* isomers is consistent with previous studies that used similar ion mobility platforms [126, 127]. This observation demonstrated that the IM separation is not affected by the paper substrate. The IM separation can be explained by their conformational differences, as reported previously that the *cis*-orientation of the double bonds results in a more corrugated backbone, whereas the trans geometry has a more open conformation [126].

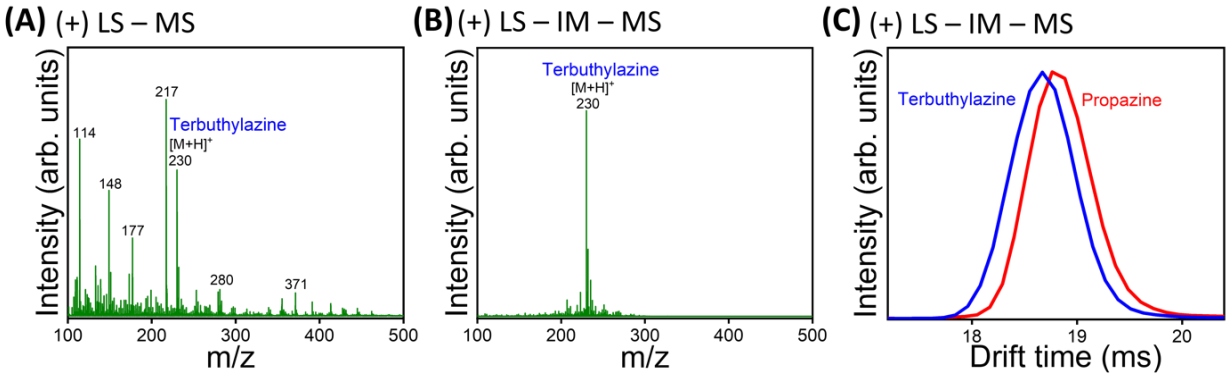

Figure 3.11. **(A)** Mass spectrum obtained after Leaf spray–MS analysis of terbuthylazine. **(B)** Mass spectrum obtained after Leaf spray– MS analysis of terbuthylazine with filtered drift time of 18.63 ± 0.10 ms. **(C)** Leaf spray–IM–MS analysis of terbuthylazine and propazine.

We extended the optimized PS–IM–MS workflow to leaf samples as leaf spray-ion mobility-mass spectrometry (LS–IM–MS). This leaf spray-based workflow rapidly separates isomers in complex matrices, demonstrating the effectiveness of our ambient ionization-IM-MS methods. The two pesticides: namely, propazine and terbuthylazine, were added separately onto a triangle cut from a plant leaf, and ion mobility spectra were acquired for both isomers. Figure 3.11A shows a complete MS scan of 1 µL of terbuthylazine (*m/z* 230.1168) spotted on the leaf triangle. The mass spectrum showed many unidentified ions due to several matrix interferences, such as plant metabolites and external pesticides present in the leaf. These interferences and high background noise resulted in a low S/N ratio of the analyte. We observed an increase in S/N of the

analyte when the mass spectra were filtered using the drift time of the analyte (18.63 ± 0.10 ms), as shown in Figure 3.11B.

This observation demonstrates the powerful analytical capabilities of IM to remove matrix interference and reduce background noise, resulting in higher selectivity and lower limits of detection. Our findings demonstrate that using IM with ambient ionization–MS can improve the accuracy of quantitation measurements in complex matrices by lowering the detection limit. These findings are consistent with previous studies reporting the effect of coupling IM with ambient ionization on the overall S/N ratios obtained for different sample ions and detecting the low abundance ions in the presence of high abundance ions [128]. Our results encourage the potential use of the LS–IM–MS platform for the rapid screening of pesticides in agricultural products and PS–IM–MS for detecting pathogens in clinical and food samples. We observed the terbuthylazine and propazine drift time peaks at 18.64 ms and 18.76 ms resulting in CCS values of 153.8 ± 0.2 $Å^2$ and 154.9 ± 0.3 $Å^2$, respectively (Figure 3.11C).

These CCS values were similar to those obtained by the PS–IM–MS workflow (with < 0.1% difference). Moreover, the IM-based separation was maintained in the analysis of pesticides in the leaf sample achieving a similar separation to that obtained in the paper spray experiment. These findings demonstrate that the drift time, CCS values, and the IM separation are unaffected by complex matrices highlighting the positive characteristics of ambient ionization–IM as chemically independent separation platforms. Computational structural studies were performed to identify the structures of the pesticide isomers. We obtained CCS values of 156.6 $Å^2$ and 157.7 $Å^2$ for the lowest energy structures of terbuthylazine and propazine, respectively. These theoretical CCS values resulted in a difference of ~2% from the experimental CCS values. Figure 3.12 shows the low-energy structures obtained from the DFT computational studies alongside their CCS values

and relative energies. Therefore, the combination of ion mobility CCS measurement and theoretical structure calculations can reveal the structures of the analyte ions obtained experimentally.

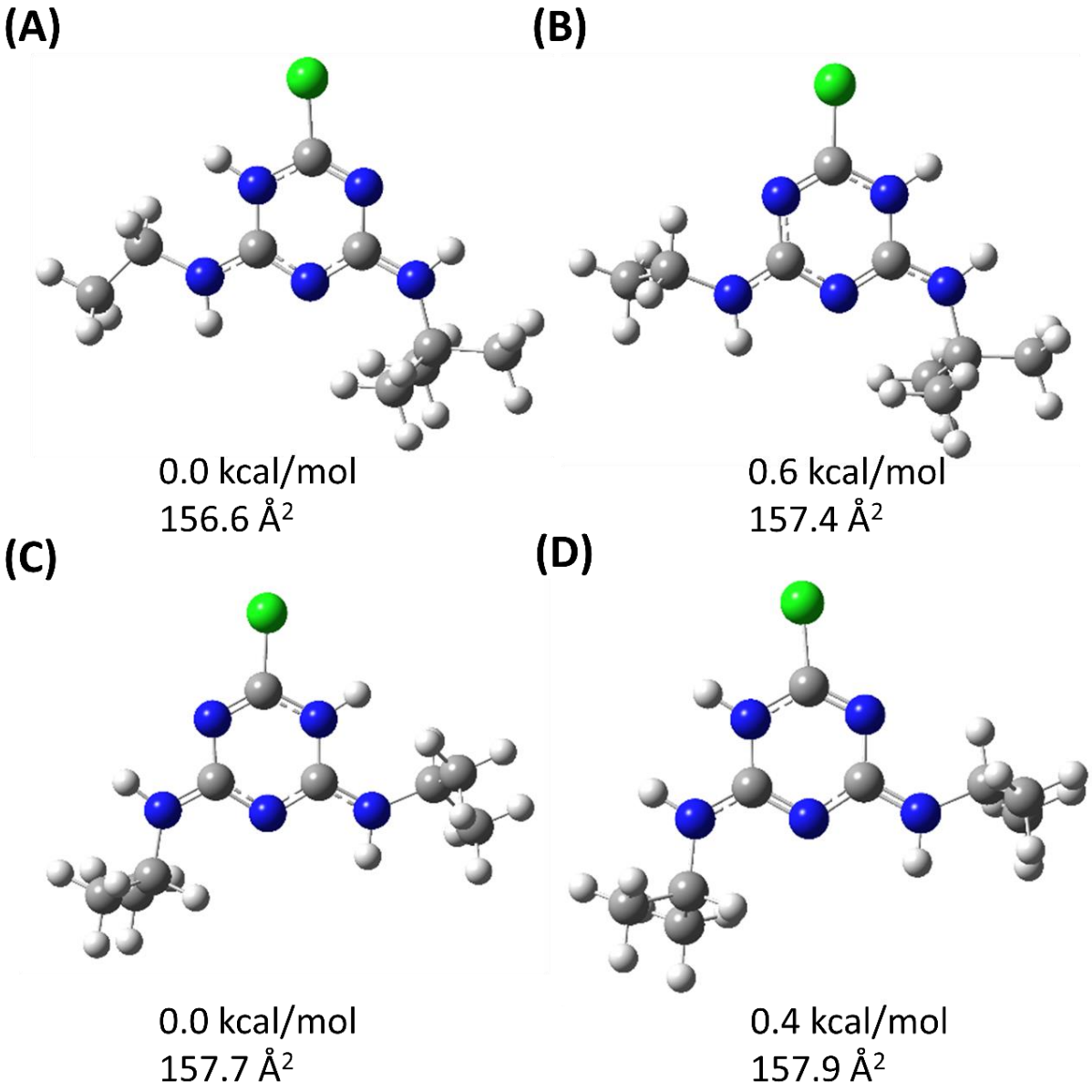

Figure 3.12. Optimized structures of **(A-B)** terbuthylazine and **(C-D)** propazine with their relative energies (kcal/mol) at B3LYP/6-31G(d,p) level of theory and their corresponding collision cross section values.

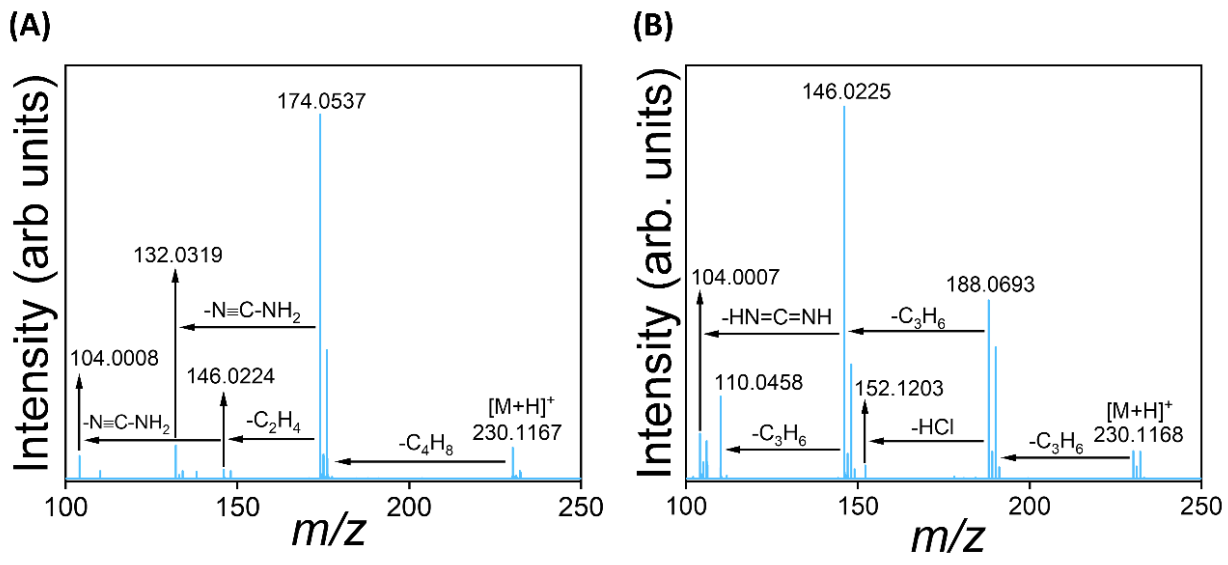

Figure 3.13. Tandem mass spectra obtained by the analysis of **(A)** terbuthylazine and **(B)** propazine using PS-IM-MS/MS.

Since IM separation occurs before fragmentation in the collision cell, accurate alignment of the fragment ions with their corresponding precursor ions is possible based on their corresponding drift times [129]. We observed significant differences in the fragmentation spectra of the two pesticides, terbuthylazine and propazine. This difference in the MS/MS spectra is because they are constitutional isomers (Figure 3.13).

For instance, *m/z* 132.0319 and 174.0540 correspond to the unique fragment ions of terbuthylazine, whereas the ions at *m/z* 152.1203 and 188.0694 correspond to distinctive fragment ions of propazine [130, 131]. The characteristic terbuthylazine fragment ion at *m/z* 174 corresponds to the loss of the side-chain, 2-methylprop-1-ene with γ-hydrogen migration to the adjacent amino group, and the other characteristic fragment ion at *m/z* 132 was formed from the ring-opening of the triazine without the loss of the ethyl side chain. Whereas the characteristic propazine fragment ion at *m/z* 188 corresponds to the cleavage of the isopropyl group with hydrogen migration to the adjacent amino group, while the other unique fragment ion at *m/z* 152 was formed by the

successive loss of HCl from the triazine group of *m/z* 188. The fragmentation features common to the MS/MS spectra of the two pesticides include fragment ions at *m/z* 104.0007, 110.0458, and 146.0224. Successive cleavage of both side-chain alkyl groups by γ-hydrogen migration gives the product ion at *m/z* 146 for both propazine and terbuthylazine, while subsequent ring-opening with the loss of HN=C=NH leads to the fragment ion at *m/z* 104 for both triazines. According to previous studies, the fragment ion at *m/z* 110 is formed via different fragmentation pathways [130, 131]. We observed no differences in MS/MS and IM–MS/MS spectra between the two workflows of ambient ionization ion mobility spectrometry, PS–IM–MS/MS and LS–IM–MS/MS, demonstrating the robustness of these techniques in the analyses of complex matrices.

3.3.4. Direct CCS Measurements

To minimize the needed analysis time and increase accuracy, we developed a new approach to conduct single-field CCS measurements. In the traditional single-field method, the IM-analysis of the calibrant tune mix ions is performed first with a single electric field, and their drift times are measured. Afterward, the analyte samples are run under the same single-field settings as those used for the calibrant ions [84]. From the linear regression of the calibrant drift times and CCS values, the experimental CCS values the analyte are obtained [85].

In this study, we performed IM measurements on a mixture of the calibrant and analytes in one step, analyzing them simultaneously. Verapamil and PG (18:0/18:0) were studied in the positive and negative ion modes, respectively, for the CCS experimental measurements. **Figure 3.14**A and **Figure 3.14**B show ions at *m/z* 322, 622, 922, 1222, 1522 corresponding to the tune ions, while the *m/z* 455 ions with corresponding drift times of 25.25 ms and 25.84 ms represent the verapamil analyte ions. IM–MS browser (Agilent, B.10.0) was used to plot the linear regression

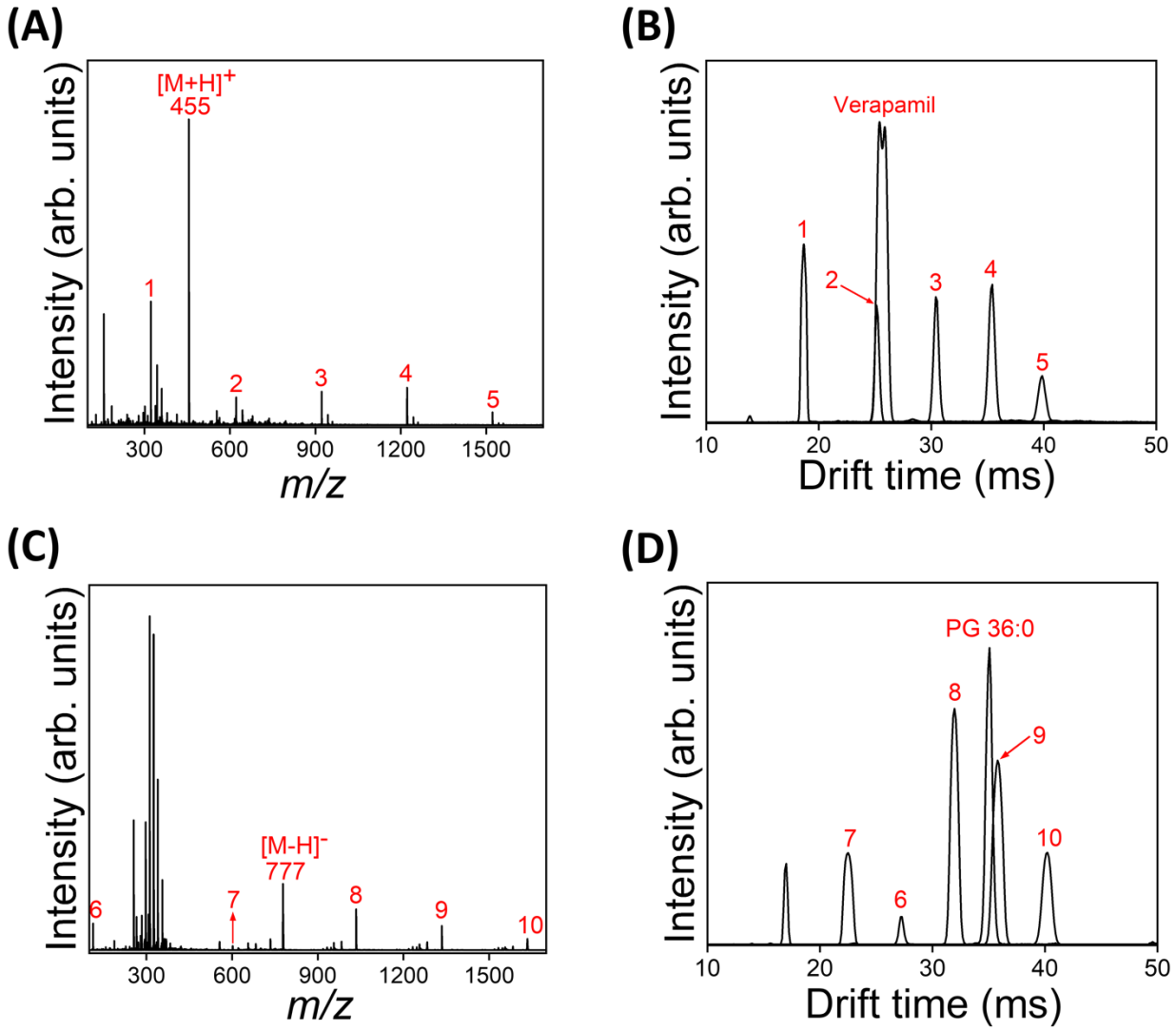

Figure 3.14. CCS Measurements by the direct method introduced in the present study: **(A)** Mass spectra of verapamil and calibrant ions. **(B)** Ion mobility spectra of verapamil and calibrant ions. **(C)** Mass spectra of PG (18:0/18:0) and calibrant ions. **(D)** Ion mobility spectra of PG (18:0/18:0) and calibrant ions. Calibrant ions are obtained from the ionization of low concentration ESI tune mix; they are labeled 1-10.

of the calibrants' CCS values and drift times so that the drift times of the analyte are converted to their corresponding CCS values. This method reduces the time required to perform an analysis because it does not require multiple measurements. In addition, it minimizes experimental errors

caused by variations between measurements. The CCS values of verapamil obtained by our new method were found to be 206.0 ± 0.6 $Å^2$ and 210.5 ± 0.8 $Å^2$. These values agree well with those obtained by the traditional single-field method (205.9 ± 0.6 $Å^2$ and 210.3 ± 0.8 $Å^2$), whereas the stepped field method resulted in CCS values of 205.7 ± 0.2 $Å^2$ and 210.3 ± 0.2 $Å^2$ for verapamil structures (**Table 3.2**). However, ionization suppression effects may be introduced by the simultaneous ionization of the analyte and calibrants which will lead to reduced sensitivity [44].

PG (18:0/18:0) was investigated for CCS measurement in the negative ion mode using our direct CCS measurement method. The MS and IM spectra are similar to those obtained in the positive ion mode, as shown in Figure 3.14C and Figure 3.14D. The %CCS difference between the new single-field, traditional single-field, and stepped-field CCS measurement methods were estimated to be less than 0.15% and 0.25% in the positive and negative ion modes, respectively as shown in Table 3.2. Moreover, the CCS values obtained with the new method were within a relative standard deviation (RSD) of 0.5% between the different measurements, which is consistent with the CCS values obtained with the traditional single-field CCS measurement (0.54% RSD) [85].

Table 3.2 Comparison of the CCS values obtained by the new single-field measurements developed in this work with those obtained by the traditional single-field and stepped-field methods.

	1. New Single-field method	2. Traditional Single-field method	3. Stepped-field method	% Difference (1 and 2)	% Difference (1 and 3)
S-(-)-Verapamil	206.0 ± 0.29 %	205.9 ± 0.29 %	205.7 ± 0.10 %	0.05 %	0.15 %
	210.5 ± 0.38 %	210.3 ± 0.38 %	210.3 ± 0.10 %	0.10 %	0.10 %
PG 36:0	280.2 ± 0.25 %	279.5 ± 0.28 %	280.0 ± 0.15 %	0.25 %	0.07 %

3.4. Conclusions

In summary, this study reports the successful coupling of paper spray and leaf spray ambient ionization techniques to ion mobility mass spectrometry and their applications in the separation of constitutional isomeric pesticides and geometric isomeric lipids analyzed in the positive and negative ion modes, respectively. Ambient ionization techniques allow direct introduction and ionization of samples with minimal sample preparation requirements, while ion mobility spectrometry offers the ability to separate isomeric compounds on the order of milliseconds, leading to the development of efficient ambient ionization–IM–MS workflows that are rapid, sensitive, and highly selective. We reported that IM-based experiments resulted in the separation of the isomeric pesticides and lipids using the paper spray as the ion source. In addition, the leaf spray–IM–MS platform was proven to identify and separate isomers in complex matrices, e.g., plant leaves, demonstrating the robustness of the workflow for complex biological and environmental samples.

In addition to the improved signal-to-noise ratio and the removal of matrix interference due to ion mobility separations, IM measurements also provide unique physicochemical properties, i.e., CCS values that describe the structures. CCS values are measured traditionally by either calibrant-dependent (single-field) or calibrant-independent (step-field) approaches. We have developed a one-step approach to single-field CCS measurements and examined it in the positive and negative ion modes. This new approach offers numerous advantages, such as higher accuracy and throughput and shorter analysis time. We have identified the experimental structures by comparing their CCS values with those obtained using DFT and MD theoretical studies. Our results showed that the integration of ambient ionization methods and ion mobility spectrometry techniques is very promising for rapid pesticide screening in agricultural products and rapid

identification of microorganisms in clinical samples. For instance, our optimized LS-IM-MS workflow can be used to investigate the structure of various phytochemicals present in medicinally important plants.

Chapter 4. Species-Level Discrimination of Microorganisms by High-Resolution Paper Spray – Ion Mobility – Mass Spectrometry

4.1. Introduction

There is a projection of 10 million deaths per year by 2050 due to antimicrobial resistance, highlighting the need for rapid detection and accurate identification of microorganisms. Despite the efficiency of typical identification methods, such as enzyme-linked immunosorbent assay (ELISA) [132, 133] and polymerase chain reaction (PCR) [134], they are labor-intensive, time-consuming, and expensive. Therefore, developing alternative methods that would enable higher throughput and less labor-intensive analyses is needed [8]. The combined advantages of sensitivity, specificity, and speed make mass spectrometry (MS) an attractive analytical platform for the analysis of intact microorganisms [135, 136]. MS analysis of bacteria has been largely achieved using matrix-assisted laser desorption ionization-mass spectrometry (MALDI-MS), a powerful tool in the clinical microbiology field [137]. In addition, the introduction of ambient ionization methods such as paper spray (PS) has enabled rapid analysis of microorganisms with minimal sample preparation requirements based on metabolic and lipid profiles [45, 138]. However, PS-MS suffers reduced selectivity which is caused by the inability of MS to distinguish isomers with identical chemical formulae which poses a challenge for species and sub-species bacterial discrimination. Hence the need to couple ion mobility to PS to increase the selectivity of the method.

Although previous reports illustrated that the PS-MS technique is successful in discriminating various microorganisms utilizing their lipid and metabolic profiles, long incubation periods (~ 24

-48 hours) were needed before a successful analysis [53, 57, 139, 140]. Herein, we optimized and examined paper spray-ion mobility-tandem mass spectrometry (PS-IM-MS/MS) methods to distinguish five *Bacillus* species rapidly and unambiguously to the species level directly in ~1-2 minutes runs after only 4 hours of incubation time. In addition, we measured the collision cross section (CCS) values that act as unique physicochemical descriptors of various biomarkers (e.g., phospholipids and surfactins) which leads to their unambiguous identification. To extract relevant chemical features from a large amount of mass spectral information, multivariate statistical methods are employed. Specifically, in this study, principal component analysis (PCA) was conducted to explore the difference among species and the contribution of each feature. After dimension reduction by PCA, linear discriminant analysis (LDA) was applied to classify different species. To explore whether including IM in the PS-MS/MS workflow would improve the efficiency of species differentiation, we compared the classification accuracy of the model with and without the consideration of IM information in both positive and negative ion modes.

4.2. Experimental

4.2.1. Materials and sample preparation

LC-MS grade isopropanol (IPA) and 3-[(3-Cholamidopropyl)-dimethylammonio]-1-propanesulfonate (CHAPS) were purchased from Sigma-Aldrich (St. Louis, MO USA) while LC-MS grade methanol (MeOH) was purchased from Honeywell (Muskegon, MI). The liquid culturing media, Luria broth (LB) was purchased from VWR Chemicals (Radnor, PA). Moreover, a low concentration ESI tuning mix was purchased from Agilent Technologies (Santa Clara, CA). All reagents and chemicals were used without additional purification. Glass fiber filter papers (0.3

μm pore size) were purchased from Advantec MFS, Inc. (Dublin, CA). Copper clips were purchased from McMaster-Carr (Chicago, IL).

4.2.2. Microorganism Culturing

Five *Bacillus* species isolates (*B. velezensis* (JJ334), *B. subtilis* (JM553), *B. thuringiensis* (JJ218), *B. pumilus* (JJ1622), and *B. altitudinis* (JJ1138)) were gifted by Dr. Douglas Goodwin (Department of Chemistry and Biochemistry Department, Auburn University) and Dr. Mark Liles (Department of Biological Sciences, Auburn University) and stored at -80 ℃. The bacteria were aliquoted from frozen glycerol stocks into Luria broth using sterile pipette tips. The liquid cultures were incubated in a VWR forced air incubator (Chicago, IL) under shaking conditions (220 rpm) at 37℃ for 4-16 hours. All bacterial culturing activities were performed in a biological safety cabinet (Labconco, Kansas City, MO), and biohazardous materials were autoclaved.

4.2.3. Instrumentation

All experiments were performed using the Agilent 6560 IM-QTOF instrument (Agilent Technologies, Santa Clara, CA) coupled with an optimized paper spray ion source as shown in Figure 4.1. The instrument has been described in detail above, so only a brief description is given here. Following our previous optimization efforts, we maintained the drying gas temperature and flow rate at 250 ℃ and 8 L/min, respectively while the ion source voltages were set as follows: capillary voltage 3500 V, Fragmentor 400 V, and Octopole RF 750 V [86]. All ion mobility spectra were acquired using a pseudorandom 4-bit sequence (multiplexing mode); the settings are listed in Table 4.1. In the multiplexing mode, several ion packets are pulsed into the drift tube during each data acquisition cycle (e.g., eight ion packets are injected during one scan interval), increasing the ion utilization efficiency within the same dwell time [93]. Product ion (MS/MS) scans were acquired in a data-dependent mode in which the precursor ions are fragmented only if their

intensities are above a certain threshold utilizing the settings listed in Table 4.1. Spectra were acquired using MassHunter Acquisition Software B.09.00 (Agilent Technologies, Santa Clara, CA).

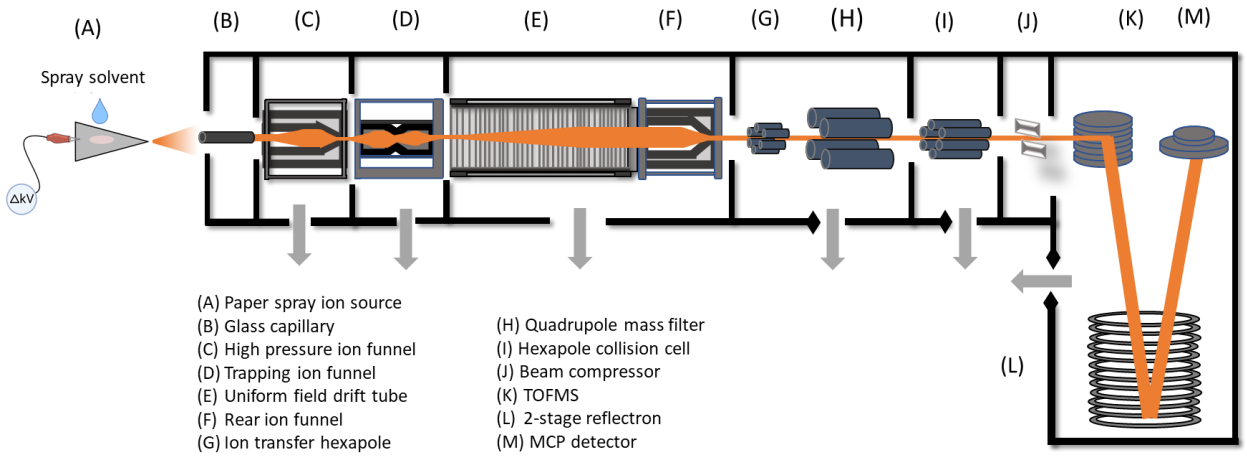

Figure 4.1. Ion mobility – Quadrupole Time of Flight – Mass Spectrometry (Agilent 6560) instrument coupled with an optimized paper spray (PS) ion source.

Table 4.1. Ion mobility and tandem mass spectrometry (MS/MS settings)

IM-MS settings

Parameter	Value	Units
Trap Fill Time	3900	µs
Trap Release Time	200	µs
Frame Rate	0.9	Frames/sec
IM Transient Rate	18	IM Transients/Frame
Max Drift Time	60	Ms
TOF Transient Rate	496	Transients/ IM Transients
Drift Tube Entrance	1700	V
Drift Tube Exit	250	V
Rear Funnel Entrance	240	V
Rear Funnel Exit	43	V
Pulsing Sequence Length	4	bit

Tandem Mass spectrometry settings

Parameter	Value	Units
Collision Energy	35	V
MS acquisition rate	1	Spectra/s
MS transient/spectrum	8133	Transient/spectrum
MS/MS acquisition rate	0.9	Spectra/s
MS/MS transient/spectrum	8978	Transient/spectrum
Max precursor per cycle	10	
Cycle time	12.2	Sec
Static Exclusion Range	100 - 300	
Mass range	100 - 1700	
Precursor Abs. Threshold	200	Counts

4.2.4. Paper Spray Ambient Ionization

For rapid detection and discrimination of bacteria, we introduced a rapid method that implements a short culturing time and less than 2 minutes analysis time. Due to the large pore size (greater than bacteria cell size) of the typical PS filter papers (Whatman 1), glass fiber filter papers with significantly smaller pore sizes (~0.3 µm) were utilized to filter bacterial cells out of the growth liquid media prior to MS analysis. As described in Figure 4.2, 8 mL of the cultured bacteria in LB were filtered through the glass fiber using a Büchner funnel, and the filter paper was allowed to dry at ambient temperatures for about 15 minutes. Then, the glass fiber was cut into several triangles of approximately 8 mm base width and 10 mm height, placed at an optimal distance (~ 6 mm) from the IM-MS inlet, followed by the application of spray solvents and high voltage to generate electrospray [86]. 40 µL of the spray solvent was added which enabled the extraction of various analytes and efficient paper spray ionization. The ions were then transported into the IM-MS inlet because of the pressure and voltage gradients followed by IM spectra and MS/MS spectra acquisition.

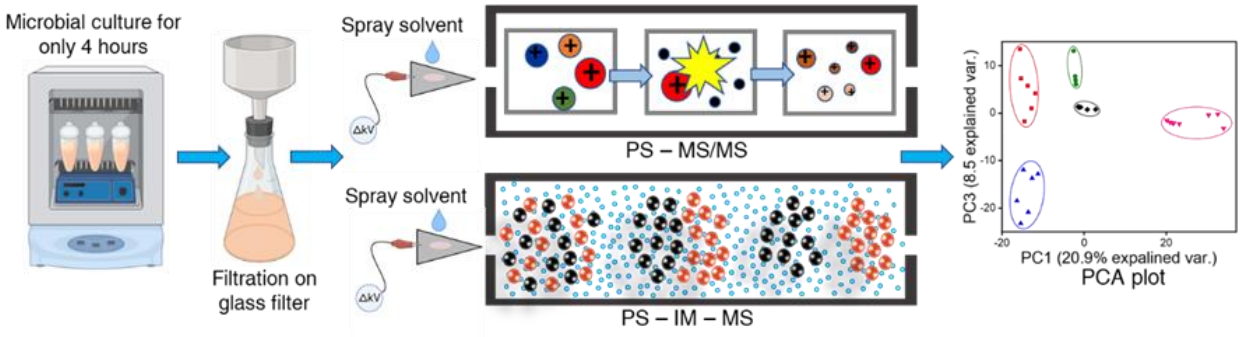

Figure 4.2. Schematic workflow for rapid detection and discrimination of bacteria using high-resolution paper spray ion mobility tandem mass spectrometry (PS-IM-MS/MS).

4.2.5. High-resolution Ion Mobility Mass Spectrometry

The tandem MS/MS spectra and the ion mobility spectra were acquired and recorded as two separate experiments. Each experiment was replicated 6-8 times where a freshly cut-glass fiber for each replicate was used. The spectra were acquired in both positive and negative ion modes. The tandem mass spectra were analyzed using MassHunter qualitative analysis software, while the overlapping spectra of the IM data files were demultiplexed using the PNNL PreProcessor software package, version 4.0 (2021.10.27), developed at Pacific Northwest National Lab (PNNL, omics.pnl.gov) [141]. Resolving power (Rp) of the Agilent 6560 operating either in the "single pulse" or "multiplexed" mode is ~60. The IM data obtained in the multiplexed mode after deconvolution through PNNL software were further processed via the "high resolution demultiplexing (HRdm)" tool for enhancement of the resolving power to ~250 [93]. In this study, we utilized a beta version of the HRdm software (v2.0.116) for enhancing the IMS separation of isobars/isomers [95]. HRdm is a new post-acquisition data reconstruction technique utilizing a Hadamard transform to enhance the IMS separation of isobars/isomers. CCS measurements of abundant biomarkers were performed using the single-field (calibrant-dependent) method with a drift field of 18.5 V/cm [85]. The tandem mass spectra and the high-resolution IM data were exported from qualitative analysis and IM software, respectively for multivariate analysis.

4.2.6. Multivariate Statistics

As shown in Figure 4.2, we used the spectra obtained from PS-IM-MS and PS-MS/MS experiments for our multivariate statistical analysis. The data from each replicate was normalized through linear scaling in both positive and negative ion modes. To examine the impact of including the IM spectra into the PS-MS/MS data on the discrimination of *Bacillus* species, we generated

two different data matrices, with and without ion mobility information. These datasets are listed in Table 4.2. Ions in *m/z* 100 - 1400 and 0 - 60 ms ranges were considered. Firstly, to reduce the redundant information, drift time selection was conducted by generating the dataset with identification of peaks for each species. Then, the dataset was reconstructed based on the selected drift time within mass spectra information. Therefore, each value in the dataset denotes the intensity of bacteria with specific drift spectra and mass spectra.

Table 4.2. List of bacteria investigated with PS-IM-MS and PS-MS/MS in positive and negative ion modes.

Bacteria species	PS-MS/MS		PS-IM-MS	
	Positive	Negative	Positive	Negative
Bacillus altitudinis	8	7	8	6
Bacillus pumilus	8	8	8	7
Bacillus subtilis	8	7	8	6
Bacillus thuringiensis	7	8	7	8
Bacillus velezensis	8	8	8	8

PCA is one of the commonly used approaches to drastically reduce the dimensionality of the dataset while keeping as much information as possible, especially for datasets with complex information, e.g., the data that includes multidimensional separations like those obtained herein [142]. Therefore, we applied PCA on the datasets listed in Table 4.2. After applying PCA, original data matrices were reorganized and compressed into a set of independent principal components (PCs). Each PC was generated by a linear combination of variables from the original dataset and the loading coefficient of PCs provided the importance of each original variable. The similarities among the five *Bacillus* species were visualized by biplots for PCs, which are two-dimensional

scatter plots. Besides, based on the proportion of variance explained by each PC, the first five PCs were selected as new variables for the subsequent analysis.

Table 4.3. Confusion matrices for negative ion mode studies **(A)** without ion mobility data (PS-MS/MS data only). **(B)** with ion mobility data included (PS-IM-MS and PS-MS/MS data).

(A)

Negative ion mode without ion mobility (Total 38 samples)					
Actual / Predicted	B. altitudinis	B. pumilus	B. subtilis	B. thuringiensis	B. velezensis
B. altitudinis	7	0	0	0	0
B. pumilus	0	8	0	0	0
B. subtilis	0	0	5	0	0
B. thuringiensis	0	0	2	8	1
B. velezensis,	0	0	0	0	7

(B)

Negative ion mode with ion mobility (Total 35 samples)					
Actual / Predicted	B. altitudinis	B. pumilus	B. subtilis	B. thuringiensis	B. velezensis
B. altitudinis	6	0	0	0	0
B. pumilus	0	7	0	0	0
B. subtilis	0	0	6	0	0
B. thuringiensis	0	0	0	8	0
B. velezensis,	0	0	0	0	8

Next, LDA, which is a statistical method to classify two or more classes of objects, was applied to discriminate different species using the new variables generated by PCA [143]. LDA attempts to model the difference between classes (i.e., species in the present study) through generating the linear combinations of variables that separate two or more classes of objects, and

the resulting combination is the so-called linear classifier. The classifier divides the data space into several disjoint regions where each class belongs to. Given a new sample, the classifier predicts its class according to the regions it locates. Each given sample is identified by the classifier and allocated to the corresponding class if it is in a certain region.

To avoid overfitting problem, we applied stratified cross-validation (CV) which is a commonly used resampling technique to evaluate models [144]. In this study, a replicate was randomly selected from each species to generate the testing set (around 13% of the dataset), and the rest formed the training set (around 87% of the dataset). The training set was used to train the linear classifier, which was then applied to the testing set to obtain the prediction accuracy. To avoid sampling bias, CV was repeated 400 times, and the classification accuracies were averaged over all the CVs. The model performances are reported in confusion matrices (Table 4.3 and Table 4.4). The significance of including IM data into the PS-MS/MS workflow was intuitively reflected by comparing the classification performance of different datasets with PS-MS/MS and PS-IM-MS/MS data.

Table 4.4. Confusion matrices for positive ion mode studies **(A)** without ion mobility data (PS-MS/MS data only). **(B)** with ion mobility data included (PS-IM-MS and PS-MS/MS data).

(A)

Positive ion mode without ion mobility (Total 39 samples)					
Actual / Predicted	B. altitudinis	B. pumilus	B. subtilis	B. thuringiensis	B. velezensis
B. altitudinis	8	1	0	0	0
B. pumilus	0	7	0	0	0
B. subtilis	0	0	8	0	0
B. thuringiensis	0	0	0	7	0
B. velezensis,	0	0	0	0	8

(B)

Positive ion mode with ion mobility (Total 39 samples)					
Actual / Predicted	B. altitudinis	B. pumilus	B. subtilis	B. thuringiensis	B. velezensis
B. altitudinis	8	0	0	0	0
B. pumilus	0	8	0	0	0
B. subtilis	0	0	8	0	0
B. thuringiensis	0	0	0	7	0
B. velezensis,	0	0	0	0	8

4.3. Results and Discussion

4.3.1. Optimization of the spray solvent and incubation time for early bacteria detection

B. subtilis and *B. thuringiensis* were used as model organisms for the optimization of the needed culturing time. We monitored the abundance of the phospholipids and surfactins detected in the ranges: *m/z* 600 to 800 and *m/z* 900 to 1200, respectively. We compared the mass spectra obtained from PS-MS analysis of bacteria cultured for 4, 8, 12, and 16 hours. As depicted in Figure

4.3 and Figure 4.4, the same ions (i.e. fatty acids, phospholipids and surfactins) were detected irrespective of the culturing time. The progression of the culture through its growth cycle may be responsible for the observed spectral variation in the relative intensities of surfactins and phospholipids, while the overall qualitative differences in the MS spectra may be due to the ionization phenomenon and bacterial metabolism at the time of sampling [145, 146]. Previous studies have reported that MS spectral variability due to culture time does not affect bacterial identification by mass spectrometry [137, 146, 147]. Therefore, due to the clinical importance of early detection, we chose an incubation time of 4 hours for further experiments.

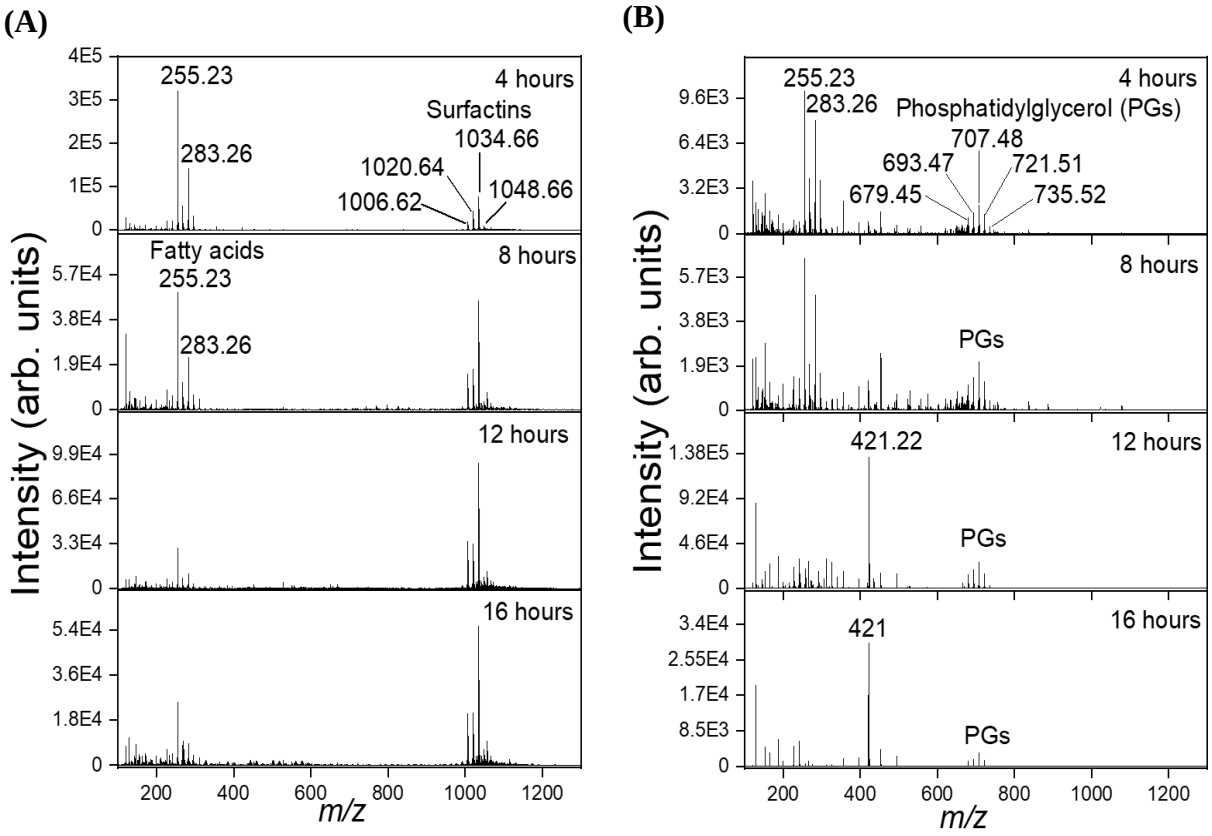

Figure 4.3. Optimization of the needed incubation time for early detection of bacteria in the negative ion mode using B. subtilis **(A)** and B. thuringiensis **(B)** as model organisms.

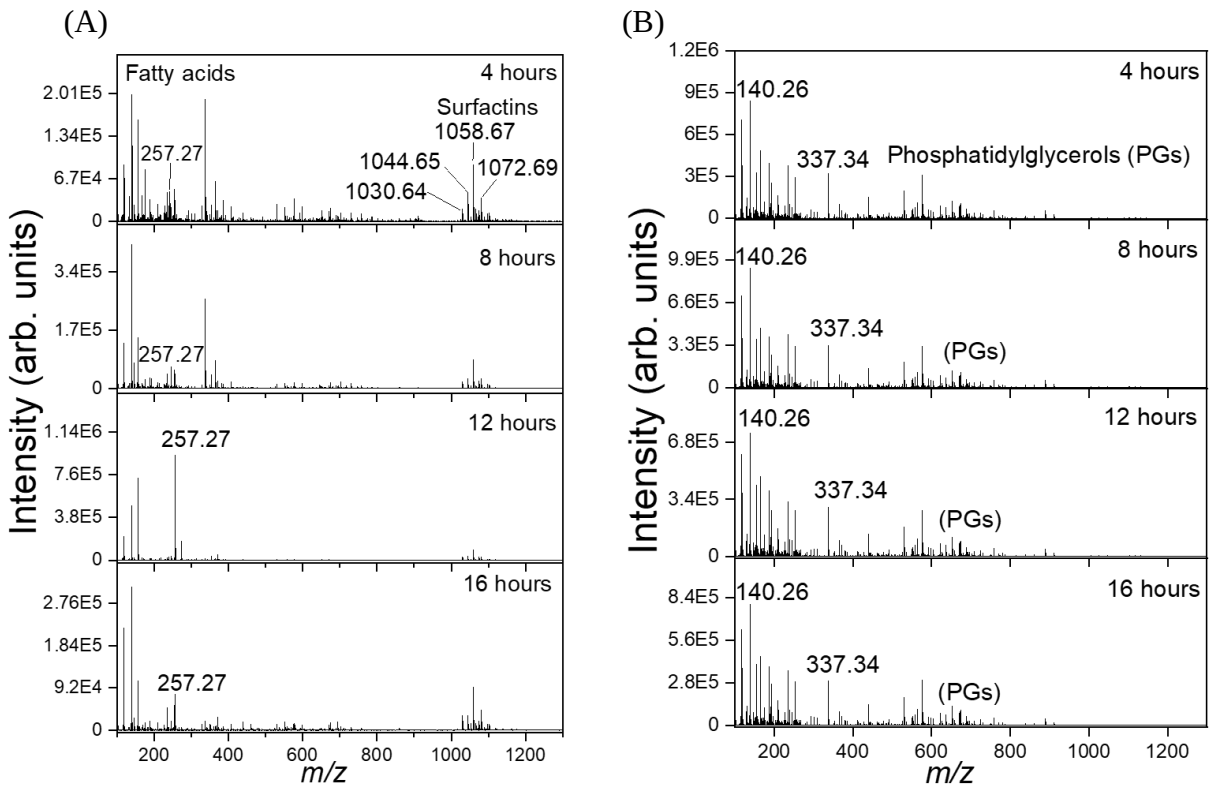

Figure 4.4. Optimization of incubation time for early detection of bacteria in the positive ion mode using *B. subtilis* **(A)** and *B. thuringiensis* **(B)** as model organisms.

In paper spray, the spray solvent impacts the extraction efficiency of the analytes of interest from the surface of the paper substrate and the spray efficiency at the tip of the paper. We examined two different spray solvents, isopropyl alcohol (IPA) and methanol (MeOH). Higher ion signals were obtained for the surfactins and phospholipids in both ion modes upon using IPA as a spray solvent than with MeOH (Figure 4.5). The high peak intensities observed with IPA can be attributed to its relatively low volatility and characteristic lower surface tension (20.52 mN/m) compared to that of MeOH (21.82 mN/m) [148, 149]. Solvents with low surface tension values facilitate the formation of the electrospray microdroplets from the paper tip [148]. Furthermore, the low volatility of IPA led to a stable spray throughout the electrospray period (2 minutes). Of note, there was a signal enhancement with the addition of 0.05% CHAPS (surfactant) to MeOH in

the negative ion mode (Figure 4.5A) which was attributed to the capability of surfactants in reducing spray solvents' surface tension, thereby increasing their ionization efficiency [53, 150]. However, the surfactant (CHAPS) has a negative impact on the positive mode spectra (Figure 4.5B) which can be attributed to charge competition as evidenced by previous studies [53].

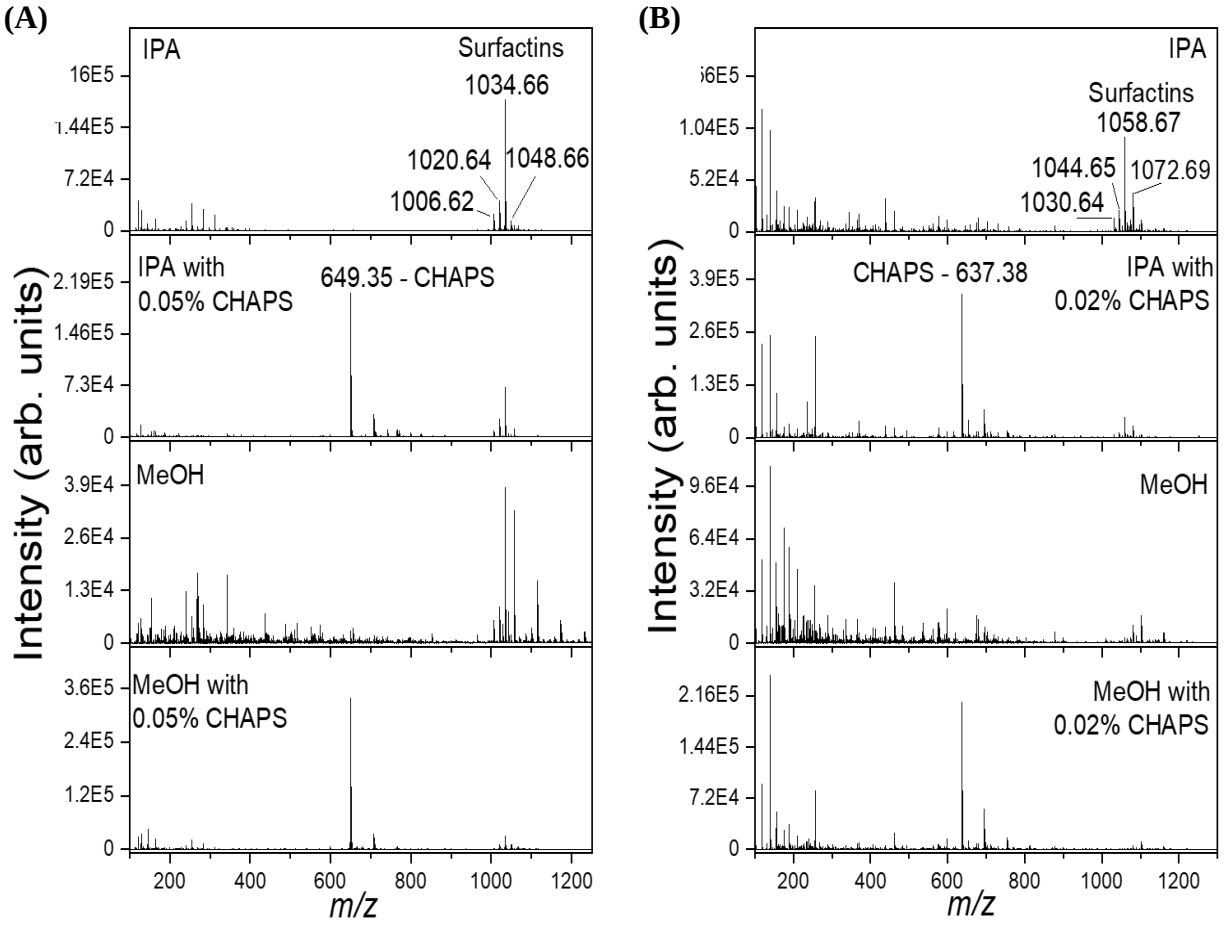

Figure 4.5. Optimization of spray solvents to be used in PS-IM-MS experiments for high MS spectral peak intensities. The biomarkers were monitored for the optimization process in **(A)** Negative and **(B)** positive ion modes.

In addition, we compared the mass spectra obtained by spraying pure spray solvent, pure LB growth medium, and *B. subtilis* (Figure 4.6). As shown in Figure 4.6, the major biomarkers were absent from the background spectra. Moreover, Figure 4.7 shows a comparison of the absorbance of bacteria in water, MeOH, and IPA with a control solution. It illustrates the higher

capability of IPA in lysing bacterial cell membranes than MeOH or water which would lead to higher signal intensities of phospholipids and surfactins upon using IPA as a spray solvent. We, therefore, selected the incubation time of 4 hours and IPA as the spray solvent for rapid detection and discrimination of bacterial species.

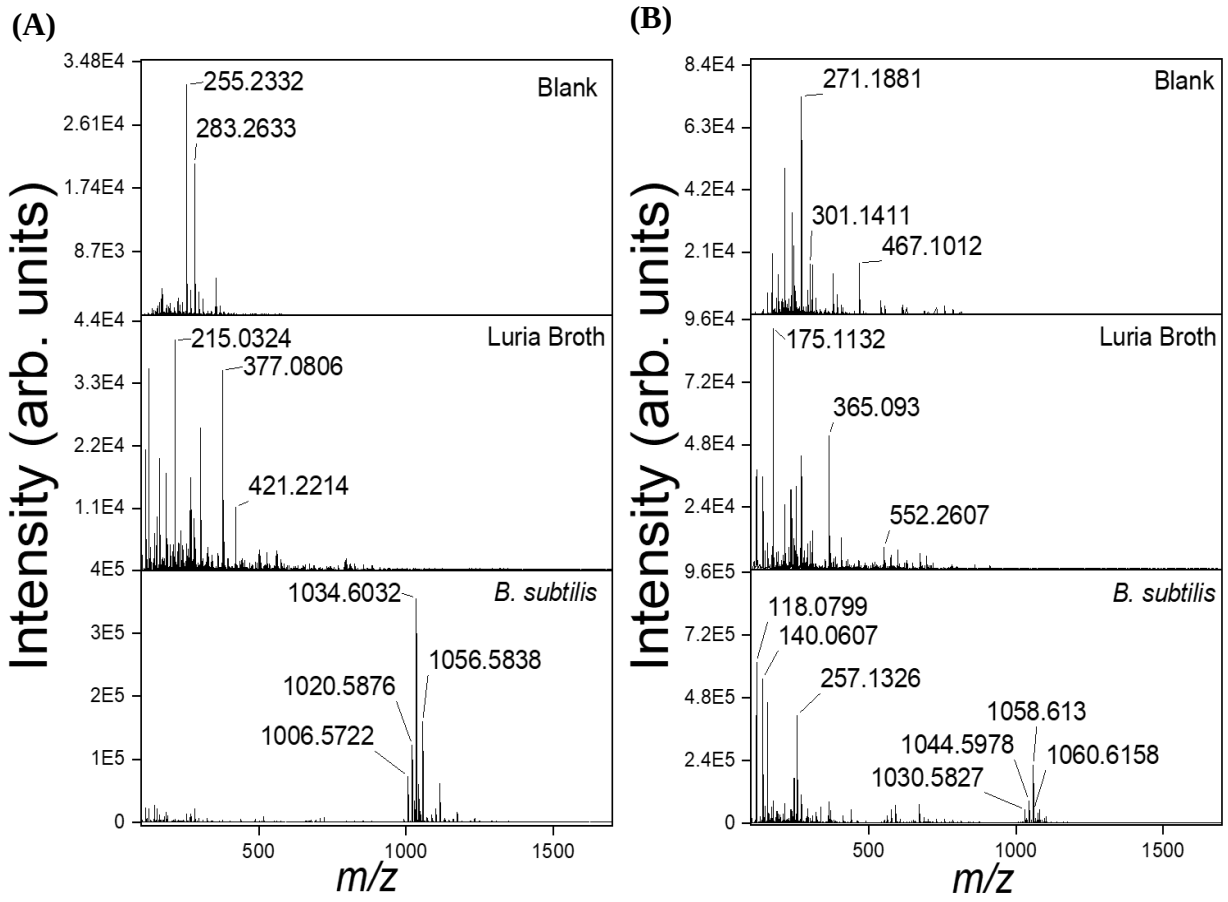

Figure 4.6. Comparison of signal intensities of ions from Blank, Luria broth, and *B. subtilis*. **(A)** Negative and **(B)** positive ion modes.

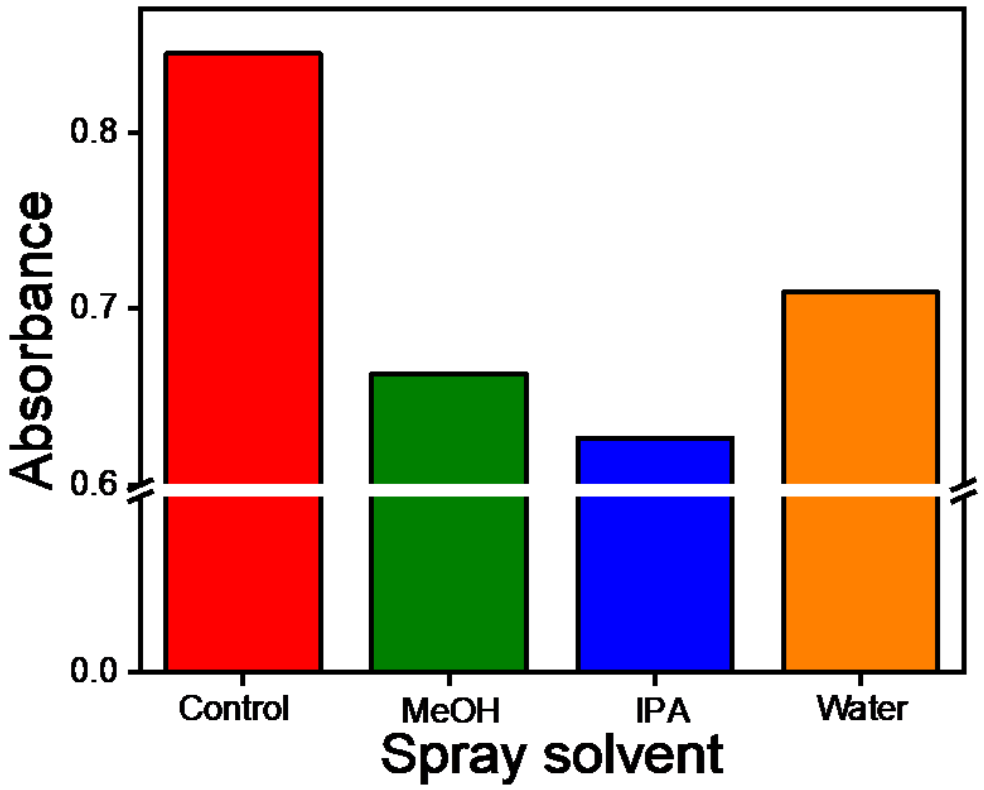

Figure 4.7. Comparison of the lysis ability of methanol, isopropyl alcohol, and water by absorbance measurements at 600 nm. In this experiment, a decrease in absorbance occurred for two reasons (1) dilution; 700 µL of the bacteria were diluted with 300 µL of the spray solvents (2) the degree of lysis. Since the samples were all diluted to the same degree, a greater decrease in absorbance indicates a stronger capability of the spray solvent in achieving lysis of the bacteria

4.3.2. Bacteria discrimination by Mass Spectrometry

Bacillus species are known producers of cyclic lipoheptapeptide surfactins which are known for their antimicrobial, antifungal, and antiviral effects [151]. In addition, their cell membranes contain other lipids such as fatty acids (FAs), phosphatidylglycerols (PGs), and phosphatidylethanolamines (PEs) [43]. To correctly identify the detected ions, we used exact mass measurements, CCS values, and MS/MS spectra. The *m/z* and CCS values of the highly abundant ions are listed in Table 4.5.

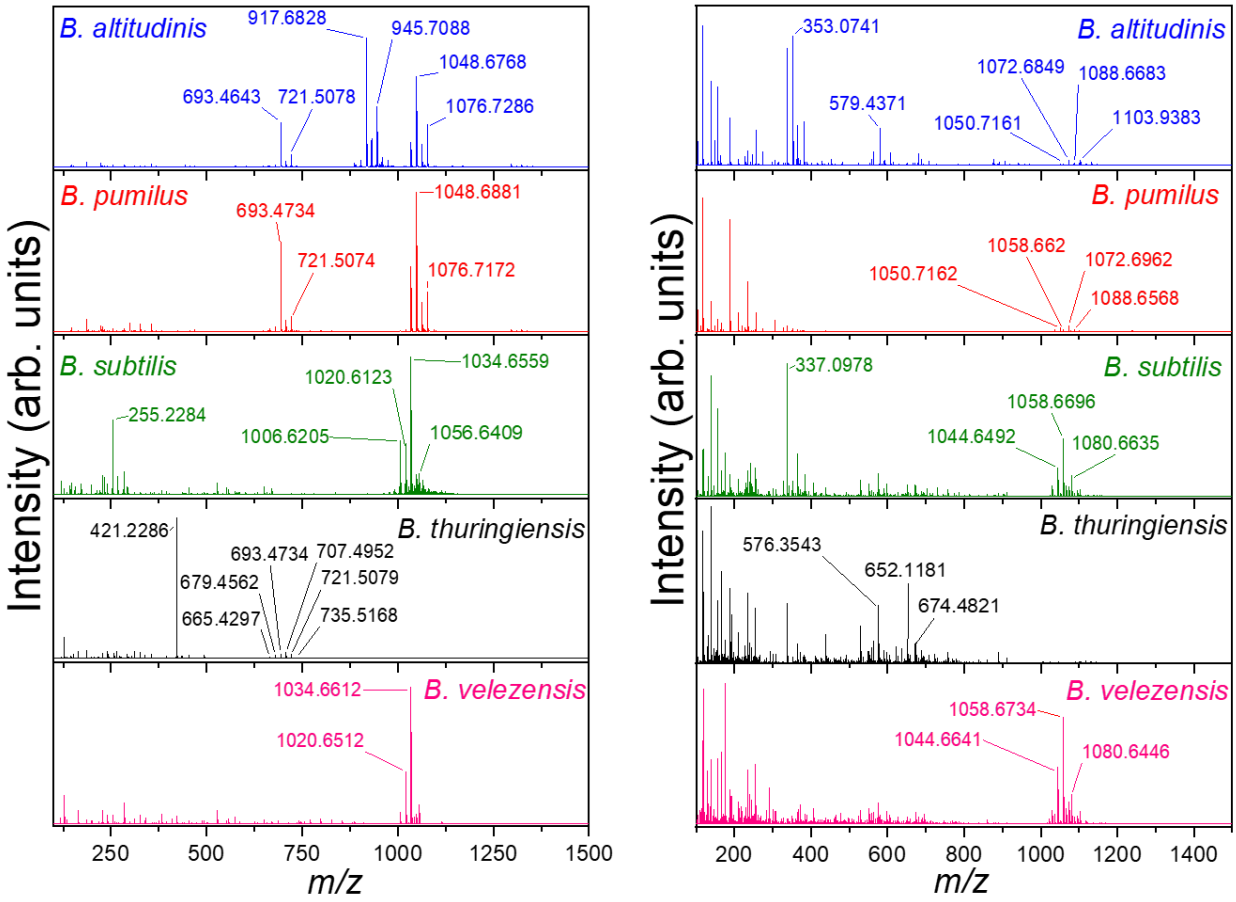

Figure 4.8. Mass spectra of the 5 *Bacillus* species: *B. altitudinis*, *B. pumilus*, *B. subtilis*, *B. thuringiensis*, and *B. velezensis* recorded after 4 hours of incubation time acquired in the **(A)** negative and **(B)** positive ion modes.

Visual inspection of the mass spectra shows some differences between the 5 *Bacillus* species. As shown in the negative mode (Figure 4.8A), *B. altitudinis* and *B. pumilus* produced similar phospholipids and surfactins except for triacylglycerols (TGs) observed at *m/z* 903.66, 917.68, 931.69, 945.71, 959.72, and 973.74 which were unique to *B. altitudinis*. Moreover, *B. subtilis* and *B. velezensis* gave similar mass spectral profiles dominated by surfactins-C12 through C17 while *B. thuringiensis* mass spectra were mainly dominated by PGs. From exact mass measurements and previous reports, the PG ions at *m/z* 665.44, 679.45, 693.47, 707.48, 721.51, and 735.52 were assigned to be $[PG\ (28:0)-H]^-$, $[PG\ (29:0)-H]^-$, $[PG\ (30:0)-H]^-$, $[PG\ (31:0)-H]^-$,

Table 4.5. The various adducts, mass accuracy, and the collision cross section (CCS) values of the different isomers of lipids and surfactins observed in all the 5 Bacillus species. The CCS values were obtained with single field measurements at a drift field of 18.5 V/cm. Lipid CCS values were compared with the Lipid CCS predictor, and the percentage difference was less than 1%.

Negative ion mode									
Phospholipids									
	Formula	Isomers	Adducts	Theoretical *m/z*	Experimental *m/z*	*m/z* error (ppm)	Exp. CCS (Å^2)	Lipid CCS* (Å^2)	% Diff.
PG 28:0	$C_{34}H_{67}O_{10}P$	(12:0/16:0)	$[M-H]^-$	665.4399	665.4388	1.65	252.5	252.0	0.20
PG 29:0	$C_{35}H_{69}O_{10}P$	(14:0/15:0)	$[M-H]^-$	679.4556	679.4551	0.74	253.3	254.5	-0.47
		(13:0/16:0)	$[M-H]^-$				254.6	254.9	-0.12
PG 30:0	$C_{36}H_{71}O_{10}P$	(15:0/15:0)	$[M-H]^-$	693.4712	693.4705	1.01	257.8	257.8	0.00
		(14:0/16:0)	$[M-H]^-$				258.3	258.2	0.04
		(13:0/17:0)	$[M-H]^-$				259.5	258.5	0.39
PG 31:0	$C_{37}H_{73}O_{10}P$	(15:0/16:0)	$[M-H]^-$	707.4869	707.4848	2.97	261.1	260.9	0.08
		(14:0/17:0)	$[M-H]^-$				262.8	261.3	0.57
PG 32:0	$C_{38}H_{75}O_{10}P$	(16:0/16:0)	$[M-H]^-$	721.5025	721.5008	2.36	262.2	264.2	-0.76
		(15:0/17:0)	$[M-H]^-$				263.3	264.6	-0.49
		(14:0/18:0)	$[M-H]^-$				264.8	264.9	-0.04
PG 33:0	$C_{39}H_{77}O_{10}P$	(16:0/17:0)	$[M-H]^-$	735.5182	735.5169	1.77	267.5	267.2	0.11
		(15:0/18:0)	$[M-H]^-$				268.4	267.6	0.30
Surfactins									
	Formular	Isomers	Adducts	Theoretical *m/z*	Experimental *m/z*	*m/z* error (ppm)	Experimental CCS (Å^2)		
(C17)	$C_{55}H_{97}N_7O_{13}$	Iso 1	$[M-H]^-$	1062.7072	1062.7053	1.79	325.0		
(C16)	$C_{54}H_{95}N_7O_{13}$	Iso 1	$[M-H]^-$	1048.6915	1048.6905	0.95	323.8		
		Iso 2	$[M-H]^-$				321.2		
(C15)	$C_{53}H_{93}N_7O_{13}$	Iso 1	$[M-H]^-$	1034.6759	1034.6744	1.45	320.7		
		Iso 2	$[M-H]^-$				318.9		
			$[M-2H+Na]$	1056.6578	1056.6549	-2.74	321.6		
(C14)	$C_{52}H_{91}N_7O_{13}$	Iso1	$[M-H]^-$	1020.6602	1020.6568	3.33	317.2		
		Iso 2	$[M-H]^-$				315.8		
			$[M-2H+Na]$	1042.6421	1042.6446	2.39	319.0		
(C13)	$C_{51}H_{89}N_7O_{13}$	Iso 1	$[M-H]^-$	1006.6446	1006.6437	0.89	314.1		
		Iso 2	$[M-H]^-$				312.3		
			$[M-2H+Na]$	1028.6265	1028.6261	-0.38	315.9		
(C12)	$C_{50}H_{87}N_7O_{13}$	Iso 1	$[M-H]^-$	992.6289	992.6283	0.60	311.1		
		Iso 2	$[M-H]^-$				309.7		
Positive ion mode									
Surfactins									
	Formular	Isomers	Adducts	Theoretical *m/z*	Experimental *m/z*	*m/z* error (ppm)	Exp. CCS (Å^2)	CCS compendium** (Å^2)	
(C17)	$C_{55}H_{97}N_7O_{13}$	Iso2	$[M+H]^+$	1064.7217	1064.723	-1.22	340.5	×	
		Iso 1	$[M+H]^+$				337.8	×	
		Iso2	$[M+Na]^+$	1086.7037	1086.6995	3.86	340.9	×	
		Iso 1	$[M+Na]^+$				337.3	×	
		Iso2	$[M+K]^+$	1102.6776	1102.6742	3.08	342.9	×	
		Iso 1	$[M+K]^+$				340.2	×	
(C16)	$C_{54}H_{95}N_7O_{13}$	Iso 3	$[M+H]^+$	1050.7061	1050.7078	-1.62	339.3	336.2	

		Iso2	$[M+H]^+$				338.4	
		Iso 1	$[M+H]^+$				336.9	
		Iso 3	$[M+Na]^+$	1072.688	1072.6848	2.98	339.4	
		Iso2	$[M+Na]^+$				337.4	338.0
		Iso 1	$[M+Na]^+$				335.8	
		Iso2	$[M+K]^+$	1088.6619	1088.6628	-0.82	340.7	×
		Iso 1	$[M+K]^+$				337.6	
(C15)	$C_{53}H_{93}N_7O_{13}$	Iso 3	$[M+H]^+$	1036.6904	1036.6898	0.58	336.8	
		Iso2	$[M+H]^+$				334.2	333.5
		Iso 1	$[M+H]^+$				331.9	
		Iso 3	$[M+Na]^+$	1058.6724	1058.6693	2.93	336.2	
		Iso2	$[M+Na]^+$				334.3	334.7
		Iso 1	$[M+Na]^+$				332.5	
		Iso2	$[M+K]^+$	1074.6463	1074.6446	1.5819	335.9	336.7
		Iso 1	$[M+K]^+$				333.7	328.0
(C14)	$C_{52}H_{91}N_7O_{13}$	Iso2	$[M+H]^+$	1022.6748	1022.6726	2.15	329.4	330.6
		Iso 1	$[M+H]^+$				328.3	
		Iso 3	$[M+Na]^+$	1044.6567	1044.6537	2.87	331.0	
		Iso2	$[M+Na]^+$				328.9	332
		Iso 1	$[M+Na]^+$				326.8	
		Iso2	$[M+K]^+$	1060.6306	1060.6312	-0.566	332.8	×
		Iso 1	$[M+K]^+$				329.1	
(C13)	$C_{51}H_{89}N_7O_{13}$		$[M+H]^+$	1008.6591	1008.6577	1.39	-	327.1
		Iso2	$[M+Na]^+$	1030.6411	1030.6413	-0.19	328.7	329.8
		Iso 1	$[M+Na]^+$				325.9	
			$[M+K]^+$	1046.615	1046.6155	-0.478	-	332.1
(C12)	$C_{50}H_{87}N_7O_{13}$		$[M+H]^+$	994.6435	994.6432	0.30	-	323.7
			$[M+Na]^+$	1016.6254	1016.6228	2.56	325.4	×
			$[M+K]^+$	1032.5993	1032.5984	0.8716	-	×

* CCS values from Lipid CCS predictor

** CCS values from CCS compendium

- No CCS values due to their low peak intensities

× No CCS values from CCS compendium

[PG (32:0)-H]$^-$, and [PG (33:0)-H]$^-$ [151]. The PG lipids were found across the 5 *Bacillus* species but in different intensities, while the surfactins were found in all the 5 *Bacillus* species except *B. thuringiensis*. The mass spectra recorded in the positive ion mode were rich in information with 3 main adducts, protonated, sodium, and potassium adducts. As shown in (Figure 4.8B), the mass spectra of the 5 *Bacillus* species were predominated by surfactins except for *B. thuringiensis* in the positive ion mode. The detected ions present three homologue sets with different carbon chain lengths, i.e., they differ in a repeating chemical unit with a characteristic difference in mass of 14 which is attributed to the molecular weight of a CH_2 group. The first group $[M+H]^+$ contained *m/z*

1022.67, 1036.69, 1050.70 while the second group $[M+Na]^+$ contained *m/z* 1044.65, 1058.67, and 1072.69, and the third group $[M+K]^+$ included *m/z* 1074.65 and 1088.66 (Table 4.5).

4.3.3. Species-level discrimination of *Bacillus* species by Ion Mobility Spectrometry

Results from previous studies have shown poor separation and overlap between bacteria at the species level when discrimination was solely based on mass spectra [57, 139, 152]. This can be attributed to the limitation of mass spectrometry in differentiating biomarkers with identical chemical formulas or the same *m/z*. The limited specificity of mass spectrometry can be enhanced by coupling it to ion mobility spectrometry which enables isomer separation through collisions with inert buffer gas under an electric field [86]. Phospholipids found in *Bacillus* cell membranes can exist as different isomers, such as acyl-chain isomers, positional isomers (e.g., sn- and double bond positional isomers), and stereoisomers (e.g., *cis*/*trans* isomers) [64, 153]. As shown in Figure 4.8A, *m/z* 721. 51 (PG (32:0)) was detected in high abundance in the mass spectra profiles of *B. altitudinis*, *B. pumilus*, and *B. thuringiensis* while its intensity was low in *B. subtilis* and *B. velezensis*. Careful investigation of the drift time spectra of the 5 *Bacillus* species obtained from our PS-IM-MS studies revealed different isomeric forms of PG 32:0. The number of the resolved IM peaks (Figure 4.9A) observed for the PG 32:0 across the 5 species was 3 for *B. thuringiensis*, 2 for *B. subtilis* and *B. velezensis*, and 1 for *B. altitudinis* and *B. pumilus*. CCS values obtained through IM measurements have been previously used to improve identification confidence, reduce false-positive identification, and identify co-eluting metabolites that have similar MS/MS spectra. Therefore, we measured the CCS values of the detected lipid biomarkers and compared them to those obtained from the widely available lipid CCS database (Lipid CCS predictor) [154]. Using single-field measurement, we estimated the IM peaks at 33.25 ms, 33.56 ms, and 33.99 ms to have

CCS values of 262.2 Å^2, 263.3 Å^2, and 264.8 Å^2 respectively. We confirmed their identities as PG (16:0/16:0), PG (15:0/17:0), and PG (14:0/18:0), respectively by comparing the measured and predicted CCS values. The percentage difference between the measured and predicted values was less than 0.8% (Table 4.5). These results indicate that PG (15:0/17:0) was present in all the *Bacillus* species, the PG (16:0/16:0) was present in 3 of the 5 *Bacillus* species; *B. thuringiensis*, *B. subtilis*, and *B. velezensis*, while PG (14:0/18:0) was unique to *B. thuringiensis*.

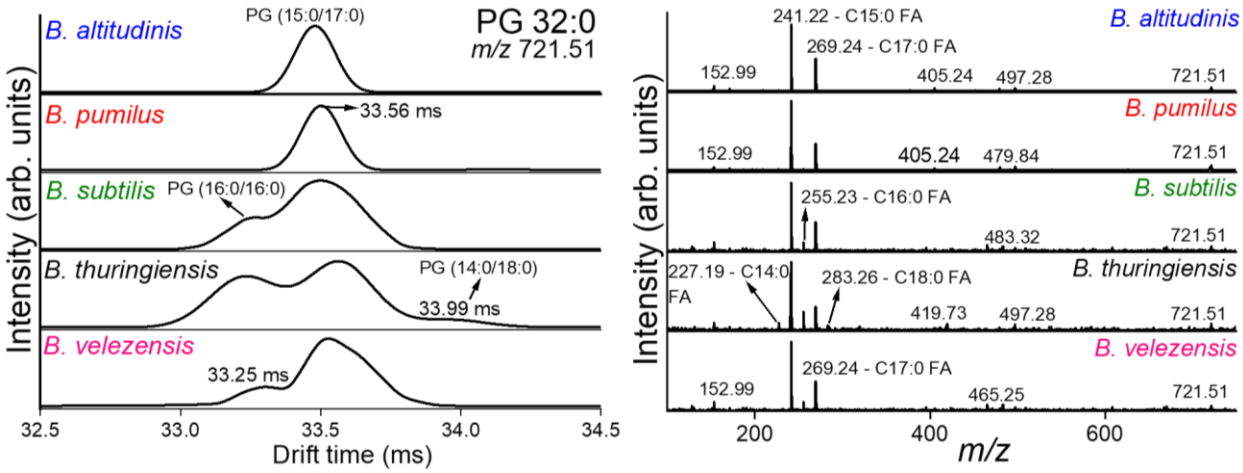

Figure 4.9. PS-IM-MS and PS-MS/MS spectra obtained in the negative ion mode of the 5 Bacillus species where **(A)** Ion mobility spectra revealed the presence of various lipid isomers of m/z 721.51 (PG (32:0)) and **(B)** Tandem mass spectra (MS/MS) spectra of m/z 721.51 which support the identification of the lipid isomers by the IM spectra.

In addition, we used tandem mass spectrometry measurements to further confirm the identities of phospholipids using fragmentation patterns. The fragmentation mechanisms of PGs have been extensively described previously, with the loss of two fatty acyl side chains ([$RCH_2CO_{2\ sn\text{-}1}$]$^-$ and [$RCH_2CO_{2\ sn\text{-}2}$]$^-$) dominating the product ion spectra [65]. Careful investigation of the tandem mass spectra revealed characteristic fragment ions of the PG 32:0 distinctively present in

each species (Figure 4.9B). For instance, the CID spectrum of *m/z* 721.51 (PG 32:0) in *B. thuringiensis* shows abundant product ions at *m/z* 227, 241, 255, 269, and 283, respectively; they correspond to the carboxylate anions of C14:0, C15:0, C16:0, C17:0, and C18:0 fatty acids. Hence, the product ions spectra of the *B. thuringiensis* confirm the presence of the 3 acyl chain isomers identified by the IM separations and CCS measurements. Similarly, the CID spectrum of *m/z* 721.51 in *B. altitudinis* and *B. pumilus* confirmed the presence of PG (15:0/17:0) isomer as accurately identified by IM. In addition, the MS/MS spectrum of *m/z* 721.51 in *B. subtilis*, and *B. velezensis* confirmed the presence of PG (15:0/17:0) and PG (16:0/16:0) isomers as accurately identified by IM.

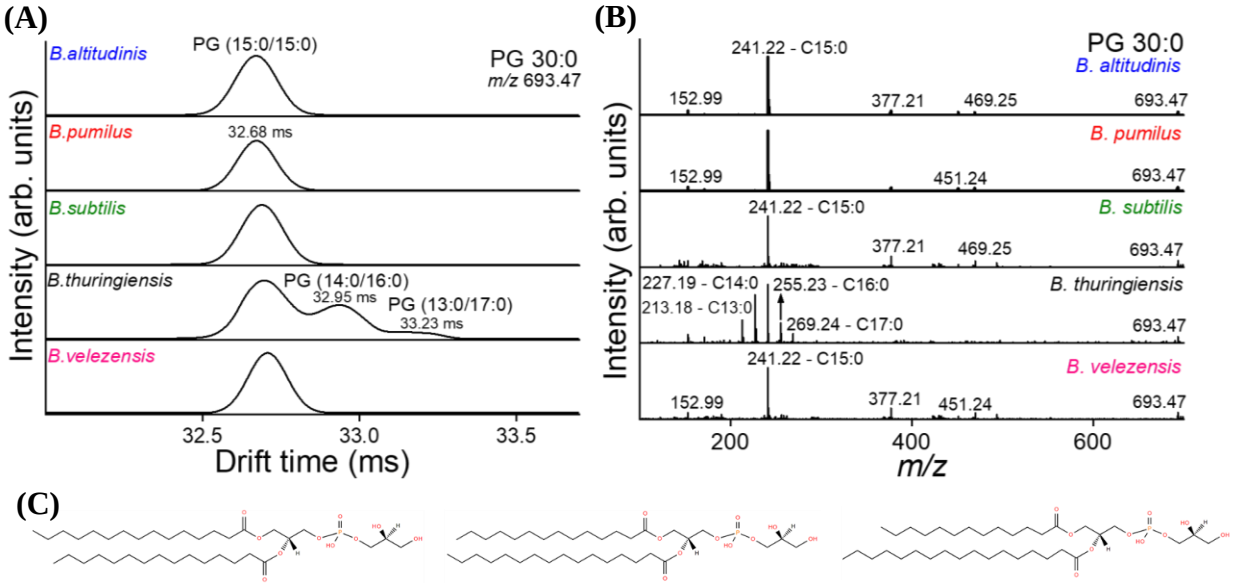

Figure 4.10. PS-IM-MS and PS-MS/MS spectra obtained in the negative ion mode of the 5 *Bacillus* species where **(A)** Ion mobility spectra revealed the various lipid isomers of *m/z* 693.47 (PG (30:0)) and **(B)** Tandem mass spectra (MS/MS) spectra support the identification of the lipid isomers by the IM spectra. **(C)** Structure of the acyl chain lipid isomers.

Another example of discriminating lipid isomers between the bacteria species is *m/z* 693.47 (PG (30:0)) which was present in all the 5 *Bacillus* species as PG (15:0/15:0), while in *B.*

thuringiensis it was present as PG (14:0/16:0) and PG (13:0/17:0) in addition to PG (15:0/15:0), as was confirmed by the MS/MS spectra shown in Figure 4.10. Of note, MS/MS spectra wouldn't be able to resolve geometric isomers which will increase the importance of performing IM measurements in identifying the structures of key biomarkers [86].

The bacterial cyclic lipopeptides (surfactins) present in *Bacillus* species are β-hydroxyl cyclic heptapeptides with possibilities of leucine (Leu), isoleucine (Ile), or valine (Val) amino acids present at positions 2, 4, and 7 while positions 1, 3, 5, and 6 are fixed [155]. In addition to the changes in the peptide chain, another source of surfactins' structural diversity can be introduced by their lipid chain configurations; their lipid chains can have a linear configuration and be branched, with iso and anteiso configurations [156]. The peptide diversity with different configurations of the lipid chains results in numerous variants or isoforms of the surfactins. We examined the IM spectra of *m/z* 1050.71 $[C_{54}H_{95}N_7O_{13}+H]^+$ which was found to be common to *B. altitudinis* and *B. pumilus* (Figure 4.11A). We found a different number of surfactin isoforms discriminating the two species. For instance, the IM peaks at 41.92 ms and 42.32 ms were common to both species while the IM peak observed at 42.70 ms was unique to *B. pumilus*. Using single field measurement, we estimated the CCS values of the IM peaks at 41.92 ms, 42.32 ms, and 42.70 ms to be 336.9 $Å^2$, 338.4 $Å^2$, and 339.3 $Å^2$, respectively. Of note, the experimental CCS values showed good agreement (less than 1% difference) when compared to empirical values from CCS compendium (Table 4.5) [157]. In addition, the IM peak at 43.13 ms in the drift spectra of *B. altitudinis* was considered to be an artifact because of the lack of the [M+1] and [M+2] monoisotopic peaks [95]. Similarly, we detected the presence of 2 surfactin isoforms in *m/z* 1044.65 (IM peaks at 41.19 ms and 41.48 ms) present in *B. velezensis* and *B. subtilis*, while the isoform at the IM peak of 41.95 ms was unique to *B. velezensis* (Figure 4.11C). Using MS/MS

measurements, we further characterized the surfactin isoforms identified by the IM studies. The CID spectrum of the *m/z* 1050.71 as shown in Figure 4.11B indicated two peptide sequences. The series of b+ ions at *m/z* 937→824→709→596→483→370 can be associated with β-OH FA-Glu^{1}-Leu/Ile^{2}-Leu/Ile^{3}-Leu/Ile^{4}-Asp^{5}-Leu/Ile^{6}-Leu/Ile^{7}, while the second series of b+ ions at *m/z* 937→824→709→610→497→384 can be associated with β-OH FA-Glu^{1}-Leu/Ile^{2}-Leu/Ile^{3}-Val^{4}-Asp^{5}-Leu/Ile^{6}-Leu/Ile^{7} (Figure 4.11D). The *m/z* 699 corresponds to the total mass of ion fragments containing$^{+}H_2$(Leu/Ile^{2}-Leu/Ile^{3}-Leu/Ile^{4}-Asp^{5}-Leu/Ile^{6}-Leu/Ile^{7}) OH, while the *m/z* 685

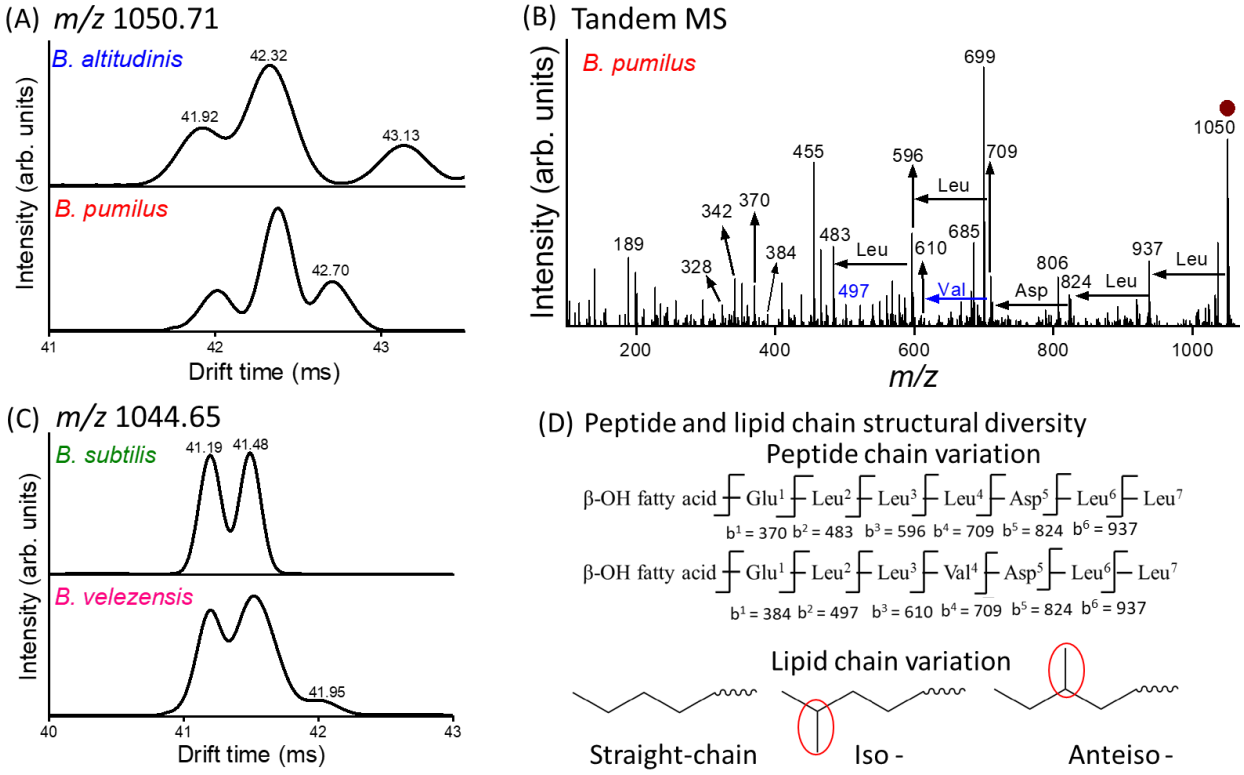

Figure 4.11. PS-IM-MS and PS-MS/MS spectra in the positive ion mode **(A)** IM spectra of surfactin ion at m/z 1050.71 showing different isomeric forms in B. altitudinis and B. pumilus. **(B)** MS/MS spectrum obtained by CID of m/z 1050.71. **(C)** IM spectra of surfactin ion at m/z 1044.65 showing different isomeric forms in B. subtilis and B. velezensis.**(D)** Structural variation in the peptide amino acid sequence and lipid chain configuration

corresponds to the total mass of ion fragments containing $^{+}H_2$(Leu/Ile^2-Leu/Ile^3-Val^4-Asp^5-Leu/Ile^6-Leu/Ile^7)OH. The presence of *m/z* 699 and 685 demonstrates the existence of two isoforms of the *m/z* 1050.71 which are C15-[Leu^4] and C16-[Sur] where the first discovered surfactin sequence (Glu-Leu-Leu-Val-Asp-Leu-Leu) was denoted as [Sur] and any changes in the peptide sequence were indicated with the abbreviation and position of the altered amino acid, i.e. in C15-[Leu^4], Val at position 4 is replaced by Leu [158].

Previous studies reported the loss of 42 and 28 from β-OH FA-Glu$^+$ to be associated with iso and anteiso configurations, respectively (Figure 4.11D) [155]. Meanwhile, anteiso can only be found in odd carbon chain lengths, iso can be found in odd and even- numbered carbon chain length [156]. The *m/z* 342 can be associated with loss of 42 from *m/z* 384 RGlu$^+$ of C16-[Sur] and 28 from *m/z* 370 RGlu$^+$ of C15-[Leu^4] which suggests two additional isomers: iso-C16-[Sur] and anteiso-C15-[Leu^4]. In addition, the *m/z* 328 can be associated with loss of 42 from *m/z* 370 RGlu+ of C15-[Leu^4] indicating the presence of iso-C15-[Leu^4]. Hence 5 isomers; C15-[Leu^4], iso-C15-[Leu^4], anteiso-C15-[Leu^4], C16-[Sur], and iso-C16-[Sur] can be potentially associated with *m/z* 1050.71. Of note, differentiating isomers based on their MS/MS spectra was challenging due to overlapping fragmentation patterns showing similar product ions such as *m/z* 937, 824, and 709 which were observed in the 5 potential isomers of surfactin at *m/z* 1050.71.

Similarly, 4 isomers; C14-[Sur], C15-[Val^7], anteiso-C15-[Val^7], and iso-C15-[Val^7] can be potentially associated with *m/z* 1044.65 as shown in the CID spectrum (Figure 4.12). It is evident that the ion mobility separation can effectively be utilized to identify discriminating isomers between bacteria species. However, the analytical complexity of the surfactin isoforms would require higher resolution to fully resolve the potential isomers.

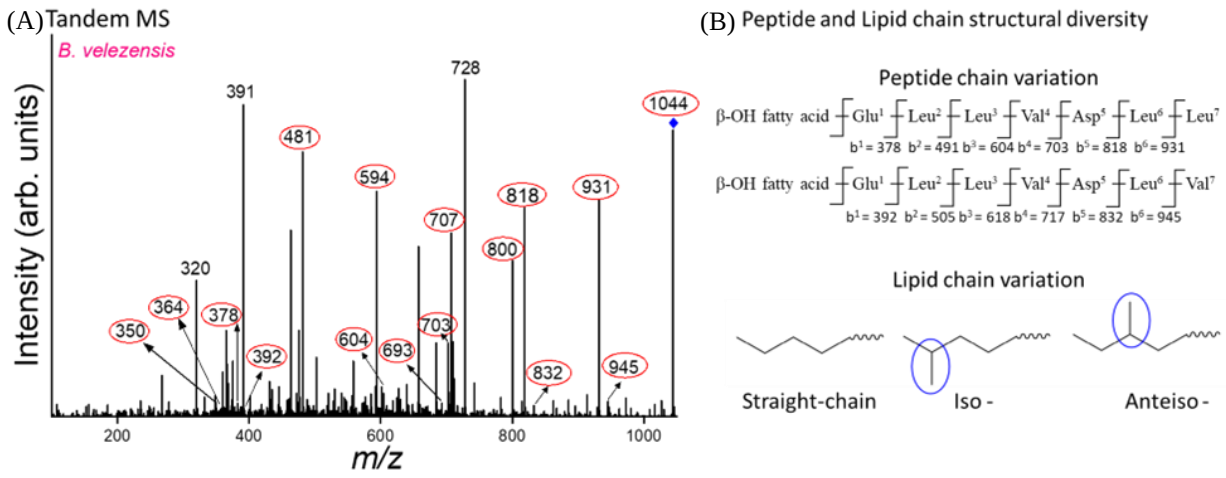

Figure 4.12. PS-IM-MS spectra in the positive ion mode of B. velezensis **(A)** MS/MS spectrum obtained by CID of m/z 1044.65. **(B)** Structural variation in the peptide amino acid sequence and lipid chain configuration.

4.3.4. Statistical Analysis

Multivariate statistical analysis was conducted to illustrate and quantitate the differences in the spectra obtained from PS-IM-MS and PS-MS/MS experiments of *Bacillus* spp. in negative and positive ion modes. The mass spectral profiles of the 5 *Bacillus* species were combined with LDA was performed to quantify the separation shown in the PCA score space. The prediction rates in the negative and positive ion modes were 92.4% and 97.6%, respectively. Upon including the IM separation data, the average prediction rates increased significantly in negative and positive ion modes to be 99.7% and 100.0%, respectively. The increased prediction rates can be attributed to the capability of IM to provide a clear separation between the diagnostic isomers based on their structures leading to an enhanced species' discrimination. Figure 4.13A and Figure 4.13B show that the *B. altitudinis* and *B. pumilus* are separated along the PC3 axis, indicating biochemical similarity between the two species. In the positive mode (Figure 4.13B), *B. subtilis* and *B. velezensis* were closer together than to *B. thuringiensis* due to the predominating effect of the

surfactins in the positive ion mode. Moreover, the CV confusion matrix reported in Table 4.3 and Table 4.4 show that *B. altitudinis* and *B. thuringiensis* was perfectly classified under both positive and negative ion modes, whereas *B. subtilis* had relatively lower classification rates in the negative ion mode when ion mobility information was excluded, i.e., utilizing the data obtained from PS-MS/MS only.

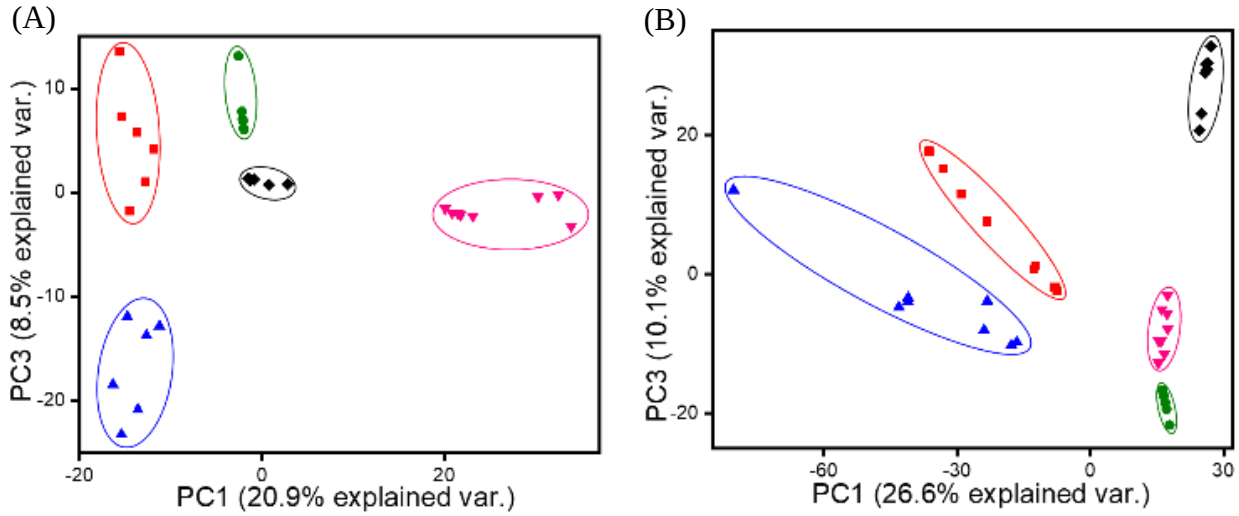

Figure 4.13. PCA plot of the 5 Bacillus species utilizing ion mobility, mass spectrometry, and tandem MS from PS-IM-MS and PS-MS/MS experiments in the **(A)** Negative and **(B)** Positive ion modes. Species are indicated by color and shape as follows: B. altitudinis (blue triangle pointing up), B. pumilus (red square), B. subtilis (green circle), B. thuringiensis (black diamond), B. velezensis (pink triangle pointing down).

4.4. Conclusions

This work demonstrates successful bacteria discrimination at the species level by high-resolution PS–IM–MS and PS–MS/MS analyses with only 4 hours incubation time and 2 minutes analysis time. Upon including the IM separation dimension data into the PS-MS/MS workflow, the prediction rates increased significantly in negative and positive ion mode from 92.4% and 97.6% to 99.7% and 100.0%, respectively. The increased prediction rates can be associated with

the capability of IM to provide a clear separation between the diagnostic isomers leading to an enhanced species' identification. Our results support a proof-of-concept for the application of PS-IM-MS in the rapid species-level discrimination of microorganisms. In addition, the high success rate of the species-level discrimination of the 5 *Bacillus* bacteria using high-resolution PS–IM–MS and PS–MS/MS data suggests the capability of the newly developed IM-based methods in strain-level differentiation.

Chapter 5. Strain-Level Discrimination of Bacteria by Liquid Chromatography and Paper Spray Ion Mobility Mass Spectrometry

5.1. Introduction

Each year in the United States, *E. coli* infections cause approximately 265,000 illnesses, 3,600 hospitalizations [159], and about 100 deaths [160]. Different *E. coli* strains share a close genetic identity but are associated with different diseases and antibiotic susceptibility profiles [161]. Therefore, effective treatments would depend on rapid and accurate identification of the causative strain, leading to strain-specific therapy that would shorten hospitalization periods, improve patient recovery, and lower antibiotic resistance. Bacterial dentification using MALDI-TOF MS is most reliable at the species level; however, it has a reduced discriminatory power at the strain level due to limiting factors such as (i) dependence on comparing the mass spectral profiles of the bacteria and the reference library [53, 162], (ii) reduced dynamic sensitivity, i.e., lowered detectability of protein signals over a wide concentration range [38, 163], and (iii) relatively low selectivity due to the inability of MS to separate isomers [36]. These limitations highlight the need for a more selective and sensitive technique for strain discrimination.

In this study, we used LC-IM-MS/MS and PS-IM-MS/MS separately as multidimensional analytical techniques combined with chemometric data analysis methods to discriminate seven non-pathogenic *E. coli* strains. The integrated techniques were used to provide complementary separations and multidimensional characterizations of various isomer types needed for accurate identification of lipid isomer biomarkers and clear discrimination of *E. coli* strains. Lipid isomers' annotation based on experimental CCS values was validated using computational approaches such

as molecular dynamics and lipid CCS predictor [117]. Due to the high dimensionality of the LC-IM-MS/MS and PS-IM-MS/MS data, classification was performed using the multivariate analysis methods of principal component analysis (PCA), which reduced the dimensionality of the data, followed by linear discriminant analysis (LDA), which classified all PCA-reduced spectra into independent categories according to the similarities and differences in the molecular composition of the bacterial strains.

5.2. Experimental

5.2.1. Materials

Ultrapure acetonitrile (ACN) and water (H_2O) solvents were purchased from Agilent Technologies (Santa Clara, CA). LC-MS grade isopropanol (IPA) and ammonium acetate were purchased from Sigma-Aldrich (St. Louis, MO USA). LC-MS grade chloroform ($CHCl_3$) was purchased from VWR Chemicals (Radnor, PA) while LC-MS grade methanol (MeOH) was purchased from Honeywell (Muskegon, MI). 1,2-dioleoyl-sn-glycero-3-phospho-(1'-rac-glycerol) (sodium salt) PG (18:1(Δ9)/18:1 (Δ9))-*Cis*, 1,2-dielaidoyl-sn-glycero-3-phospho-(1'-rac-glycerol) (sodium salt) PG (18:1(Δ9)/18:1 (Δ9))-*Trans*, and *E. coli* Polar Lipid Extract (ATCC 11303) were purchased from Avanti Polar Lipids, Inc. (Alabaster, AL). Moreover, a low-concentration ESI tuning mix was purchased from Agilent Technologies (Santa Clara, CA). All reagents and chemicals were used without additional purification.

Stock solutions of these standards (1 μg μL^{-1}) were prepared in $CHCl_3$: MeOH (2:1, v/v) and stored at -20 °C. Then, the stock solutions were diluted in IPA: ACN: H_2O (2:1:1, v/v/v) to a final concentration of 5 ng μL^{-1} for the *E. coli* Polar Lipid Extract and 0.5 ng μL^{-1} for the geometric lipids' isomers.

5.2.2. Culturing conditions and lipid extraction from bacteria

Isolates of seven non-pathogenic *E. coli* strains (K-12, C41, BL21, CSH23, DH10B, DH5α, and S17-1 λpir) were gifted by Dr. Steven Mansoorabadi (Department of Chemistry and Biochemistry, Auburn University) and Dr. Mark Liles (Department of Biological Sciences, Auburn University) and stored at -80 ℃. The bacteria were aliquoted from frozen glycerol stocks into Luria broth (LB) using sterile pipette tips. The liquid cultures were incubated in a forced air incubator (VWR, Chicago, IL) under shaking conditions (220 rpm) at 37 ℃ for 16 h. The number of bacterial cells was measured through absorbance measurements to be $8.10 \pm 0.35 \times 10^8$ CFU/mL (Table 5.1) [164]. All bacterial culturing activities were performed in a biological safety cabinet (Labconco, Kansas City, MO), and biohazardous materials were autoclaved.

Table 5.1 Colony-forming units of the *E. coli* strains.

E. coli strains	(cells/mL) × 10^8
K12	8.71
CSH23	8.38
BL21	7.77
C41	8.29
S17-1 λpir	7.77
DH5α	7.90
DH10B	8.11

Lipids were extracted from bacterial cells according to the Folch method [165]. Briefly, 2 mL of chilled $CHCl_3$/MeOH (2:1) was added to the bacterial suspension and vortexed for 3 minutes. Then, 0.5 mL of chilled water was added to the suspension to induce phase separation, followed by another 1 minute of vortexing followed by centrifugation at 2,800 rpm for 8 minutes. The $CHCl_3$-rich (bottom) phase containing the phospholipids (PLs) was then removed with a sterile pipette tip. The extraction step was repeated twice, and the collected organic phase was diluted with IPA: ACN: H_2O (2:1:1, v/v/v) for analysis.

5.2.3. LC–IM–MS/MS Analyses

All experiments were performed using the Agilent 1290 Infinity LC system and the Agilent 6560 IM-QTOF MS (Agilent Technologies, Santa Clara) instrument described in chapter 2. The separations of the lipid isomers using the reversed-phase (RP) LC were performed by injecting 3 µL of the sample onto a Zorbax RRHD Extend C18 column ((50.0 mm × 2.1 mm i.d., 1.8 µm particle size; Agilent Technologies, Santa Clara, CA) at 45 ℃). Mobile phase A consisted of ACN/H_2O (60:40, v/v), while mobile phase B comprised IPA/ACN (90:10, v/v). Both mobile phases A and B contained 10 mM ammonium acetate for increased signal intensity [166]. Gradient elution was maintained at 55% B for the first 5 minutes and gradually increased to 98% B over the next 5 minutes at a flow rate of 0.4 mL/min, after which the column was equilibrated to baseline conditions for 2 minutes before the next injection, resulting in a total run time of 12 minutes. The same chromatographic conditions were used for both positive and negative ion modes.

The effluent from the RPLC separation was directed to the ESI source of the Agilent 6560 IM-QTOF MS. The conditions for the ESI source were as follows: Drying gas temperature and flow rate, 325 ℃, and 5 L/min; nebulizer gas pressure, 30 psi; sheath gas temperature and flow rate, 275 ℃, and 12 L/min; capillary voltage, 3500 V; nozzle voltage, 1000 V; fragmentor, 400 V; octopole RF, 750 V. The instrument was operated in all-ion IM-MS/MS mode, with ion mobility spectra acquired using a pseudorandom 5-bit sequence (multiplexing mode). In the multiplexing mode, several ion packets are pulsed into the drift tube during each data acquisition cycle, increasing the efficiency of ion utilization within the same dwell time [93]. Ions exiting the drift tube are refocused through the rear funnel into the quadrupole mass filter, allowing total ion transmission into the collision cell for fragmentation. Ion mobility and product ion (MS/MS) scans were acquired in two alternating frames: the low fragmentation frame at 0 V and the high

fragmentation frame at 35 V. The overlapping spectra of the IM data files were deconvoluted using the PNNL PreProcessor software package, version 4.0 (2021.10.27) [167], and further processed using the High-Resolution Demultiplexing (HRdm) tool (v2.0.118) to increase the IM resolving power from ~60 to ~250 [93]. Both low (IM) and high fragmentation (MS/MS) data were exported from the IM-MS Browser (v10.0.1) after averaging the ion mobility tandem mass spectrum, while the LC data were analyzed with MassHunter qualitative software (v10.0) and further processed with Mass Profiler (v10.0.2) to export the relevant LC information (retention time, abundance, *m/z*) for multivariate analysis. The LC-IM-MS/MS data were acquired in positive and negative ion modes in the range of *m/z* 100 - 1700, with the TOF operated in high sensitivity mode at ~20,000 resolution. The IM-MS/MS settings are listed in Table 5.2. CCS measurements of abundant lipid isomers were performed using the single-field method (calibrant-dependent) with a drift field of 18.5 V/cm [85].

Table 5.2. Electrospray ionization (ESI) source and all ions – ion mobility fragmentation (IM-MS/MS) settings.

Parameter	Value	Units
Trap Fill Time	1000	µs
Trap Release Time	100	µs
Frame Rate	0.8	Frames/sec
IM Transient Rate	19	IM Transients/Frame
Max Drift Time	60	ms
TOF Transient Rate	621	Transients/ IM Transients
Drift Tube Entrance	1700	V
Drift Tube Exit	250	V
Rear Funnel Entrance	240	V
Rear Funnel Exit	43	V
Pulsing Sequence Length	5	bit
Low fragmentation frame collision energy	0	V
High fragmentation frame collision energy	35	V

5.2.4. Lipid Identification

The LC-IM all ions fragmentation data were annotated to specific lipids using MS/MS *in silico* spectra matching with MassHunter Lipid Annotator software (Agilent Technologies, Santa Clara, CA) [168]. Glycerophospholipid classes searched for in positive and negative ion modes included phosphatidylethanolamines (PE), phosphatidylglycerols (PG), and cardiolipins (CL) using the data processing parameters given in Table 5.3. Molecular lipids were annotated with the number of carbon atoms and double bonds of the fatty acid in the *sn*-1 position, followed by the number of carbon atoms and double bonds of the fatty acid in the *sn*-2 position. The confidence level of the tentative annotation list was increased by using the lipid CCS predictor to reduce false identifications based on CCS values [117]. The SMILES structure of the molecular lipid was inputted into the CCS predictor and CCS values for $[M+H]^+$, $[M+Na]^+$, and $[M+NH_4]^+$ were searched in positive ion mode and for $[M-H]^-$ in negative ion mode.

Table 5.3. MassHunter Lipid Annotator data processing parameters settings.

Identification parameters	
Mass deviation	≤ 5 ppm
Fragment score	≥ 30
Report dominant constituent if relative abundance differential	≥ 10 %
Library parameters	
Positive ion	+H, +Na, $+NH_4$
Negative ion	-H

5.2.5. Paper spray ambient ionization

We reported in Chapter 3 that the PS ambient ionization method can be used to successfully discriminate various bacteria species rapidly and accurately. In the current study, 8 mL of the cultured bacteria in LB were filtered through a glass fiber filter paper using a Büchner funnel, and the filter paper was allowed to dry at ambient temperatures for about 15 minutes. Then, the filter

papers were cut into several triangles of approximately 8 mm base width and 10 mm height and placed at an optimal distance (~6 mm) from the IM-MS inlet. Spray solvent and high voltage were then applied to generate an electrospray-like plume [86]. Forty microliters of the spray solvent were added, which enabled the extraction of various analytes and efficient paper spray ionization. Afterward, the ions were transported into the IM-MS inlet because of the pressure and voltage gradients, followed by data acquisition in all-ion IM-MS/MS mode, with IM spectra acquired using a pseudorandom 5-bit sequence (multiplexing mode). Post- processing of the IM and MS/MS data for multivariate statistical analysis is performed as in the steps described above for the LC-IM all-ion fragmentation data.

5.2.6. Multivariate statistics

Linear scaling was employed to normalize all tandem mass spectra, and high-resolution IM, LC, and PS data from each replicate. The range of mass is 0~1400 *m/z*, 0~60 ms for drift time, and 0~10 minutes for retention time. Our multivariate statistical analysis was performed on the spectra obtained from LC-IM-MS/MS and PS-IM-MS/MS experiments. The MS data associated with LC-IM-MS/MS experiments were compiled into a matrix (56 by 100561 for positive ion mode, 56 by 808806 for negative ion mode). To reduce the redundant information, *m/z* and drift time selections were successively carried out from IM data. Specifically, for each dataset with IM data, we performed peak identification for mass spectra over all 56 replicates by extracting the most abundant 100 peaks and recorded the corresponding "*m/z*" values. Then, we kept all the ions that were identified in at least 4 replicates. For each selected mass spectrum, we removed the drift time when the abundance was extremely small, i.e., less than 5% of the largest abundance value. For each selected mass spectra and drift time, we recorded the corresponding abundance values.

Therefore, each value in the reconstructed IM data matrix denotes the intensities of bacteria strains with specific drift spectra and mass spectra (56 by 18380 for positive ion mode, 56 by 18011 for negative ion mode). Similarly, peak identification, mass selection, and elimination of extremely small abundance peaks were performed on LC data. Each value in the reconstructed LC data matrix denotes the intensity of bacteria strains with specific retention times and *m/z* (56 by 2421 for positive ion mode, 56 by 2318 for negative ion mode).

Table 5.4. List of *E. coli* strains and their corresponding number of measurements investigated with LC-IM-MS/MS and PS-IM-MS/MS in the negative and positive ion modes.

***E. coli* strains**	**LC-IM-MS/MS**		**PS-IM-MS/MS**	
	Negative	Positive	Negative	Positive
E. coli BL21	8	8	8	7
E. coli C41	8	8	8	8
E. coli CSH23	8	8	8	8
E. coli DH10B	8	8	8	8
E. coli DH5α	8	8	8	8
E. coli K12	8	8	8	8
E. coli S17-1 λpir	8	8	8	8

PCA was applied to the datasets listed in Table 5.4. PCA compressed the original data matrix into a set of independent PCs, which were linear combinations of variables in the original datasets. The similarities among the seven *E. coli* strains and the importance of the original variables in each PC were visualized by a biplot, which overlays a score plot with a loading plot. Besides, based on the proportion of variance explained by each PC, the first three PCs were selected as new variables for subsequent classification. LDA is a widely used statistical classification method, which attempts to differentiate classes using a linear combination of independent variables. In this study, LDA was implemented to distinguish different strains using the new variables generated by PCA in the previous step. To avoid overfitting, we used stratified cross-validation (CV), a popular resampling technique for evaluating models' performance. In this

study, one replicate was chosen at random from each strain to form the testing set (approximately 13% of the dataset), and the rest formed the training set (approximately 87% of the dataset). The LDA model was trained on the training set and tested on the testing set. Furthermore, the stratified CV was repeated 400 times to avoid sampling bias, and the classification accuracies were averaged across all stratified CVs. The model performance was summarized in the confusion matrices (Table 5.5 and Table 5.6). To improve the classification of strains with the PS-IM-MS/MS method, the positive and negative ion mode data were used in conjunction via data fusion. Specifically, the fusion data (56 by 6) was constructed by the combination of extracted PCs from positive and negative ion mode data.

Table 5.5. Confusion matrices associated with LC-IM-MS/MS analysis in the **(A)** Negative and **(B)** Positive ion modes.

(A) Negative ion mode

Total: 56 samples							
Actual / Predicted	BL21	C41	CSH23	DH10B	DH5α	K12	S17-1 λpir
BL21	1	0	0	0	0	0	0
C41	0	1	0	0	0	0	0
CSH23	0	0	1	0	0	0	0
DH10B	0	0	0	1	0	0	0
DH5α	0	0	0	0	1	0	0
K12	0	0	0	0	0	0.86	0.14
S17-1 λpir	0	0	0	0	0	0.14	0.86

(B) Positive ion mode

Total: 56 samples							
Actual / Predicted	BL21	C41	CSH23	DH10B	DH5α	K12	S17-1 λpir
BL21	1	0	0	0	0	0	0
C41	0	1	0	0	0	0	0
CSH23	0	0	1	0	0	0	0
DH10B	0	0	0	1	0	0	0
DH5α	0	0	0	0	1	0	0
K12	0	0	0	0	0	1	0
S17-1 λpir	0	0	0	0	0	0	1

Table 5.6. Confusion matrices associated with PS-IM-MS/MS data obtained in the **(A)** Negative ion mode **(B)** Positive ion mode **(C)** Data fusion.

(A) Negative ion mode

Total: 56 samples							
Actual / Predicted	BL21	C41	CSH23	DH10B	DH5α	K12	S17-1 λpir
BL21	1	0	0	0	0	0	0
C41	0	1	0	0	0	0	0
CSH23	0	0	0.15	0.07	0.04	0	0.19
DH10B	0	0	0.34	0.40	0.15	0.19	0.30
DH5α	0	0	0.15	0.27	0.61	0.09	0.01
K12	0	0	0	0	0	0.72	0
S17-1 λpir	0	0	0.36	0.26	0.20	0	0.50

(B) Positive ion mode

Total: 55 samples							
Actual / Predicted	BL21	C41	CSH23	DH10B	DH5α	K12	S17-1 λpir
BL21	0.86	0	0	0	0	0	0
C41	0.14	0.88	0	0	0	0	0
CSH23	0	0.08	0.28	0	0.49	0	0
DH10B	0	0.04	0.04	0.85	0	0.12	0.12
DH5α	0	0	0.68	0	0.51	0	0
K12	0	0	0	0	0	0.88	0
S17-1 λpir	0	0	0	0.15	0	0	0.88

(B) Data fusion

Total: 55 samples							
Actual / Predicted	BL21	C41	CSH23	DH10B	DH5α	K12	S17-1 λpir
BL21	1	0	0	0	0	0	0
C41	0	0.90	0	0	0	0	0
CSH23	0	0	0.34	0	0.34	0	0
DH10B	0	0.10	0.06	0.85	0	0	0.12
DH5α	0	0	0.60	0	0.66	0	0
K12	0	0	0	0	0	1	0
S17-1 λpir	0	0	0	0.15	0	0	0.88

5.2.7. Computational methods

Classical molecular dynamics (MD) simulations were performed to model and predict the structural changes of the lipid conformers in vacuum. The simulations were performed using a large-scale atomic/molecular massively parallel simulator (LAMMPS). NVT (constant number, volume, and temperature) molecular dynamics simulations were performed using a Nosé-Hoover thermostat at 300 K [92]. The system was pre-equilibrated for 100 ps, and the conformations were sampled every 1 ps from the 200 ps simulations. The trajectory method using the IMoS software package was used to compute the CCS values of the 200 structures at 3.95 Torr and 300 K [91]. Single-point energy calculations at the B3LYP/6-31G(d,p) level were used to calculate the energies of the 200 structures.

5.3. Results and Discussion

5.3.1. Complementary separations of lipid isomers and conformers

Since lipids are significant disease biomarkers, effective separation of lipid isomers is crucial to knowing the lipid isomer composition for accurate diagnosis of diseases. Geometric isomers, particularly *trans* isomers, unlike *cis* isomers, are associated with metabolic disease and colon cancer, highlighting the need for efficient separation. Since conventional MS measurements cannot distinguish geometric isomers, we interfaced a complementary separation method, LC, with the MS technique to provide orthogonal separation. A mixture of PG (18:1(9Z)/18:1 (9Z))-*Cis* and PG (18:1(9E)/18:1 (9E))-*Trans* isomers was analyzed (Figure 5.1A).

The LC dimension provided a baseline separation of the *cis* and *trans* isomers (resolution (r) ~ 2.1, Figure 5.1B). The *cis* double bond geometry causes more kinks in the lipid backbone

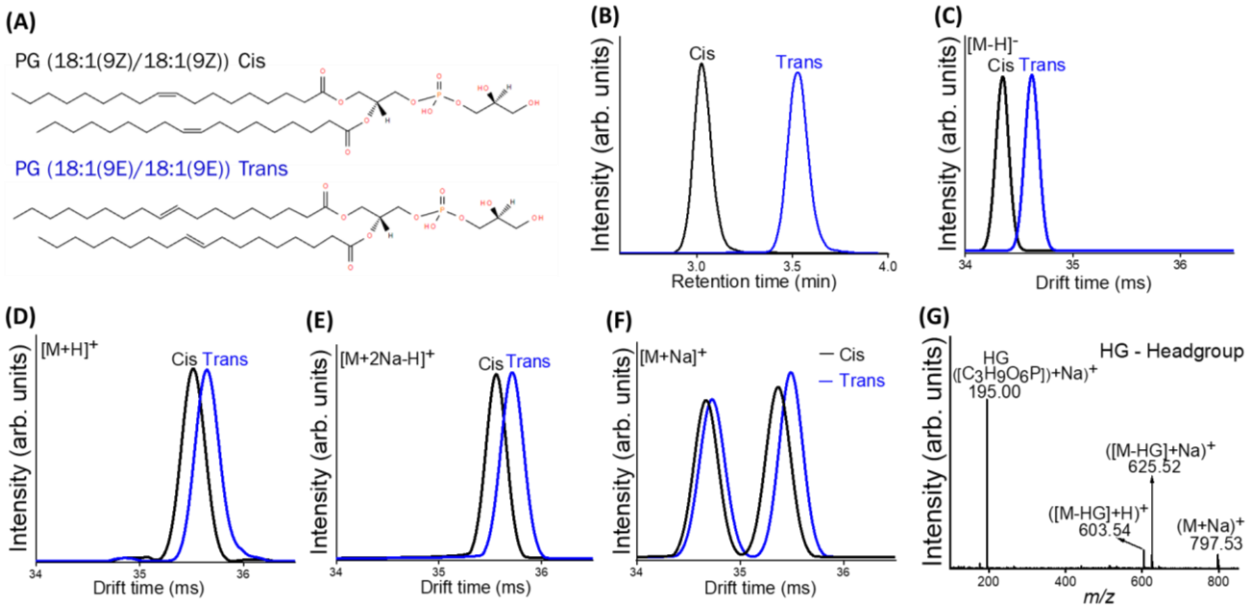

Figure 5.1. A) Structure of PG (36:2) *cis* and *trans* geometric isomers. Separation of a mixture of PG (36:2) *cis* and *trans* isomers with (B) LC separation and Ion mobility using (C) $[M-H]^-$ (D) $[M+H]^+$ (E) $[M+2Na-H]^+$ (F) $[M+Na]^+$ ions. (G) Tandem MS spectrum of PG 36:2 *cis* and *trans* $[M+Na]^+$ adducts.

than the *trans* configuration, resulting in reduced surface hydrophobicity of the *cis* isomer. This results in the *cis* isomer being more polar than the *trans* isomer. Since the separation mechanism in reversed-phase LC (RPLC) depends on polarity, the *cis* and *trans* isomers were effectively separated.

IM, a post-ionization separation technique, in contrast to LC, a pre-ionization separation technique, provides the ability to use ionization adducts to influence separation to different degrees. The *cis/trans* isomers were observed predominantly in the negative ion mode as the deprotonated species, $[M-H]^-$. The two isomers were nearly baseline resolved. They showed a drift time difference (which reflects the degree of separation) of 0.72%, as observed in Figure 5.1C. Of note, the IM-based resolution obtained here is significantly higher than that obtained previously (Figure 3.10D) which elucidates the resolution enhancement upon implementing HRdm. The

double bonds with *cis* orientation curved the backbone more than those with *trans* orientation, resulting in a difference in the corresponding size and shape leading to an effective IM separation of the two geometric isomers. In the positive ion mode, the predominantly observed ions include $[M+H]^+$, $[M+Na]^+$, and $[M+2Na-H]^+$. Cationization with alkali metals such as sodium and potassium has been reported to improve the separation of isomeric compounds [169, 170]. As illustrated by the arrival time distributions (ATDs) presented in Figure 5.1D and Figure 5.1E, the drift time differences between the two geometric isomers were 0.36% and 0.42% for their $[M+H]^+$ and $[M+2Na-H]^+$ adducts, respectively. The effect of metal adduction is more pronounced in the $[M+Na]^+$ adducts of the geometric isomers as two new conformations of the *cis* and *trans* isomers were revealed and baseline separated. The drift time difference between the two new conformers of the *cis* isomer is 2.0% (Figure 5.1F, black trace). Similar observations were made with the *trans* isomer, as shown in the extracted ion mobilogram (EIM) (Figure 5.1F, blue trace). These observations suggest that the sodium adduct interacts with the fatty acid moieties of the geometric isomers [170], and consequently leads to a more pronounced change in lipid ion structure, resulting in each isomer adopting two new conformations that are more easily distinguished by their drift times.

As shown in Table 5.7, the experimental CCS values of the two conformations of the [*cis* + $Na]^+$ are $\Omega_1 = 279.8 \pm 0.5$ Å^2 and $\Omega_2 = 284.5 \pm 0.6$ Å^2 and the [*trans* + $Na]^+$ are $\Omega_1 = 280.3 \pm 0.4$ Å^2 and $\Omega_2 = 285.5 \pm 0.5$ Å^2. We performed MD simulations to assign theoretical structures to the experimental CCS values of the *cis* and *trans* conformers. As shown in Figure 5.1, two new conformers of *cis* and *trans* isomers revealed by IM separation were inseparable with LC and undistinguishable with tandem MS (Figure 5.1G). These results demonstrate the advantage of

using complementary separation methods for complete characterization and separation of lipid isomers and conformers.

Table 5.7. Experimental and theoretical CCS values of the sodiated geometric isomers of PG (36:2) lipids

Species	Experimental CCS (Å^2)	Theoretical CCS (Å^2)	% Difference
Cis $[M+Na]^+$	279.8	285.5	2.0
	284.5	288.5	1.4
Trans $[M+Na]^+$	280.3	291.2	3.8
	285.5	293.9	2.9

The MD simulations trajectories of the sodiated *cis* and *trans* lipids showed that the two acyl chains undergo large structural fluctuations due to the thermal energy at 300 K. Similar to previous studies, no clear subset of geometry through the whole set of MD simulations was observed in the scatter plot of collision cross sections versus the conformations (Figure 5.2) [86, 171]. Hence, we considered the theoretical structures closest in CCS values to the experimental CCS values. The theoretical CCS of the two MD simulated conformers of [*cis* + Na]$^+$ closest to the experimental values are Ω_1 = 285.5 Å^2 and Ω_2 = 288.5 Å^2 and those of [*trans* + Na]$^+$ are Ω_1 =291.2 Å^2 and Ω_2 = 293.9 Å^2. We observed good agreement between the experimental and theoretical CCS values, as the difference is less than 4%. The zero-point energy structures of the two conformers of [*cis* + Na]$^+$, as shown in Figure 5.3A, indicate that the two acyl chains of the small conformer are more folded inwardly than those of the large conformer i.e., the small conformer has a more globular-like conformation than the large conformer. The degree of folding of the two acyl chains is the major structural difference between the two MD simulated conformations of [*trans* + Na]$^+$. The small conformer of the [*trans* + Na]$^+$ has the two acyl chains wrapped more inwardly than the large conformer (Figure 5.3B).

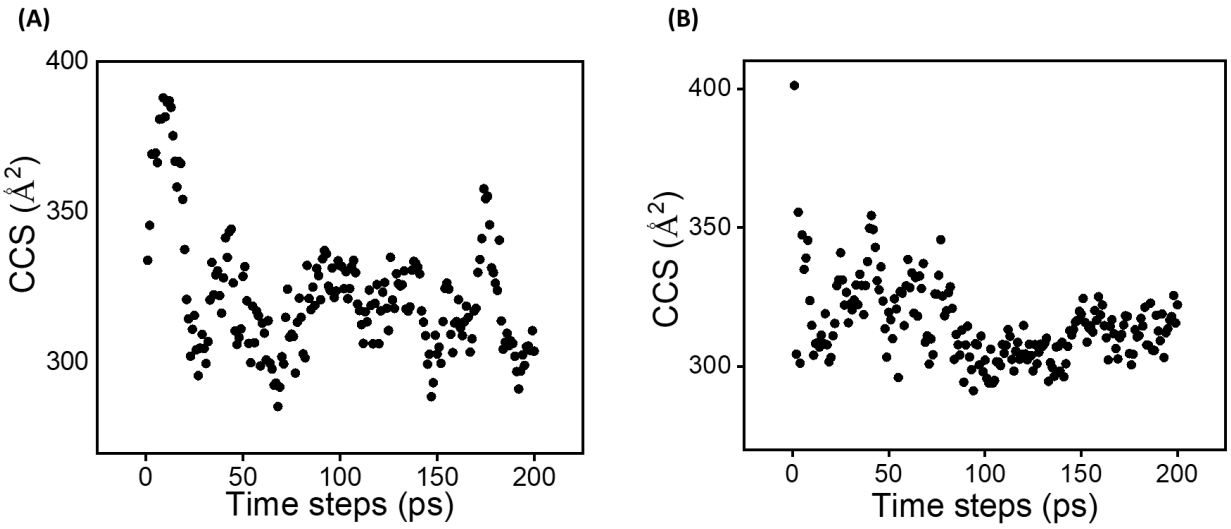

Figure 5.2. Scatter plots of collision cross section values vs. conformations for 200 structures sampled from MD simulations for **(A)** PG (18:1(9Z)/18:1 (9Z))-*Cis* and **(B)** PG (18:1(9E)/18:1 (9E))-*Trans*.

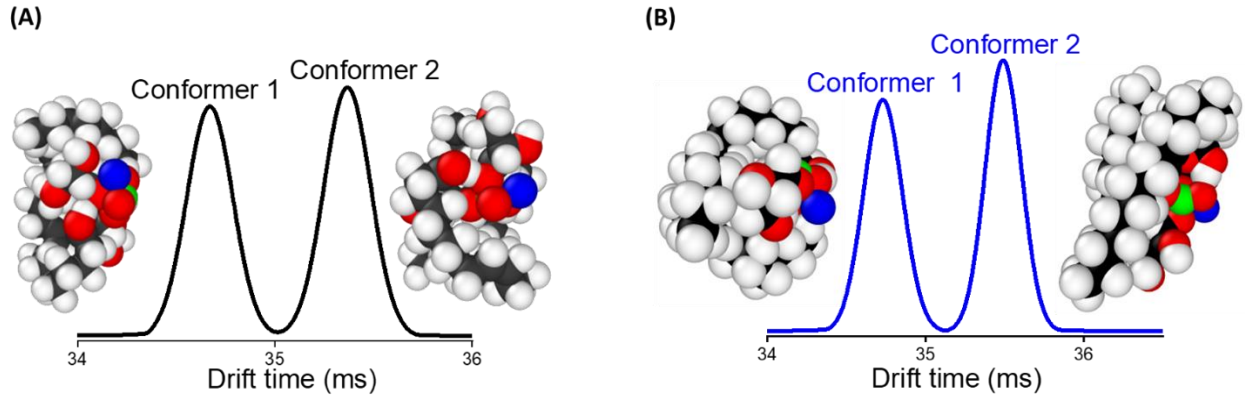

Figure 5.3. Molecular dynamics (MD) simulated conformations of the sodiated $[M+Na]^+$ adduct of the geometric isomers for **(A)** PG (18:1(9Z)/18:1 (9Z))-*Cis* and **(B)** PG (18:1(9E)/18:1 (9E))-*Trans*.

5.3.2. Multidimensional characterization and separation of lipid isomers in *E. coli* lipid extract

The lipidome of bacteria exhibits an abundance of lipid isomers that serve as biomarkers for accurate disease diagnosis. Due to the structural complexity associated with lipid isomers, we used a complementary LC-IM-all ions fragmentation method to provide multidimensional separation to resolve various lipid isomers in *E. coli* extracts. The LC separation shown in Figure 5.4A indicates that the major lipid species in *E. coli* membranes are phosphatidylethanolamines (PEs, rt: 3.5 - 6.5 min), followed by phosphatidylglycerols (PGs, rt: 2 - 4 min) and cardiolipins (CLs, rt: 2-4 min, Figure 5.5).

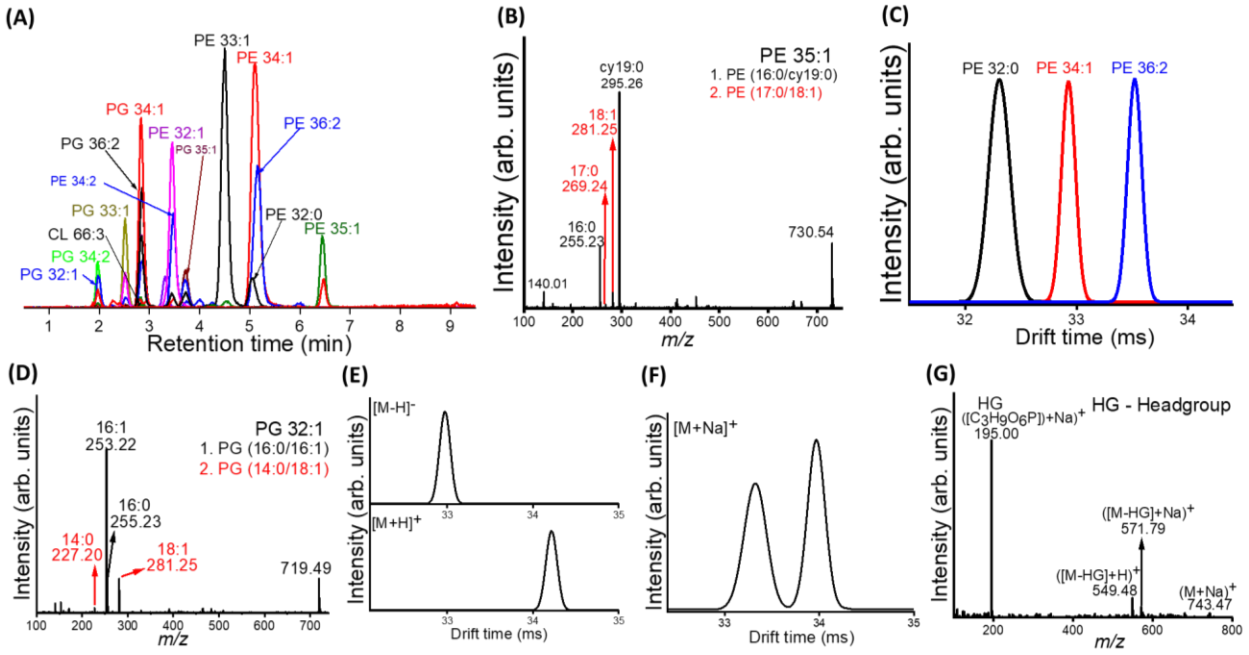

Figure 5.4. (A) RPLC separation of lipids in *E. coli* polar lipid extract (B) Tandem MS spectrum of [PE 35:1-H]$^-$ showing 2 lipid isomers: PE (16:0/cy19:0) and PE (17:0/18:1) (C) IM separation of PE (32:0), PE (34:1), and PE (36:2) (D) Tandem MS spectrum of [PG 32:1-H]$^-$ showing 2 lipid isomers: PG (16:0/16:1) and PG (14:0/18:1). Drift spectra of (E) of PG (32:1) ([M-H]$^-$ top panel) and ([M+H]$^-$ bottom panel) (F) [M+Na]$^+$ of PG (32:1). (G) Tandem MS spectrum of PG (32:1) *cis* and *trans* [M+Na]$^+$ adducts.

We structurally annotate the lipids using MS/MS *in silico* spectra matching with further manual identification using fragmentation mechanisms of glycerophospholipids (PEs, PGs, CLs) described in detail in previous studies [39, 172]. For instance, the CID spectrum of *m/z* 730.54 shown in Figure 5.4B revealed characteristics of fragment ions at *m/z* 255.23, 269.24, 281.25, and 295.26, corresponding to the carboxylate anions of C16:0, C17:0, C18:1, and Ccy19:0, respectively [39]. The characteristic ion at *m/z* 140.01 is $[C_2H_7O_4NP]^-$, which is a head group, confirmed the identity of the lipid as PE. Therefore, we confidently annotated the lipid ion *m/z* 730.54 as PE (16:0/cy19:0) and PE (17:0/18:1). Moreover, tandem mass spectrometry measurement was used to accurately annotate the isomers of PGs and CLs, while their sum composition was reported in the LC chromatogram. To confidently improve the identification of the lipid isomers in the *E. coli* extract, we utilized single-field measurements to estimate the CCS of the lipid isomers. The CCS of five ions of the lipid isomers were experimentally estimated, which include $[M-H]^-$ for negative ionization and $[M+H]^+$, $[M+Na]^+$, $[M+NH_4]^+$, and $[M+2Na-H]^+$ for positive ionization (Table 5.8). For instance, the CCS values of $[M-H]^-$, $[M+H]^+$, $[M+Na]^+$, and $[M+NH_4]^+$ of PE (17:0/18:1) are 269.1, 278.8, 282.5, and 281.2 $Å^2$, respectively, which differ less than 0.6% from the theoretical CCS values, 267.6, 279.2, 280.8, and 280.5 $Å^2$, respectively (Table 5.8). Not only do the CCS values support the annotation of the lipid structures, but they also effectively remove potential false identifications from *m/z*, retention time, and MS/MS matches. Using the four-dimensional data of retention time (LC), CCS (IM), *m/z*, and MS/MS, 34 acyl chain lipid isomers containing 18 PEs, 13 PGs, and 3 CLs were identified confidently in the *E. coli* lipid extract.

After comprehensive characterization of the lipid isomers, we used the orthogonal separation from the complementary LC-IM-MS/MS method to resolve co-eluting lipid isomers

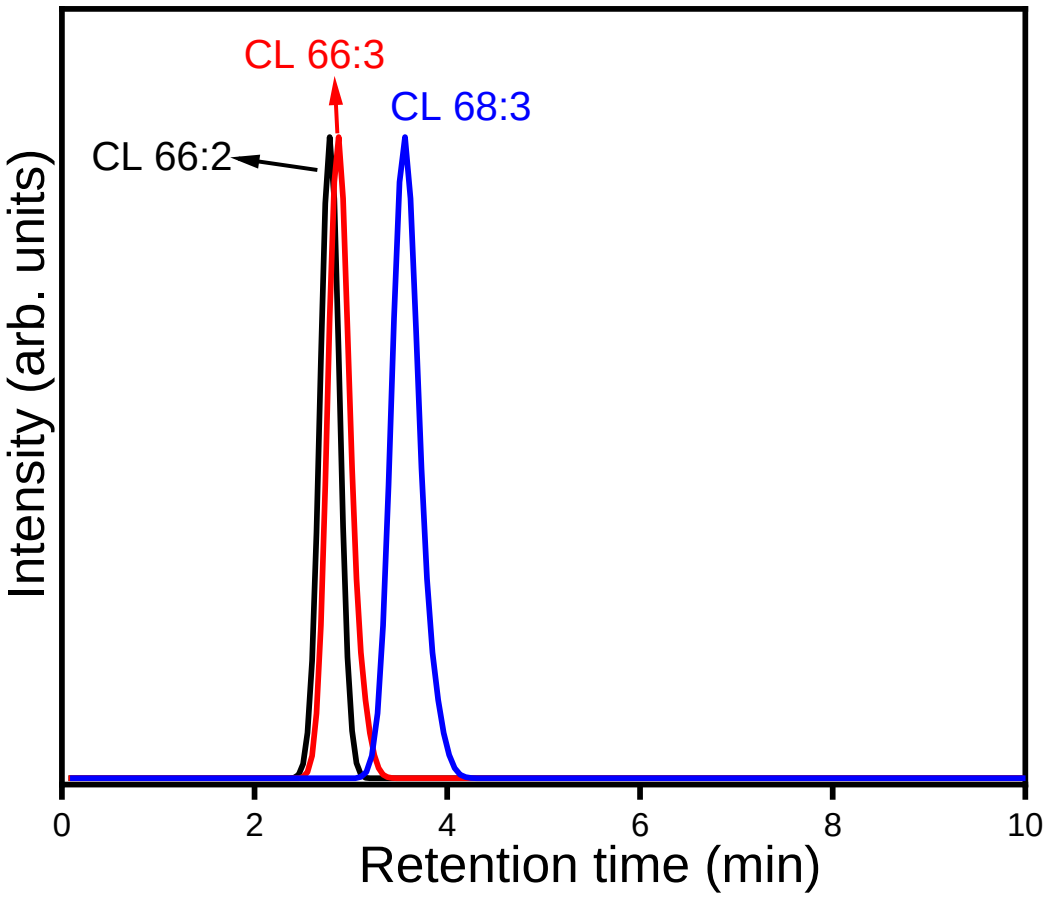

Figure 5.5. Extracted ion chromatogram of the cardiolipins detected in the *E. coli* polar lipid extract using reversed phase liquid chromatography.

conformers in the *E. coli* extract. PE (32:0), PE (34:1), and PE (36:2) differ respectively by one ethylene unit co-eluted in the LC dimension (rt: ~5.2 min, Figure 5.4A). Increasing double bonds has been shown in previous studies to increase lipid polarity and consequently decrease their retention times, whereas increasing side chain length increases lipid hydrophobicity and therefore increases their retention times [39]. From PE (32:0) to PE (34:1), there is an increase in both the side chain length and the number of double bonds. Hence, the increasing lipid polarity (decreasing rt) nullifies the increasing lipid hydrophobicity (increasing rt), resulting in the co-elution of these LC peaks. However, the IM dimension was very effective, providing a baseline separation of the

three LC co-eluted peaks (Figure 5.4C). The lipid species PE (32:0), PE (34:1), and PE (36:2) differ respectively by one ethylene unit, which corresponds to a drift time difference of 2.0%. Consequently, they are baseline-resolved since IM separation depends on structure and size in contrast to LC which depends on polarity. We further demonstrate the integrated method, LC-IM-MS/MS, to provide complementary and multidimensional separation of acyl chain lipid isomers and conformers in *E. coli* extract. The $[M-H]^-$ adduct of PG (32:1) (*m/z* 719.49) was annotated as PG (14:0/18:1) and PG (16:0/16:1) using tandem MS (Figure 5.4D). The characteristic fragment ions at *m/z* 227.20 and 281.25 correspond to the carboxylate anions of C14:0 (*sn*-1) and C18:1 (*sn*-2), while *m/z* 255.23 and 253.22 correspond to the carboxylate anions of C16:0 (*sn*-1) and C16:1 (*sn*-2). However, the two PG acyl chain isomers were unresolved in the LC dimension (rt: 2.0 min, Figure 5.4A) and IM dimension (drift time: 32.96 ms, negative ion mode, Figure 5.4E, top panel). In the positive ionization mode, the $[M+H]^+$ adduct of the PG (32:1) (*m/z* 721.51) shows a single IM peak indicating that the two PG acyl chain isomers are unresolved (Figure 5.4E, bottom panel). However, the $[M+Na]^+$ spectrum shows two major IM peaks which were suggested to present two isomers or conformers of the acyl chain isomers due to the interaction of the sodium adduct with the fatty acyl moieties (Figure 5.4F). We could not distinguish the two conformations using tandem mass spectrometry as their MS/MS show similar fragmentation patterns (Figure 5.4G). The predominant product ions observed from the tandem MS spectrum at *m/z* 549.48 and 195.00 correspond to the protonated diglyceride-like ion and sodiated polar head group ion, respectively. The ion at *m/z* 571.79 corresponds to a sodium ion attached to the diglyceride-like ion. This result demonstrates the advantage of complementary separation techniques in an integrated fashion to resolve and characterize lipid isomers as diagnostic biomarkers for bacterial diseases.

Table 5.8. Isomeric lipids present in *E. coli* and their experimental m/z and CCS values in comparison to their corresponding theoretical values.

	Formula	Isomers	Adducts	Theoretical *m/z*	Experimental *m/z*	*m/z* error (ppm)	Exp. CCS (Å^2)	Lipid CCS* (Å^2)	% Diff.
PG 37:2	$C_{43}H_{81}O_{10}P$	(18:1/19:1)	$[M-H]^-$	787.5495	787.5476	2.41	280.3	276.3	1.45
PG 36:2	$C_{42}H_{79}O_{10}P$	(18:1/18:1)	$[M-H]^-$	773.5338	773.5318	2.59	277.1	273.6	1.28
			$[M+H]^+$	775.5484	775.5467	2.19	287.9	286.9	0.35
			$[M+Na]^+$	797.5303	797.5286	2.13	-	288.4	-
			$[M+NH_4]^+$	792.5749	792.5732	2.14	288.7	288.1	-
			$[M+2Na-H]^+$	819.5122	819.5105	1.01	287.8	-	-
PG 36:1	$C_{42}H_{81}O_{10}P$	(18:0/18:1)	$[M-H]^-$	775.5495	775.5484	1.42	278.5	275.1	1.24
			$[M+H]^+$	777.5640	777.5630	1.28	-	289.6	
PG 35:1	$C_{41}H_{79}O_{10}P$	(16:0/19:1)	$[M-H]^-$	761.5338	761.5313	3.28	275.4	272.1	1.21
			$[M+H]^+$	763.5484	763.5472	1.57	-	286.0	
			$[M+Na]^+$	785.5303	785.5291	1.20	-	287.5	
			$[M+NH_4]^+$	780.5749	780.5736	1.66	-	287.2	
PG 35:2	$C_{41}H_{77}O_{10}P$	(17:1/18:1)	$[M-H]^-$	759.5182	759.5156	3.42	274.1	270.2	1.44
			$[M+H]^+$	761.5327	761.5313	1.84	-	283.0	-
			$[M+Na]^+$	783.5147	783.5125	2.81	-	284.6	-
			$[M+NH_4]^+$	778.5593	778.5571	2.83	-	284.2	-
PG 34:1	$C_{40}H_{77}O_{10}P$	(16:0/18:1)	$[M-H]^-$	747.5182	747.5169	1.74	272.1	269.3	1.04
			$[M+H]^+$	749.5327	749.5314	1.73	285.4	283.5	0.67
			$[M+Na]^+$	771.5147	771.5130	2.20	-	285.0	-
			$[M+NH_4]^+$	766.5593	766.5577	2.09	286.1	284.7	-
			$[M+2Na-H]^+$	793.4977	793.4947	3.78	282.4	-	-
PG 34:2	$C_{40}H_{75}O_{10}P$	(18:1/16:1)	$[M-H]^-$	745.5025	745.4992	4.43	270.8	267.7	1.16
			$[M+H]^+$	747.5171	747.5160	1.47	-	280.6	-
			$[M+Na]^+$	769.4977	769.4975	1.91	-	282.1	-
			$[M+NH_4]^+$	764.5436	764.5419	2.22	-	281.7	-
PG 33:1	$C_{39}H_{75}O_{10}P$	(16:0/17:1)	$[M-H]^-$	733.5025	733.5003	3.00	268.1	265.6	1.47
			$[M+H]^+$	735.5171	735.5154	2.31	-	279.7	-
			$[M+Na]^+$	757.4990	757.4973	2.24	-	281.3	-
			$[M+NH_4]^+$	752.5436	752.5420	2.13	-	280.9	-
PG 32:0	$C_{38}H_{75}O_{10}P$	(16:0/16:0)	$[M-H]^-$	721.5025	721.4996	4.02	267.5	264.2	1.25
			$[M+H]^+$	723.5171	723.5159	1.64	-	280.4	-
			$[M+Na]^+$	745.4990	745.4979	1.47	-	282.0	-
			$[M+NH_4]^+$	740.5436	740.5427	1.22	-	281.6	-
PG 32:1	$C_{38}H_{73}O_{10}P$	(16:0/16:1)	$[M-H]^-$	719.4869	719.4839	4.17	265.8	262.6	1.22
			$[M+H]^+$	721.5014	721.5001	1.80	-	277.3	-
			$[M+Na]^+$	743.4834	743.4819	2.00	-	278.8	-
			$[M+NH_4]^+$	738.5280	738.5264	2.16	-	278.5	-
			$[M+2Na-H]^+$	765.4664	765.4634	3.91	-	-	-
		(14:0/18:1)	$[M-H]^-$	719.4869	719.4839	4.17	265.8	263.3	0.99
			$[M+H]^+$	721.5014	721.5001	1.80	-	-	-
			$[M+Na]^+$	743.4834	743.4819	2.00	-	-	-
			$[M+NH_4]^+$	738.5280	738.5264	2.16	-	-	-
			$[M+2Na-H]^+$	765.4664	765.4634	3.91	-	-	-
PG 30:0	$C_{36}H_{71}O_{10}P$	(16:0/14:0)	$[M-H]^-$	693.4712	693.4707	0.72	261.7	258.2	1.36
			$[M+H]^+$	695.4858	695.4863	0.71	-	274.2	-
			$[M+Na]^+$	717.4677	717.4672	0.69	-	275.8	-
			$[M+NH_4]^+$	712.5123	712.5122	0.14	-	275.4	-
			$[M+2Na-H]^+$	739.4507	739.4478	3.92	-	-	-
PG 30:1	$C_{36}H_{69}O_{10}P$	(14:0/16:1)	$[M-H]^-$	691.4556	691.4537	2.75	-	256.5	-
			$[M+H]^+$	693.4701	693.4717	2.30	-	270.9	-
			$[M+Na]^+$	715.4521	715.4527	0.84	-	272.5	-
			$[M+NH_4]^+$	710.4967	710.4974	0.98	-	272.1	-
			$[M+2Na-H]^+$	737.4351	737.4320	4.20	-	-	-
PE 37:2	$C_{42}H_{80}NO_8P$	(18:1/19:1)	$[M-H]^-$	756.5549	756.5524	3.30	273.7	272.2	0.55
			$[M+H]^+$	758.5694	758.5681	1.71	282.75	282.7	0.02
			$[M+Na]^+$	780.5514	780.5501	1.66	-	272.5	-
			$[M+NH_4]^+$	775.5960	775.5946	1.80	-	284.0	-
			$[M+2Na-H]^+$	802.5344	802.5320	2.99	-	-	-

PE 36:2	$C_{41}H_{78}NO_8P$	(18:1/18:1)	$[M-H]^-$	742.5392	742.5375	2.29	270.4	269.4	0.37
			$[M+H]^+$	744.5538	744.5530	1.07	277.7	280.1	-0.86
			$[M+H]^+$	744.5538	744.5530	1.07	279.7	280.1	-0.14
			$[M+H]^+$	744.5538	744.5530	1.07	281.3	280.1	0.42
			$[M+Na]^+$	766.5357	766.5342	1.95	282.43	281.7	0.26
			$[M+NH_4]^+$	761.5803	761.5811	1.05	-	281.3	-
			$[M+2Na-H]^+$	788.5188	788.5158	3.80	-	282.6	-
		(cy19:0/cy17:0)	$[M-H]^-$	742.5392	742.5375	2.29	270.4	269.7	0.26
			$[M+H]^+$	744.5538	744.5530	1.07	277.7	280.1	-0.86
			$[M+Na]^+$	766.5357	766.5342	1.95	282.4	281.7	0.26
			$[M+NH_4]^+$	761.5803	761.5811	1.05	-	281.3	-
			$[M+2Na-H]^+$	788.5188	788.5158	3.80	-	282.6	-
PE 36:1	$C_{41}H_{80}NO_8P$	(18:0/18:1)	$[M-H]^-$	744.5549	744.5518	4.16	272.1	270.9	0.44
PE 35:1	$C_{40}H_{78}NO_8P$	(16:0/cy19:1)	$[M-H]^-$	730.5392	730.5390	0.27	269.1	268.0	0.41
			$[M+H]^+$	732.5538	732.5527	1.50	278.8	279.2	-0.14
			$[M+Na]^+$	754.5357	754.5342	1.98	282.5	280.8	0.59
			$[M+2Na-H]^+$	776.5188	776.5163	3.21	283.1	-	-
		(17:0/18:1)	$[M-H]^-$	730.5392	730.539	0.27	269.1	267.6	0.56
			$[M+H]^+$	732.5538	732.5527	1.50	278.8	279.2	-
			$[M+Na]^+$	754.5357	754.5342	1.98	282.5	280.8	-
			$[M+NH_4]^+$	749.5803	749.5823	3.21	281.2	280.5	-
		(18:0/cy17:0)	$[M-H]^-$	730.5392	730.5390	0.27	269.1	267.6	0.56
			$[M+H]^+$	732.5538	732.5527	1.50	278.8	-	-
			$[M+Na]^+$	754.5357	754.5342	1.98	282.5	-	-
			$[M+2Na-H]^+$	776.5188	776.5163	3.21	-	-	-
PE 35:2	$C_{40}H_{78}NO_8P$	(17:1/18:1)	$[M-H]^-$	728.5236	728.5222	1.92	267.4	266.0	0.53
PE 34:2	$C_{39}H_{74}NO_8P$	(16:1/18:1)	$[M-H]^-$	714.5079	714.5062	2.38	263.9	263.3	0.23
			$[M+H]^+$	716.5225	716.5218	0.90	271.1	273.2	-0.77
			$[M+H]^+$	716.5225	716.5218	0.90	273.9	273.2	0.25
			$[M+H]^+$	716.5225	716.5218	0.90	275.6	273.2	0.87
			$[M+Na]^+$	738.5044	738.5031	1.76	276.9	274.9	0.73
			$[M+NH_4]^+$	733.5490	733.5494	0.54	-	274.5	-
			$[M+2Na-H]^+$	760.4875	760.4850	3.28	-	-	-
		(cy17:0/cy17:0)	$[M-H]^-$	714.5079	714.5062	2.38	263.9	263.0	0.34
			$[M+H]^+$	716.5225	716.5218	0.90	-	-	-
			$[M+Na]^+$	738.5044	738.5031	1.76	-	-	-
			$[M+NH_4]^+$	733.549	733.5494	0.54	-	-	-
			$[M+2Na-H]^+$	760.4875	760.485	3.28	-	-	-
PE 34:1	$C_{39}H_{76}NO_8P$	(16:0/18:1)	$[M-H]^-$	716.5236	716.5225	1.54	265.6	265.0	0.23
			$[M+H]^+$	718.5381	718.5374	0.97	275.2	276.6	-0.51
			$[M+Na]^+$	740.5201	740.5188	1.75	279.5	278.2	0.46
			$[M+2Na-H]^+$	762.5031	762.5006	3.27	278.4	-	-
PE 33:1	$C_{38}H_{74}NO_8P$	(16:0/17:1)	$[M-H]^-$	702.5079	702.5065	1.99	262.8	261.3	0.57
			$[M+H]^+$	704.5225	704.5219	0.85	272.6	272.4	0.06
			$[M+Na]^+$	726.5044	726.5036	1.10	273.0	274.1	-0.4
			$[M+Na]^+$	726.5044	726.5036	1.10	275.8	274.1	0.62
			$[M+2Na-H]^+$	748.4875	748.4851	3.20	276.8	-	-
PE 32:0	$C_{37}H_{74}NO_8P$	(16:0/16:0)	$[M-H]^-$	690.5079	690.5051	4.05	260.0	259.9	0.04
			$[M+H]^+$	692.5225	692.5213	1.71	272.3	273.3	-0.37
			$[M+Na]^+$	714.5044	714.5034	1.39	-	275.0	-
			$[M+NH_4]^+$	709.5490	709.5483	0.98	-	274.6	-
			$[M+2Na-H]^+$	736.4875	736.4849	3.53	-	-	-
PE 32:1	$C_{37}H_{72}NO_8P$	(16:0/16:1)	$[M-H]^-$	688.4923	688.4912	1.60	259.1	258.2	0.35
			$[M+H]^+$	690.5068	690.5062	0.86	268.3	269.8	-0.54
			$[M+Na]^+$	712.4888	712.4875	1.82	273.0	271.5	0.55
			$[M+NH_4]^+$	707.5334	707.5309	3.53	-	271.1	-
			$[M+2Na-H]^+$	734.4718	734.4694	3.26	271.6	-	-
PE 31:1	$C_{36}H_{70}NO_8P$	(15:0/16:1)	$[M-H]^-$	674.4766	674.4759	1.04	257.0	254.9	0.82
			$[M+H]^+$	676.4912	676.4898	2.06	-	265.5	-
			$[M+Na]^+$	698.4731	698.4717	2.00	-	267.2	-
			$[M+2Na-H]^+$	720.4562	720.4549	1.80	-	-	-
		(14:0/17:1)	$[M-H]^-$	674.4766	674.4759	1.04	257.0	255.2	0.71
			$[M+H]^+$	676.4912	676.4898	2.06	-	265.5	-
			$[M+Na]^+$	698.4731	698.4717	2.00	-	267.2	-
PE 30:0	$C_{35}H_{70}NO_8P$	(14:0/16:0)	$[M-H]^-$	662.4766	662.4745	3.17	254.9	253.7	0.47
			$[M+H]^+$	664.4912	664.4900	1.80	266.47	266.6	0.05

			$[M+Na]^+$	686.4731	686.4714	2.47	270.4	268.3	0.78
PE 30:1	$C_{35}H_{68}NO_8P$	(14:0/16:1)	$[M-H]^-$	660.4610	660.4584	3.94	253.0	252.0	0.40
			$[M+H]^+$	662.4755	662.4738	2.56	-	263.0	-
			$[M+Na]^+$	684.4575	684.4563	1.75	-	264.6	-
CL 66:2	$C_{75}H_{142}O_{17}P_2$		$[M-2H]^{2-}$	687.4788	687.4794	-0.87	-	-	-
			$[M+2H]^{2+}$	689.4934	689.4945	-025	-	-	-
CL 66:3	$C_{75}H_{140}O_{17}P_2$		$[M-2H]^{2-}$	686.4710	686.4713	-0.44	-	-	-
CL 68:3	$C_{77}H_{144}O_{17}P_2$		$[M-2H]^{2-}$	700.4867	700.4865	0.29	-	-	-

- collision cross section values not found

5.3.3. Differentiation of *E. coli* strains by LC–IM–MS/MS

The close biological relationship between the *E. coli* strains is strongly reflected in their lipidomic profiles, showing high similarity in their mass spectral profiles, as observed in Figure 5.6 and Figure 5.7. This challenge highlights the need for a highly selective method, in this case, LC–IM–MS/MS for accurate discrimination of the strains. We utilized seven *E. coli* strains, including BL21, C41, CSH23, DH10B, DH5α, K12, and S17-1 λpir, to demonstrate the high discriminatory power of this integrated technique. In the negative ionization mode, the predominant ionic species observed was the deprotonated $[M-H]^-$ species. The most abundant $[M-H]^-$ ions observed across the seven *E. coli* strains are *m/z* 674.48, 688.49, 702.51, 716.53, 728.53, 730.54, 733.51, and 742.54 assigned to be [PE (31:1)-H]$^-$, [PE (32:1)-H]$^-$, [PE (33:1)-H]$^-$, [PE (34:1)-H]$^-$, [PE (35:2)-H]$^-$, [PE (35:1)-H]$^-$, [PG (33:1)-H]$^-$, and [PE (36:2)-H]$^-$, respectively (Figure 5.6). The annotation of these lipids was confirmed by CCS measurements, isotopic abundances, and exact mass measurements. For instance, using single-field measurements, the experimental CCS values of *m/z* 716.53 [PE (34:1)-H]$^-$ is 265.6 Å^2 which differs by 0.23% from the Lipid CCS predictor value, 265.0 Å^2 (Table 5.8).

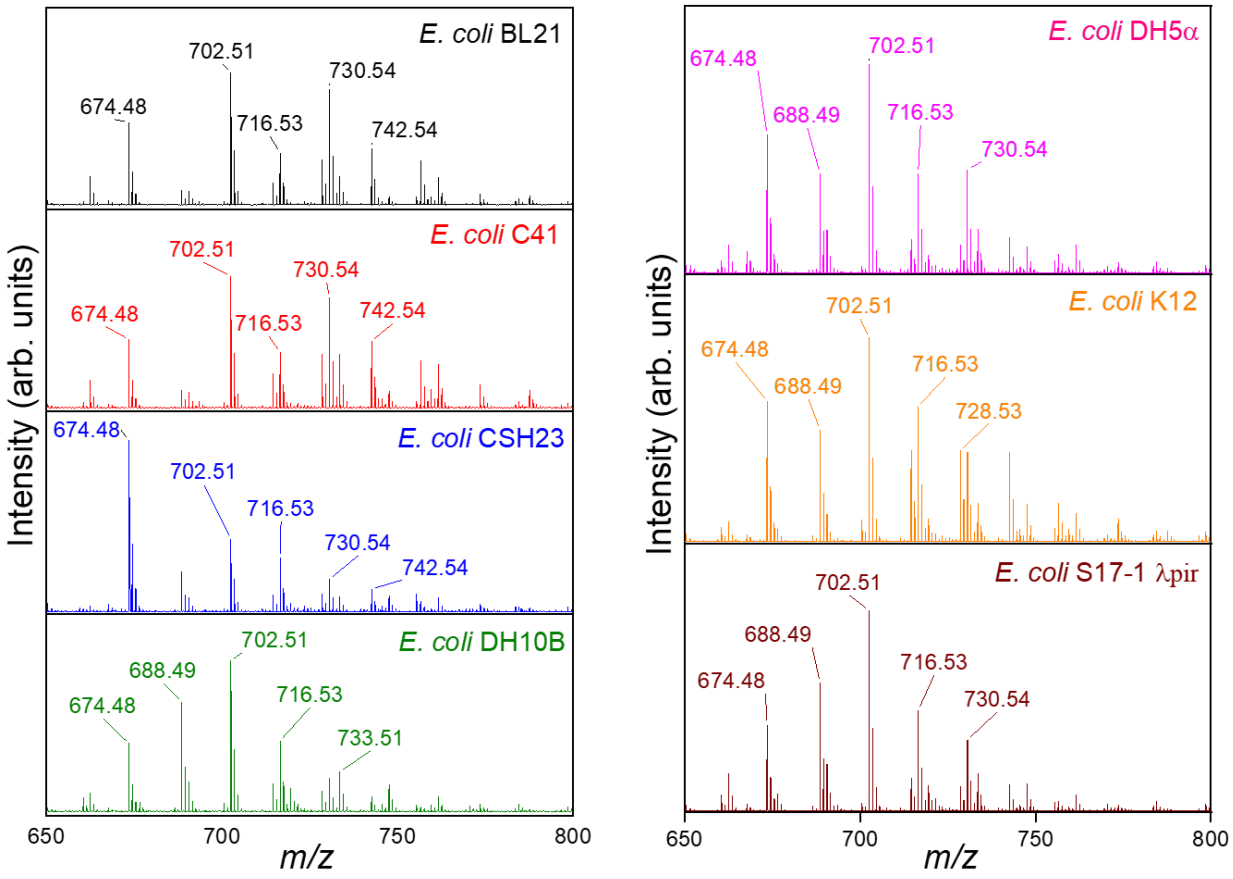

Figure 5.6. Mass spectra of the seven E. coli strains: BL21, C41, CSH23, DH10B, DH5α, K-12, and S17-1 λpir obtained by LC-IM-MS/MS analysis in the negative ion mode.

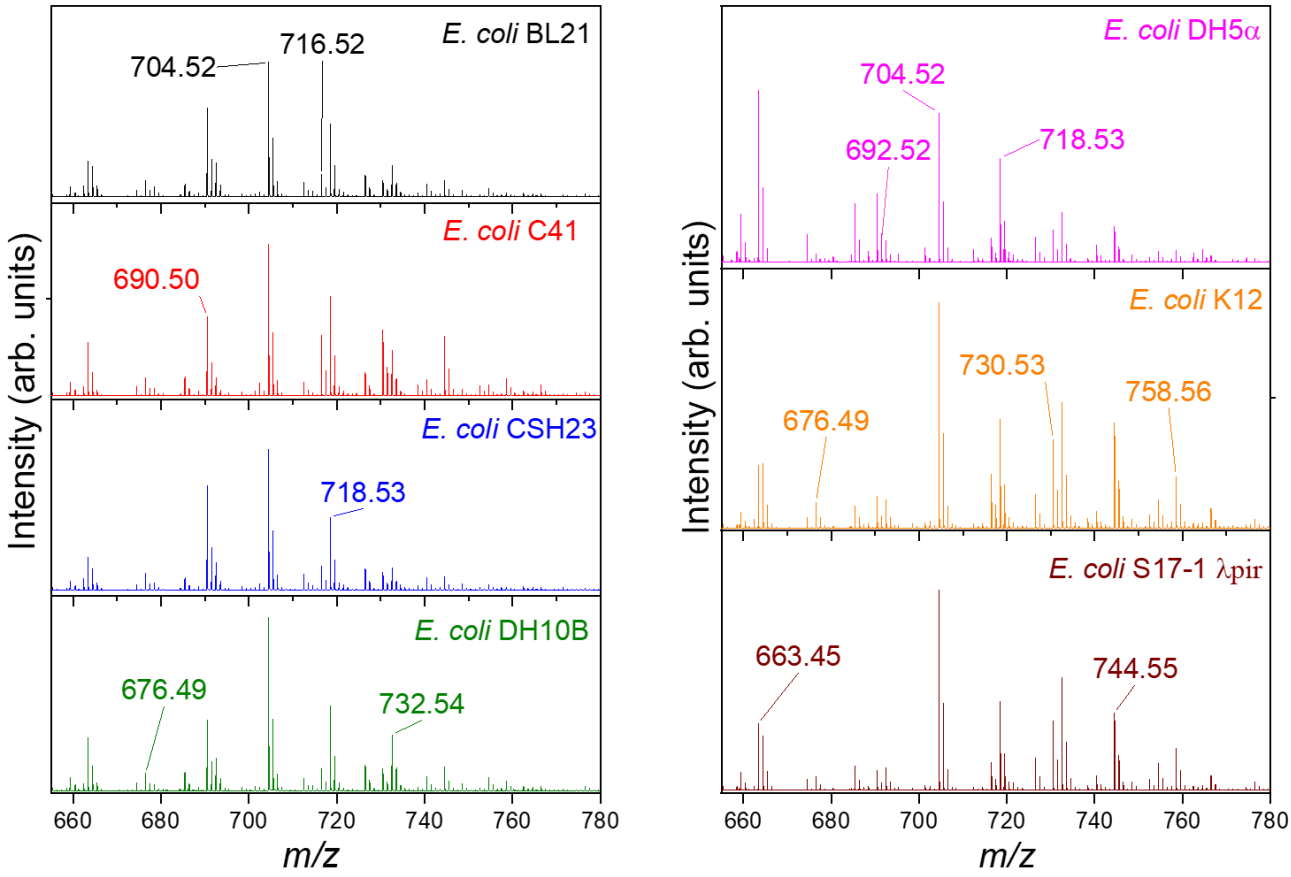

Figure 5.7. Mass spectra of the seven *E. coli* strains: BL21, C41, CSH23, DH10B, DH5α, K-12, and S17-1 λpir obtained by LC-IM-MS/MS analysis in the positive ion mode.

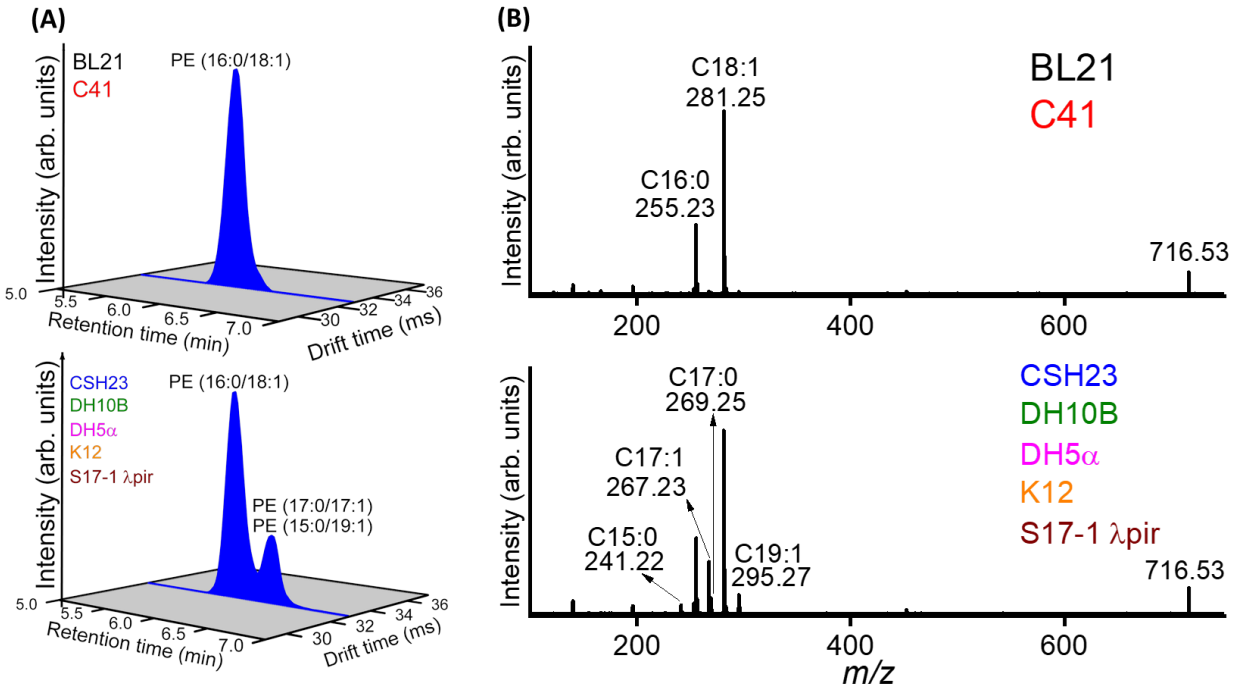

Figure 5.8. LC-IM-MS/MS spectra obtained in the negative ion mode of the seven E. coli strains where (A) liquid chromatography and ion mobility spectra revealed the presence of various lipid isomers of m/z 716.53 (PE (34:1)) and (B) Tandem mass spectra of m/z 716.53 which support the identification of the lipid isomers by the LC and IM spectra. The spectra associated with the analysis of E. coli BL21 and C41 are presented in the top panels while those associated with the analysis of E. coli CSH23, DH10B, DH5α, K12, and S17-1 λpir are presented in the bottom panels.

.

Careful examination of the drift time spectra of the *E. coli* strains reveals a single IM peak for PE (34:1) across all seven *E. coli* strains. However, LC separation revealed different isomeric forms of PE (34:1), as shown in Figure 5.8A. The number of resolved LC peaks observed for PE (34:1) across the seven strains was 1 for *E. coli* BL21 and C41 and 2 for *E. coli* CSH23, DH10B, DH5α, K12, and S17-1 λpir. Using tandem mass spectrometry, we were able to confirm the isomer types in these LC peaks based on fragmentation patterns. By examining the tandem MS analysis of *E. coli* BL21 and C41 (Figure 5.8B, top panel), the CID spectrum of the LC peak at a retention time of 5.9 min (*m/z* 716.53, PE (34:1)) shows abundant product ions at *m/z* 255.23 and 281.25

corresponding to C16:0 and C18:1, respectively. These fragment ions indicate the presence of PE (16:0/18:1). In *E. coli* CSH23, DH10B, DH5α, K12, and S17-1 λpir, the CID spectra of the LC peak at retention time 6.3 min (*m/z* 716.53, PE 34:1) (Figure 5.8B, bottom panel) reveals characteristic fragment ions at *m/z* 241.22, 267.23, 269.25, and 295.27 corresponding to carboxylate anions of C15:0, C17:1, C17:0, and C19:1, respectively. These product ions confirm the presence of PE (15:0/19:1) and PE (17:0/17:1). In addition, the presence of abundant product ions at *m/z* 255.23 and 281.25 corresponding to C16:0 and C18:1, respectively indicate the

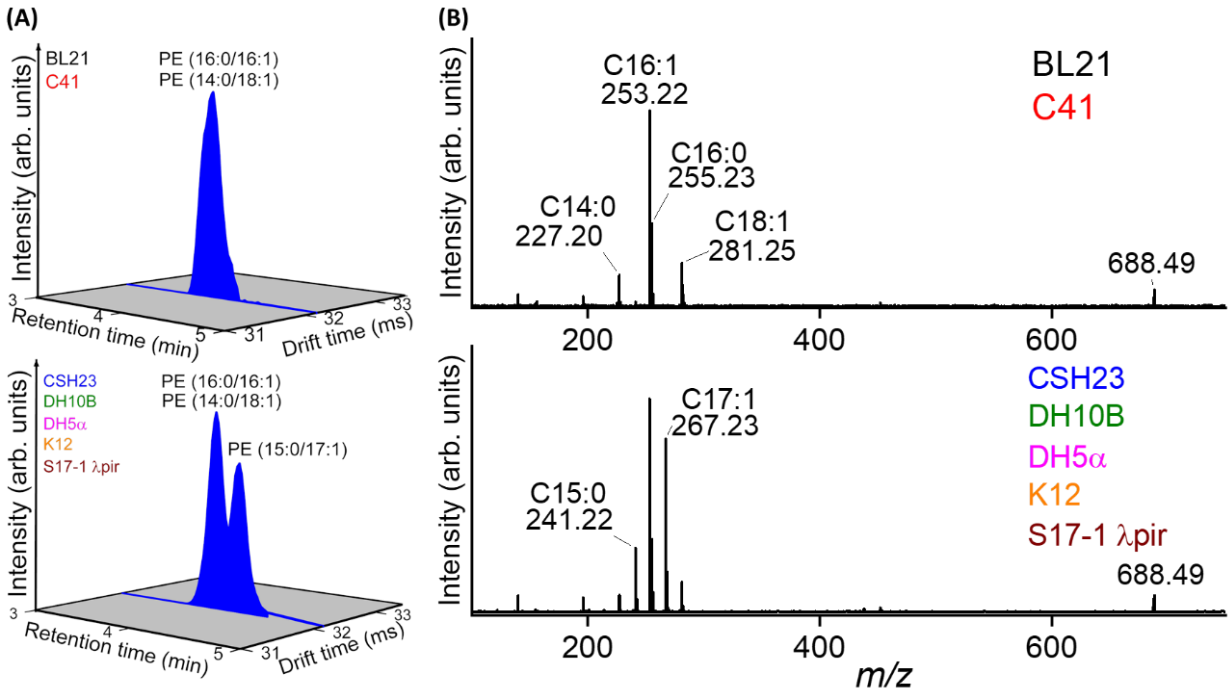

Figure 5.9. LC-IM-MS/MS spectra obtained in the negative ion mode of the seven *E. coli* strains where **(A)** liquid chromatography and ion mobility spectra revealed the presence of various lipid isomers of *m/z* 688.49 (PE (32:1)) and **(B)** Tandem mass spectra of *m/z* 688.49 which support the identification of the lipid isomers by the LC and IM spectra. The spectra associated with the analysis of *E. coli* BL21 and C41 are presented in the top panels while those associated with the analysis of *E. coli* CSH23, DH10B, DH5α, K12, and S17-1 λpir are presented in the bottom panels.

presence of PE (16:0/18:1). These results indicate that PE (16:0/18:1) was present in all the *E. coli* strains, while PE (15:0/19:1) and PE (17:0/17:1) were unique to *E. coli* CSH23, DH10B, DH5α, K12, and S17-1 λpir. Another example of discriminating lipid isomers between the *E. coli* strains is *m/z* 688.49 (PE (32:1)), which was present as PE (16:0/16:1) and PE (14:0/18:1) in all the seven *E. coli* strains, and PE (15:0/17:1) in five of the strains, as shown in Figure 5.9.

The positive ionization MS spectra of the seven *E. coli* strains also show high spectral similarity like the negative ionization mode as observed in Figure 5.7. Four positive ionization adducts $[M+H]^+$, $[M+Na]^+$, $[M+NH_4]^+$, and $[M+2Na-H]^+$ were detected across the spectra, however, the most predominant ion was the protonated $[M+H]^+$ adducts. As shown in Figure 5.7, the *m/z* at 676.49, 690.50, 692.52, 704.52, 716.52, 718.53, 730.53, 732.54, 744.55, and 758.56 were characterized as $[PE\ (31:1)+H]^+$, $[PE\ (32:1)+H]^+$, $[PE\ (32:0)+H]^+$, $[PE\ (33:1)+H]^+$, $[PE\ (34:2)+H]^+$, $[PE\ (34:1)+H]^+$, $[PE\ (35:2)+H]^+$, $[PE\ (35:1)+H]^+$, $[PE\ (36:2)+H]^+$, and $[PE\ (37:2)+H]^+$, respectively.

The identification of these lipid ions was confirmed by CID, isotopic abundances, and exact mass measurements. For example, the product ion spectrum of *m/z* 716.51 $[PE\ (34:2)+H]^+$ (Figure 5.10B) shows a base peak of *m/z* 575.51 $[M+H-141]^+$ corresponding to the neutral loss of the polar head group ($C_2H_8O_4NP$), confirming the identity of the lipid as PE. The fragment ions at *m/z* 237.22 and 265.25 correspond to C16:1 and C18:1, which are *sn*-1 and *sn*-2 fatty acids (FAs), respectively, of $[PE\ (34:2)+H]^+$, identifying the lipid as PE (16:1/18:1). The successive neutral loss of *sn*-1 (*m/z* 236) and *sn*-2 (*m/z* 264) FAs from the base peak ion (*m/z* 575.50) leads to the fragment ions at *m/z* 338.28 $(M+H-141\text{-}sn\text{-}1)^+$ and 311.26 $(M+H-141\text{-}sn\text{-}2)^+$, respectively, which further support the identification of the lipid as PE (16:1/18:1). This indicates that $[PE\ (34:2)+H]^+$ is present in all seven *E. coli* strains as PE (16:1/18:1). Careful examination of the

extracted ion chromatogram (EIC) of PE (16:1/18:1) showed a single LC peak at a retention time of 4.6 min in all seven *E. coli* strains (Figure 5.10A). However, the EIM revealed different conformers of PE (16:1/18:1), as shown in the drift spectra of the seven *E. coli* strains (Figure 5.10A). This implies that neither LC nor tandem MS can distinguish the lipid conformers revealed by IM since PE (16:1/18:1) has a single LC peak and the same fragmentation pattern in all seven *E. coli* strains (Figure 5.11).

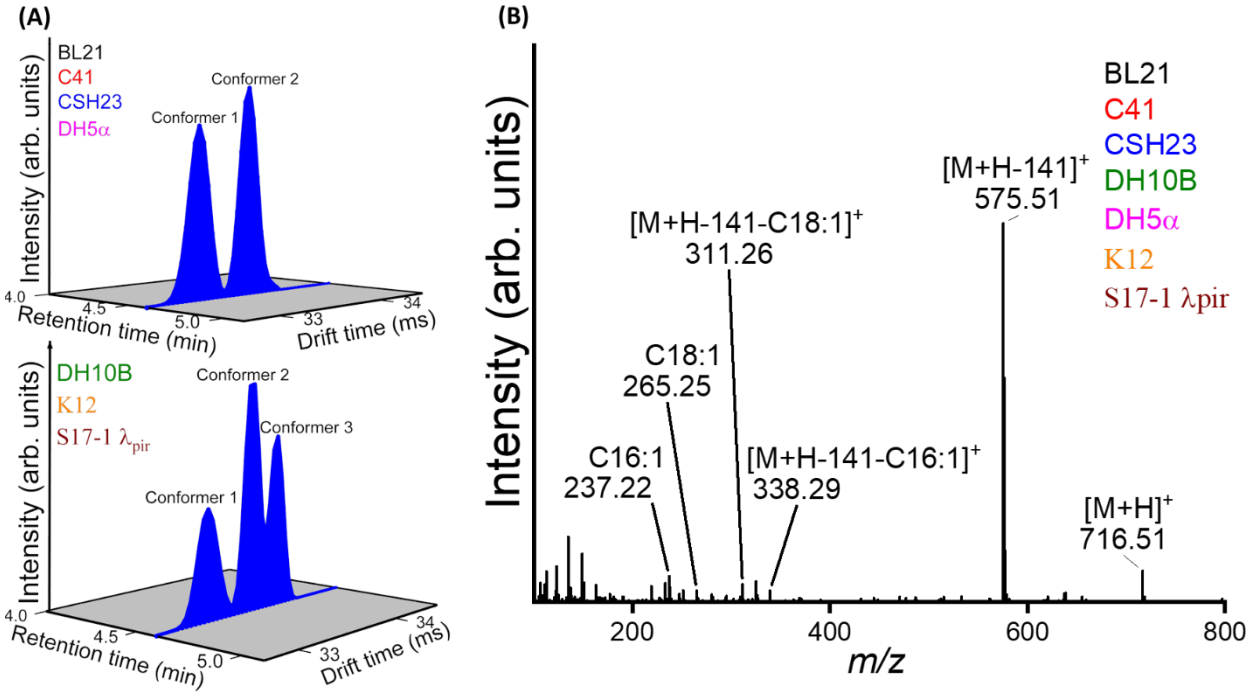

Figure 5.10. LC-IM-MS/MS spectra obtained in the positive ion mode of the seven E. coli strains where (A) liquid chromatography and ion mobility revealed the presence of various lipid conformers of m/z 716.51 (PE (34:2). The spectra associated with the analysis of E. coli BL21, C41, CSH23, and DH5α are presented in the top panel while those associated with the analysis of E. coli DH10B, K12, and S17-1 λpir are presented in the bottom panel. (B) Tandem mass spectra of m/z 716.50 $[PE (34:2)+H]^+$.

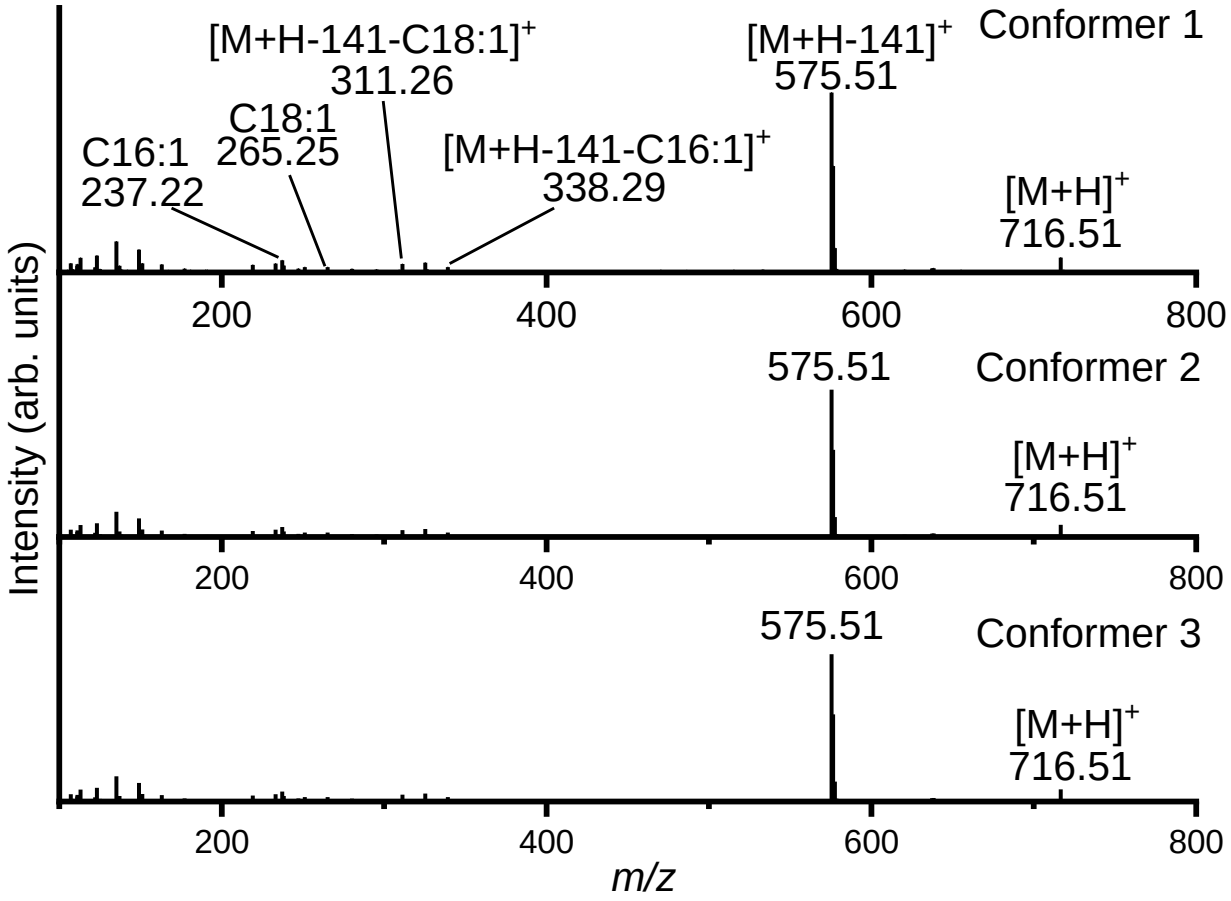

Figure 5.11. Tandem mass spectra of *m/z* 716.51 [PE (34:2) + H]$^+$ as conformers 1, 2, and 3

Using single-field CCS measurement, we measured the IM protonated peaks of PE (16:1/18:1) at 33.17, 33.57, and 33.82 ms, as shown in Figure 5.10A, yielding CCS values of 271.1, 273.9, and 275.6 Å^2, respectively. Remarkably, these experimental CCS values showed good agreement (less than 1% difference) with the theoretical values obtained by the Lipid CCS predictor (273.2 Å^2). Of the three conformers of PE (16:1/18:1) detected, two conformers (conformers 1 and 2 (IM peaks at 33.17 and 33.57 ms) are present in all seven *E. coli* strains, while the conformer with the IM peak at 33.83 ms (conformer 3) is present in only three of the *E. coli* strains (DH10B, K12, and S17-1 λpir). PE (18:1/18:1) like PE (16:1/18:1), has a single LC peak and the same product ion spectrum in all the *E. coli* strains, as shown in Figure 5.12, but exist

as three different conformers in BL21, C41, and DH10B strains. This shows that lipid conformers revealed by IM analysis can be used to distinguish the *E. coli* strains. Moreover, these results demonstrate that multidimensional techniques such as LC-IM-MS/MS provide high selectivity and discriminatory power for accurate discrimination of bacteria strains.

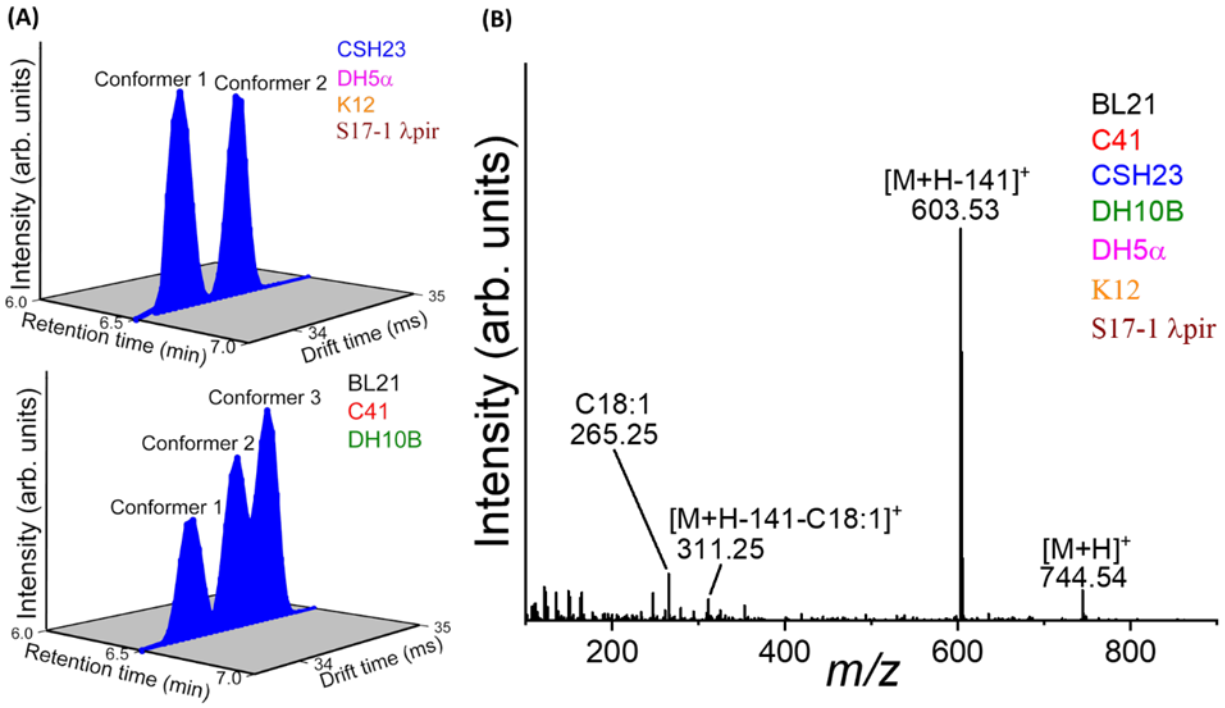

Figure 5.12. LC-IM-MS/MS spectra obtained in the positive ion mode of the seven *E. coli* strains where **(A)** liquid chromatography and ion mobility revealed the presence of various conformers of *m/z* 744.54 (PE (36:2)). **(B)** Tandem mass spectra of *m/z* 744.54 $[PE\ (36:2)+H]^+$.

5.3.4. Discrimination of *E. coli* strains by paper spray–IM–MS/MS

Although the LC-IM-MS/MS could accurately distinguish the seven *E. coli* strains, this method is labor-intensive and time-consuming, primarily because of the extensive sample preparation and long LC acquisition times. Therefore, alternative techniques with minimal sample preparation and rapid analysis are needed as early detection of bacteria allows quick clinical intervention. For this purpose, we used paper spray (PS)-IM-MS/MS, in which the bacterial culture was filtered through a glass filter paper, and after applying spray voltage and solvent, the IM and

tandem MS spectra of the seven *E. coli* strains were recorded in both ionization modes . In the negative ionization mode, the deprotonated $[M-H]^-$ adduct of lipid isomers in the seven *E. coli* strains was characterized by CCS and exact mass measurements. For instance, *m/z* 733.51 in Figure 5.13 was characterized as PG (33:1) because the experimental CCS value, 268.1 $Å^2$, shows good agreement (less than 2% difference) with the theoretical CCS value, 265.6 $Å^2$ (Table 5.8). Interestingly, careful examination of the EIM of the $[PG (33:1)-H]^-$ across the seven *E. coli* strains revealed a single IM peak at the drift time of 35.04 ms (Figure 5.13A). However, its CID spectrum showed several characteristic fragment ions that can serve as diagnostics biomarkers for distinguishing the seven *E. coli* strains (Figure 5.13B). The fragment ions at *m/z* 255.23 and 267.23 in the CID spectrum of $[PG (33:1)-H]^-$ in *E. coli* BL21, C41, DH10B, and DH5α correspond to C16:0 and C17:1, respectively. The additional product ions at *m/z* 241.22, 253.22, 269.24, and 281.25 in *E. coli* CSH23, K12, and S17-1 λpir correspond to C15:0, C16:1, C17:0, and C18:1, respectively. This result indicates that PG (16:0/17:1) is present in all seven *E.*

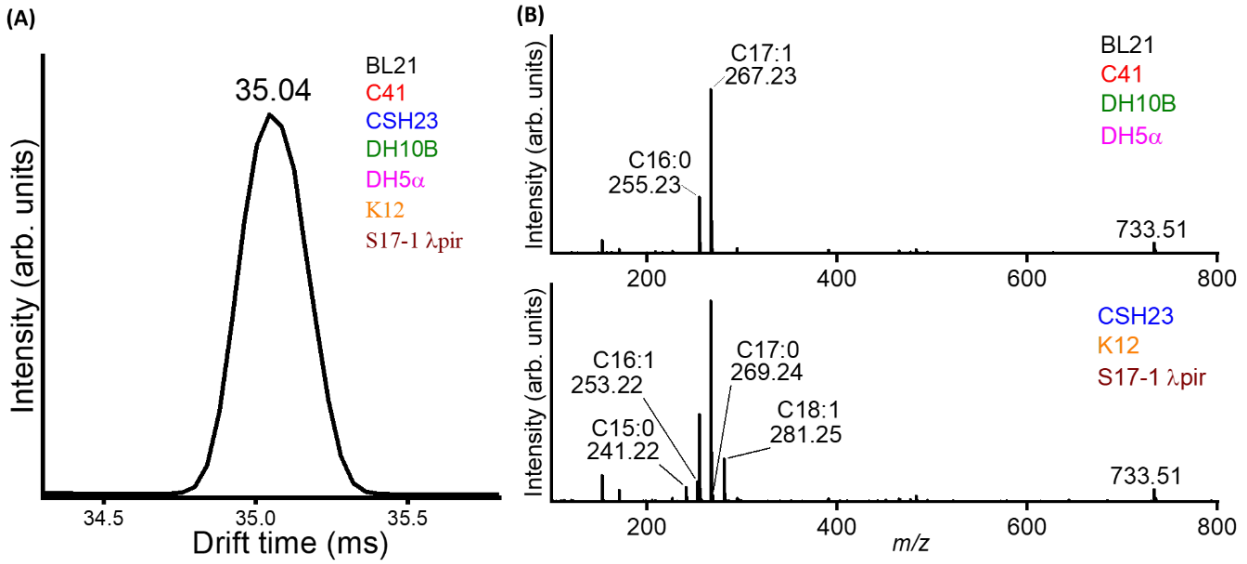

Figure 5.13. PS-IM-MS/MS spectra obtained in the negative ion mode of the seven *E. coli* strains. **(A)** ion mobility spectrum of the *m/z* 733.51 (PG (33:1)) and **(B)** Tandem mass spectra (MS/MS) of *m/z* 733.51which revealed the presence of various isomers of PG (33:1).

coli strains, while PG (15:0/18:1) and PG (16:1/17:0) are present only in three of the *E. coli* strains (CSH23, K12, and S17-1 λpir).

In the positive ionization mode, IM effectively separates diagnostic lipid conformers indistinguishable by tandem mass spectrometry. For example, *m/z* 726.51, characterized as $[PE(33:1)+Na]^+$, has multiple IM peaks in the drift spectra of the seven *E. coli* strains (Figure 5.14A). Meanwhile, its CID spectrum is similar in all seven *E. coli* strains (Figure 5.14B). The product ion scan of *m/z* 726.51 $[PE(33:1)+Na]^+$ in the *E. coli* strains shows a characteristic ion at *m/z* 164.00 $([C_2H_8O_4NP]+Na)^+$ corresponding to the polar head group, ethanolamine, confirming the identity of the lipid as PE. The neutral loss of the polar head group leads to the fragment ions at *m/z* 563.50 $[M+H-141]^+$ and 585.49 $[M+Na-141]^+$ corresponding to a proton and sodium attached to the diglyceride-like ion. The product ions at *m/z* 239.24 and 251.25 correspond to C16:0 and C17:1, which represent the *sn*-1 and *sn*-2 FAs of the $[PE(33:1)+Na]^+$, respectively, and accurately characterize the lipid as PE (16:0/17:1).

However, the IM dimension revealed different conformers of $[PE(33:1)+Na]^+$, which can serve as fingerprints to distinguish the seven *E. coli* strains. The two conformers of $[PE(33:1)+Na]^+$ at drift time of 34.61 and 35.13 ms (conformers 1 and 2), as shown in Figure 5.14A, have CCS values of 273.0 and 275.8 $Å^2$, respectively, showing good agreement (less than 1% difference) with the theoretical CCS value of 274.1 $Å^2$. Of the two conformers of PE(16:0/17:1) detected, the IM peak at 35.13 ms (conformer 1) is present in all seven *E. coli* strains, whereas the conformer at the IM peak of 34.61 ms (conformer 2) is present in only two of the *E. coli* strains (K12 and S17-1 λpir). The complementary separation of IM and tandem MS was effectively used to reveal lipid isomers and conformers that serve as diagnostic biomarkers to distinguish *E. coli* strains, while the paper spray was used to rapidly analyze each bacteria strain

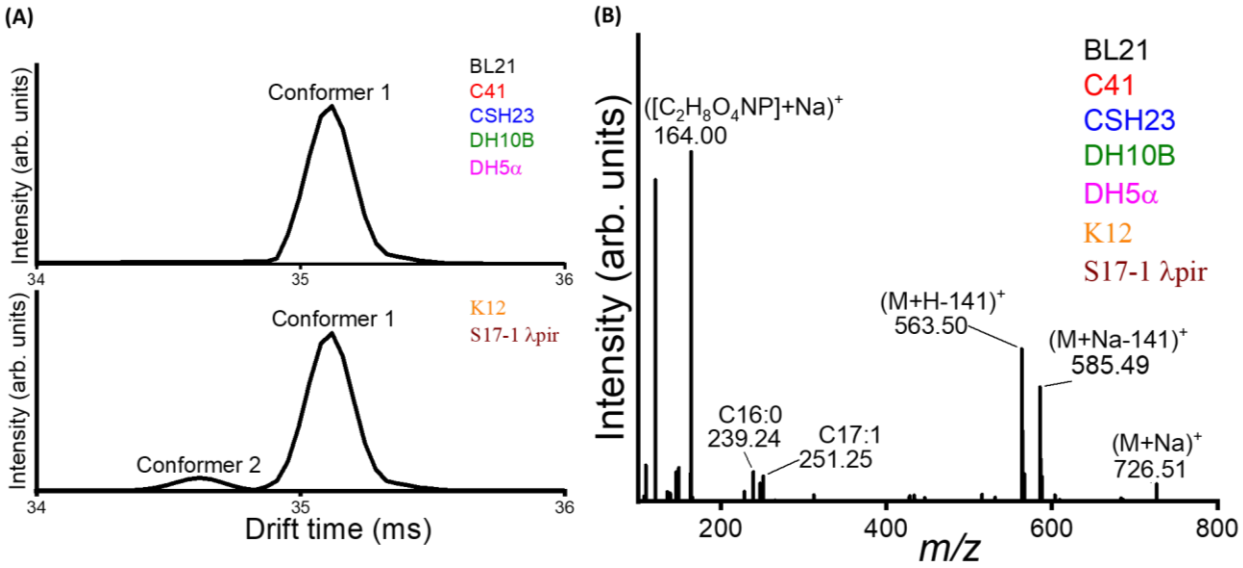

Figure 5.14. PS-IM-MS/MS spectra obtained in the positive ion mode of the seven *E. coli* strains where **(A)** Ion mobility spectra revealed the presence of various lipid conformers of *m/z* 726.51 ([PE (33:1)+Na]$^+$) and **(B)** Tandem mass spectra of *m/z* 726.51 ([PE (33:1)+Na]$^+$).

in less than 2 minutes. These findings demonstrate PS-IM-MS/MS can act as an effective analytical technique to provide rapid detection and accurate discrimination of bacteria strains.

5.3.5. Multivariate statistics

Integration of two orthogonal separation methods (LC and IM) with tandem mass analysis, as demonstrated in our bacterial strain discrimination, allowed multidimensional complementary separation, and increased peak capacity. Isomeric lipid biomarkers discriminating *E. coli* strains were resolved in at least one separation dimension. Therefore, using multivariate statistical analysis, spectral information from LC, IM, and MS/MS was used to reveal biochemical differences and group *E. coli* strains based on their corresponding spectral fingerprints. The high selectivity of LC-IM-MS/MS is reflected in the PCA score plots, which show a clear separation between the seven *E. coli* strains in negative and positive ion modes (Figure 5.15A and Figure

5.15B, respectively). Quantification of separation using LDA resulted in 96.1% and 100% prediction rates in the negative and positive ion modes, respectively, as shown in the CV confusion matrix (Table 5.5), which shows a high classification rate of the strains. These rates show that the multidimensional LC-IM-MS/MS is very effective in discriminating closely related bacteria strains. As depicted in Figure 5.15A and Figure 5.15B, two and three clusters were observed along the PC1 axis of the negative and PC3 axis of the positive ion data, respectively. One of the clusters in both modes contains DH10B, DH5α, K12, and S17-1 λpir indicating biochemical similarity between these strains. In the positive ion data, as shown in Figure 5.15B, BL21 and C41 appeared separated by the cluster group (DH10B, DH5α, K12, and S17-1 λpir), suggesting that they share several lipid conformation biomarkers with the other strains.

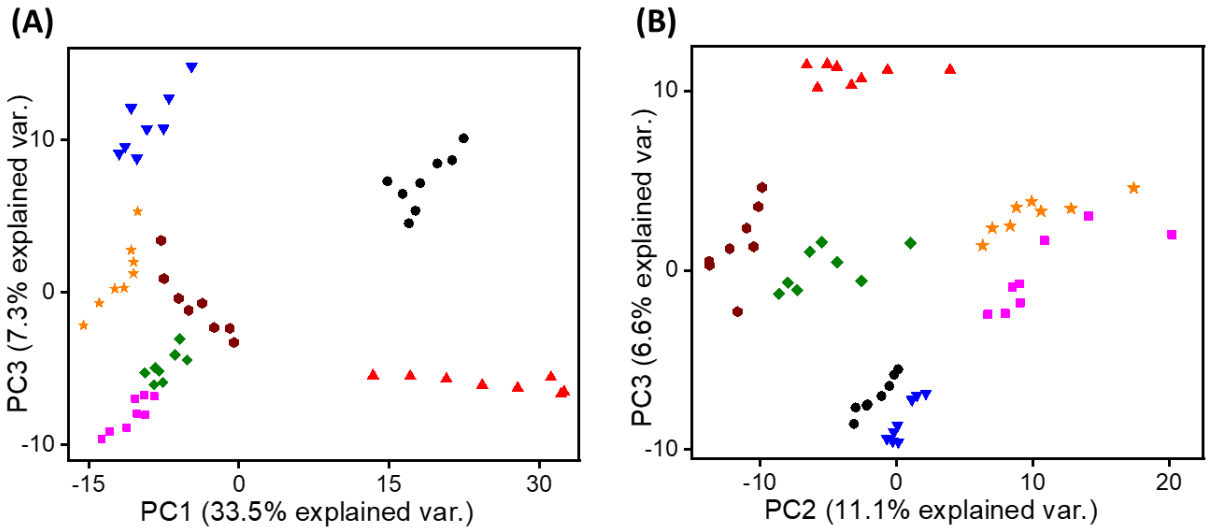

Figure 5.15. PCA plots of the seven *E. coli* strains in the (A) negative and (B) positive ion modes of the LC-IM-MS/MS method. The *E. coli* strains are indicated by color and shape as follows: BL21 (Black circles), C41(Red triangles pointing up), CSH23 (Blue triangles pointing down), DH10B (Green diamonds), DH5α (Magenta squares), K12 (Orange stars), and S17-1 λpir (Wine hexagons).

To theoretically investigate the genomic relatedness of the *E. coli* strains, we used genome assemblies of the strains for comparative genome analysis. The genome assemblies of six strains

(BL21, C41, DH10B, DH5α, K-12, and S17-1 λpir) available in the NCBI reference sequence database [173] were downloaded and compared for genetic variability by counting the single nucleotide polymorphisms (SNPs) between the strains using the CSIPhylogeny webtool [174]. SNP calling was performed with default settings, using the *E. coli* K12 strain as a reference. The result shows the highest variation between strains K12 and C41, followed by strains K12 and BL21 based on the SNP count between strains (Table 5.9). Interestingly, the variation in SNP counts between strains DH10B, DH5α, K12, and S17-1 λpir, is lower, indicating the high genetic similarity of these four *E. coli* strains. Comparative genomic analysis shows good agreement with our experimental findings, as DH10B, DH5α, K12, and S17-1 λpir clustered in the PCA score plot in both ion modes (Figure 5.15A and B), and with less variation in SNP number. However, the proximity of these four strains to each other differs in the negative and positive ion modes. BL21 and C41 appear to have high SNP counts based on comparative genomic analysis. The bulk of our experimental analysis is supported by comparative genome analysis. Therefore, our results show that multidimensional LC-IM-MS/MS is a highly selective and sensitive discrimination technique for bacterial strains.

Table 5.9. Comparative genome analysis of the *E. coli* strains.

	DH10B	S17-1 λpir	DH5α	BL21	C41	Reference (K12)
DH10B	0	704	304	15268	40169	102
S17-1 λpir	704	0	829	14994	40377	625
DH5α	304	829	0	15432	40314	240
BL21	15268	14994	15432	0	43701	15216
C41	40169	40377	40314	43701	0	40099
Reference (K12)	102	625	240	15216	40099	0

The PS-IM-MS/MS rapidly discriminates the seven *E. coli* strains with a prediction rate of 62.5% and 73.5% in the negative and positive ion modes, respectively, as quantified by LDA. The

negative ion mode PCA score plot shows a clear separation between BL21, C41, and K12 highlighting the high genomic disparities between these strains as shown in Figure 5.16.

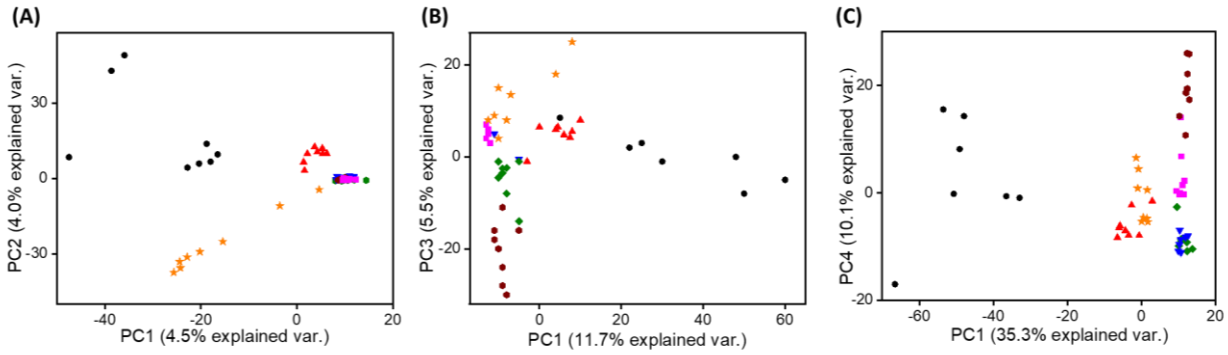

Figure 5.16. PCA plots of the seven *E. coli* strains in the **(A)** negative ion mode and **(B)** positive ion mode of the PS-IM-MS/MS method. (C) Data fusion of the extracted PCs of the negative and positive ion modes of the PS-IM-MS/MS. The *E. coli* strains are indicated by color and shape as follows: BL21 (Black circles), C41(Red triangles pointing up), CSH23 (Blue triangles pointing down), DH10B (Green diamonds), DH5α (Magenta squares), K12 (Orange stars), and S17-1 λpir (Wine hexagons).

CSH23, DH10B, DH5α, and S17-1 λpir appear unseparated in the negative PCA score plot, however, the positive mode PCA plot showed improved separation of these four strains along the PC3 axis (Figure 5.16B). The separation along the PC1 axis of the positive mode of the PS-IM-MS/MS indicates that DH10B, DH5α, K12, and S17-1 λpir, are highly genetically similar to one another in comparison to BL21 and C41 as confirmed by the LC-IM-MS/MS PCA score plots and the comparative genome analysis. The low predictive ability of the PS-IM-MS/MS in comparison

to LC-IM-MS/MS can be attributed to the ionization suppression from matrix effects [175], and the absence of chromatographic separation.

Previous studies have demonstrated that fusing the chemical information present in the negative ion mode with that of the positive ion mode can increase classification rates [53]. The fusion of the extracted PCs from the negative and positive ion data increased the separation among the seven *E. coli* strains, as visible in the PC1 versus PC4 score plot (Figure 5.16C). Indeed, the prediction rates significantly increased to 80.5% as quantified through LDA. These results illustrate the capabilities of PS-IM-MS/MS as a rapid, highly selective, and sensitive discrimination technique for bacterial strains.

5.4. Conclusions

This work demonstrates successful strain-level discrimination of bacteria using LC-IM-MS/MS and PS-IM-MS/MS. The complementary separations from the multidimensional LC-IM-MS/MS were used to reveal acyl chain lipid isomers and conformers in lipid standards, *E. coli* lipid extract, and strains. Prediction rates of 96.1% and 100% were achieved with LC-IM-MS/MS in negative and positive ion modes, respectively, highlighting the high accuracy and selectivity of the LC-IM-MS/MS method. Tandem MS and LC separation proved effective in discriminating lipid isomers in the negative ionization mode, while IM separation was more effective in resolving lipid conformational biomarkers in the positive ionization mode. Due to the clinical importance of early detection for rapid medical intervention, a faster technique, PS-IM-MS/MS, was used to discriminate *E. coli* strains with a prediction rate of 80.5% after the fusion of the negative and positive ion data. Lipid isomers and conformers were detected, which served as strain-indicating biomarkers.

Chapter 6. Conclusions and Future Outlooks

6.1. Conclusions

Determining bacterial identity is crucial to clinical diagnostics, environmental monitoring, food safety surveillance, and public health concerns. Millions of hospitalizations and thousands of deaths are reported annually according to CDC because of foodborne illnesses, Urinary tract infections, waterborne illnesses, etc. If this issue is left unaddressed, 10 million deaths per year would be reported by 2050 mainly due to antimicrobial resistance. Towards providing rapid and accurate diagnostics to reduce hospitalizations, deaths, and antimicrobial resistance, we developed paper spray – ion mobility – tandem mass spectrometry (PS – IM – MS/MS) technique. Bacterial infections diagnosis depends on the microbial biomarkers for accurate detection, however, these biomarkers which can be metabolites, lipids, peptides, etc., are structurally diverse, having several forms of isomerism which require a highly selective analytical technique for accurate separation. We utilized the PS – IM – MS/MS to differentiate two constitutional isomers rapidly and accurately; propazine and terbuthylazine and two geometric isomers; *cis* and *trans* isomers. Sample introduction using the paper spray and data acquisition which include both drift time and MS/MS were accomplished in less than a minute for each run. The PS – IM – MS/MS proves to be highly effective for separating isomeric compounds in a timely manner, hence, we used the method to differentiate five *Bacillus* species through isomeric biomarker discovery. The five *Bacillus* species were accurately distinguished within 4 hours of incubation time. Using only the PS – MS/MS information, we obtained a prediction rate of 92.4% and 97.6% in the negative and positive ion information, respectively. Upon including the IM separation dimension data into the PS – MS/MS workflow, the prediction rates increased significantly in negative and positive ion

mode from 92.4% and 97.6% to 99.7% and 100.0%, respectively. We associated the increased prediction rates to the capability of IM to provide a clear separation between the diagnostic isomers leading to an enhanced species' identification.

Upon successful species' discrimination of the *Bacillus* microorganisms, we challenged the PS – IM – MS/MS method for strain level differentiation. Using the PS – IM – MS/MS method, we achieved the prediction rates of 62.5% and 73.5% respectively for negative and positive ion modes. Furthermore, the strategy of numerical data fusion of negative and positive ion data increased the classification rates of PS - IM - MS/MS to 80.5%. These rates were not considered high enough for accurate discrimination as clear separation and unequivocal identification is needed for bacterial disease diagnosis. Hence, liquid chromatography instead of paper spray was interfaced with ion mobility and tandem mass spectrometry for the strain level discrimination of *E. coli* strains. Prediction rates of 96.1% and 100% were achieved with LC – IM – MS/MS in negative and positive ion modes, respectively, highlighting the high accuracy and selectively of the LC – IM – MS/MS method. These high prediction rates from the multidimensional LC – IM – MS/MS demonstrates the capability of the method for not only strain discrimination but also for more challenging discrimination such as antibiotics resistant bacteria versus non-resistant bacteria, pathogenic bacteria strains against non-pathogenic strains and so much more.

6.2. Future Outlooks

The genetic similarities of bacteria increase from species to strains to serotypes, highlighting the need for highly selective and sensitive analytical techniques and approaches. For instance, the chromosome size of *E. coli* O157:H7 is 5.5 Mb, it contains a 4.1 Mb backbone sequence that is conserved in all *E. coli* strains, emphasizing the high genetic similarity of these

strains. While the research work in this dissertation has achieved species and strain discrimination, it is highly recommended that different types of strains and serotypes differentiation should be investigated for the main purpose of improving bacterial identity, reducing hospitalization times and number of deaths, and reducing antimicrobial resistance. Some of the future research that should be conducted to improve the rapid and accurate discrimination of bacteria are listed below.

6.2.1. Pathogenic and Non-pathogenic Strain Discrimination

Most *E. coli* strains colonize the gastrointestinal tract of humans and animals harmlessly as normal flora. However, there are some strains that have evolved into pathogenic *E. coli* through the acquisition of virulence factors via plasmids, transposons, bacteriophages and/or pathogenicity islands [176]. This pathogenic *E. coli* can be categorized based on serogroups, pathogenicity mechanisms, clinical symptoms or virulence factors [176]. Serotyping of pathogenic *E. coli* based on their surface antigen profiles includes O (somatic), H (flagellar) and K (capsular) [177]. Some studies suggest that 20 to 50% of all enterohemorrhagic (EHEC) infections are caused by non-O157 serotypes, which appear to be less virulent than the O157 serotypes [177]. The most common non-O157 serotypes associated with human disease include O26:H11, O103:H2, O111NM and O113:H21 [176]. The similarity of their genetic make-up and the thousands of diseases caused in humans require a highly selective and sensitive method to distinguish them. When differentiating between the various strains based on their pathogenicity, one of the many objectives should be the detection of target genes encoding virulence factors or the detection of target metabolites, peptides and lipids that are expressions of the target genes.

6.2.2. Antibiotic-resistance and non-resistance bacteria strain discrimination

In recent years, the emergence of antibiotic-resistant bacteria has become a global problem. One of the main drivers for the emergence of antibiotic-resistant bacteria is the excessive or

inappropriate use of antibiotics [178]. In some cases, these antibiotic-resistant bacteria have remarkable ability to acquire resistance to multiple antibiotics [179]. The emergence of penicillin-resistant *Staphylococcus aureus* (*S. aureus*) was reported within 2 years of the introduction of penicillin [180]. Methicillin-resistant *S. aureus* (MRSA) was first reported in 1961, shortly after the semisynthetic antibiotic methicillin was first introduced [181]. MRSA is a significant clinical threat with high morbidity and mortality, much higher than those of methicillin-susceptible *S. aureus* (MSSA) [179]. Hence, a rapid and highly accurate diagnostic method needs to be urgently developed for distinguishing not only MSSA and MRSA but also other resistant bacteria from non-resistant bacteria. The method should be highly sensitive such that the bacteria can be detected without culturing and highly selective such that the discrimination is not affected by environmental or other factors.

6.2.3. Influence of Growth Condition and Media on Bacterial Identity

One of the achieved objectives in this dissertation is the detection of microbials at early incubation time (4 hours) with the utmost objective of detecting bacteria without the requirement for culturing [182]. We compared the mass spectra obtained from PS – MS analysis of bacteria cultured for 4, 8, 12, and 16 hours and found that the same ions were detected irrespective of the culturing time [182]. We concluded that the progression of the culture through its growth cycle may be responsible for the observed spectral variation in the relative intensities of biomarkers, while the overall qualitative differences in the MS spectra may be due to the ionization phenomenon and bacterial metabolism at the time of sampling [183, 184]. Previous studies have reported that MS spectral variability due to culture time and conditions does not affect bacterial identification by mass spectrometry [183]. However, these previous studies were all conducted for species-level identification and discrimination using MALDI-MS which utilizes mainly ribosomal

proteins for identification [179, 183]. Hence further investigation should be conducted to evaluate the influence of culturing time, media, and sample preparation on the discrimination of bacteria strains using ambient ionization ion mobility mass spectrometry techniques such as PS – IM – MS/MS.

6.3. Recommended Strategies for improving bacterial detection and discrimination

Accurate identification and discrimination of bacterial strains and serotypes is highly dependent on the selectivity of the analytical techniques and methodology used. Some of the recommended approaches for improving bacterial detection and discrimination at the strains and serotypes levels that will enhance clinical diagnostics and improve food safety, etc. are discussed below;

6.3.1. Whole organisms' fingerprint

Bacterial species and strains have been successfully detected and differentiated using lipids [77], peptides [7], metabolites [185], proteins [186], and so on. The gold standard method for bacteria strain detection is Pulse Field Gel Electrophoresis (PFGE) which is a powerful genotyping technique used for the separation of large DNA molecules (entire genomic DNA), however, it is time consuming and expensive [8, 187]. While MALDI-MS is the method of choice for bacterial identification at clinical microbiology laboratories largely due to its robust analysis as it largely measures the ribosomes, which are always present irrespective of how the bacteria are cultures, its discriminatory power remains questionable at the strain level [8, 77]. A multidimensional PS – IM – MS/MS and LC – IM – MS/MS has been utilized to accurately discriminate seven *E. coli* strains based on the organisms lipidomic profiles [77], however, it would be expected that the discriminatory power of these techniques would decrease as the number of bacteria strains increase. Hence, an all-omics approach would be considered a significant solution as it would

provide a holistic view of the molecules making up an organism. The approach would be primarily aimed at the global detection of genes (genomics), mRNAs (transcriptomics), proteins (proteomics), lipids (lipidomic) and metabolites (metabolomics) in a biological sample. Towards all omics approach for accurate bacteria strain discrimination, we are using peptides, lipids, and metabolites to differentiate six non-pathogenic and five pathogenic *E. coli* strains as a proof of concept for all-omics approach to provide accurate discrimination of bacteria strains and serotypes [188].

6.3.2. Machine Learning

Advances in technology and computing power have made machine learning methods more accessible, especially through open-source computing languages such as Python [189], R [190], and Julia [191]. This has led to a sharp increase in the successful application of machine learning to problems in the field of bioinformatics. Machine learning has been applied to the identification of microorganisms [192] and the diagnosis of ovarian cancer among others [193]. Random forest classification (RFC), k-nearest neighbor (KNN), multilayer perceptron (MLP) and convolution neural network (CNN) are examples of classifiers that extract the most informative features for accurate classification [194]. Machine learning can be used in combination with different analytical techniques to develop biomarkers for the detection and differentiation of bacterial strains and serotypes. The unique list of metabolites, lipids, peptides, and other significant biomarkers discovered by the machine learning can then be used to detect a specific bacterial strain in an unknown biological sample.

6.3.3. High-Resolution Ion Mobility Instrument

The standard resolution (R_p) of Agilent 6560 IM-QTOF used in this dissertation is ~ 60 which begins to resolve peaks at ~2% difference in drift times or CCS values [77, 93]. With the

introduction of the HRdm technique, the accessible resolution of the DTIMS is extended to ~ 180 to 250 which increases its isomer separation capability up to the sub-1% range [77, 93]. Isomers including acyl-chain, sn-positional, double-bond positional, geometric, and constitutional isomers have <1% drift time difference [195]. Some of these isomers have been found to be present in *E. coli* strains and would not be resolved by the traditional DTIMS (R_p, ~60) [77]. With the introduction of the HRdm technique, we could resolve some lipid isomers and conformers which proved to be effective biomarkers for the discrimination of seven non-pathogenic *E. coli* strains [77]. However, acyl chain lipids isomers annotated by the tandem MS dimension were inseparable in the IM dimension even with the utilization of the HRdm technique [77]. This implies that a higher resolution IM instrument such as structure for lossless ion manipulations (SLIM, separation power ~ 1860) is needed to provide better separation of isomers than the current technology (HRdm) used in this dissertation [196, 197]. Using IM platforms with higher resolution will allow the identification of more biomarkers, which in turn will lead to the discrimination of wide sets of microorganisms.

6.3.4. Portable and Standalone Ion Mobility instrument

Rapid diagnostic tests (RDTs) are increasingly used in clinical practice to provide actionable information for patient care in a timely manner, ideally at the time and location of the patient's interaction with health care system. RDT (often referred to as point-of-care tests (POCT) when deployed near-patient) are often simple to use and therefore can offer diagnostic support in resource-limited settings or away from more sophisticated diagnostic laboratory support, for example in primary care. The long-term goal of this project is to develop a portable and standalone IM instruments capable of providing rapid diagnostics tests for a wide variety of infectious diseases such that it can be easily used by nurses at the hospital, or by individuals at home, etc.

Towards this goal, the development of these devices should incorporate whole organisms fingerprinting, machine learning, and high-resolution IM capabilities to provide accurate and rapid detection and discrimination of various types of infectious diseases. In addition, it should be cost effective and easily used by all individuals regardless of their education levels.

References

[1] S.V. Lynch, O. Pedersen, The human intestinal microbiome in health and disease, New England Journal of Medicine, 375 (2016) 2369-2379.
[2] C. Deusenbery, Y.Y. Wang, A. Shukla, Recent Innovations in Bacterial Infection Detection and Treatment, Acs Infect Dis, 7 (2021) 695-720.
[3] L. Cole, P.R. Kramer, Bacteria, virus, fungi, and infectious diseases, Human Physiology, Biochemistry and Basic Medicine, (2016) 193.
[4] T.P. Lodise, M. Nowak, M. Rodriguez, The 30-Day Economic Burden of Newly Diagnosed Complicated Urinary Tract Infections in Medicare Fee-for-Service Patients Who Resided in the Community, Antibiotics, 11 (2022) 578.
[5] S.P. Oliver, B.M. Jayarao, R.A. Almeida, Foodborne pathogens in milk and the dairy farm environment: food safety and public health implications, Foodbourne Pathogens & Disease, 2 (2005) 115-129.
[6] J.W.-F. Law, N.-S. Ab Mutalib, K.-G. Chan, L.-H. Lee, Rapid methods for the detection of foodborne bacterial pathogens: principles, applications, advantages and limitations, Frontiers in microbiology, 5 (2015) 770.
[7] F. Roux-Dalvai, C. Gotti, M. Leclercq, M.-C. Hélie, M. Boissinot, T.N. Arrey, C. Dauly, F. Fournier, I. Kelly, J. Marcoux, Fast and Accurate Bacterial Species Identification in Urine Specimens Using LC-MS/MS Mass Spectrometry and Machine Learning*[S], Molecular & cellular proteomics, 18 (2019) 2492-2505.
[8] N. AlMasoud, H. Muhamadali, M. Chisanga, H. AlRabiah, C.A. Lima, R. Goodacre, Discrimination of bacteria using whole organism fingerprinting: the utility of modern physicochemical techniques for bacterial typing, Analyst, 146 (2021) 770-788.
[9] J. Shafrin, A. Marijam, A.V. Joshi, F.S. Mitrani-Gold, K. Everson, R. Tuly, P. Rosenquist, M. Gillam, M.E. Ruiz, Economic burden of antibiotic-not-susceptible isolates in uncomplicated urinary tract infection: Analysis of a US integrated delivery network database, Antimicrobial Resistance & Infection Control, 11 (2022) 84.
[10] P.K. Mandal, A. Biswas, K. Choi, U. Pal, Methods for rapid detection of foodborne pathogens: an overview, American Journal of Food Technology, 6 (2011) 87-102.
[11] X. Zhao, C.-W. Lin, J. Wang, D.H. Oh, Advances in rapid detection methods for foodborne pathogens, (2014).
[12] S.S. Buehler, B. Madison, S.R. Snyder, J.H. Derzon, N.E. Cornish, M.A. Saubolle, A.S. Weissfeld, M.P. Weinstein, E.B. Liebow, D.M. Wolk, Effectiveness of practices to increase timeliness of providing targeted therapy for inpatients with bloodstream infections: a laboratory medicine best practices systematic review and meta-analysis, Clinical microbiology reviews, 29 (2016) 59-103.
[13] M.H. Kollef, Broad-spectrum antimicrobials and the treatment of serious bacterial infections: getting it right up front, Clinical Infectious Diseases, 47 (2008) S3-S13.
[14] W.H. Organization, Antimicrobial resistance: global report on surveillance, World Health Organization, 2014.

[15] S.C. Davies, T. Fowler, J. Watson, D.M. Livermore, D. Walker, Annual Report of the Chief Medical Officer: infection and the rise of antimicrobial resistance, The Lancet, 381 (2013) 1606-1609.
[16] W. Adamus-Białek, A. Baraniak, M. Wawszczak, S. Głuszek, B. Gad, K. Wróbel, P. Bator, M. Majchrzak, P. Parniewski, The genetic background of antibiotic resistance among clinical uropathogenic Escherichia coli strains, Molecular biology reports, 45 (2018) 1055-1065.
[17] S. Leekha, C.L. Terrell, R.S. Edson, General principles of antimicrobial therapy, in: Mayo clinic proceedings, Elsevier, 2011, pp. 156-167.
[18] N. Lee, K.Y. Kwon, S.K. Oh, H.-J. Chang, H.S. Chun, S.-W. Choi, A multiplex PCR assay for simultaneous detection of Escherichia coli O157: H7, Bacillus cereus, Vibrio parahaemolyticus, Salmonella spp., Listeria monocytogenes, and Staphylococcus aureus in Korean ready-to-eat food, Foodborne pathogens and disease, 11 (2014) 574-580.
[19] Y. Zhao, H. Wang, P. Zhang, C. Sun, X. Wang, X. Wang, R. Yang, C. Wang, L. Zhou, Rapid multiplex detection of 10 foodborne pathogens with an up-converting phosphor technology-based 10-channel lateral flow assay, Scientific reports, 6 (2016) 21342.
[20] P.C. Woo, S.K. Lau, J.L. Teng, H. Tse, K.-Y. Yuen, Then and now: use of 16S rDNA gene sequencing for bacterial identification and discovery of novel bacteria in clinical microbiology laboratories, Clinical Microbiology and Infection, 14 (2008) 908-934.
[21] F. Balloux, O.B. Brynildsrud, L. Van Dorp, L.P. Shaw, H. Chen, K.A. Harris, H. Wang, V. Eldholm, From theory to practice: translating whole-genome sequencing (WGS) into the clinic, Trends in microbiology, 26 (2018) 1035-1048.
[22] W. Li, D. Raoult, P.-E. Fournier, Bacterial strain typing in the genomic era, FEMS microbiology reviews, 33 (2009) 892-916.
[23] R.H. Deurenberg, E. Bathoorn, M.A. Chlebowicz, N. Couto, M. Ferdous, S. García-Cobos, A.M. Kooistra-Smid, E.C. Raangs, S. Rosema, A.C. Veloo, Application of next generation sequencing in clinical microbiology and infection prevention, Journal of biotechnology, 243 (2017) 16-24.
[24] R.A. Everley, T.M. Mott, S.A. Wyatt, D.M. Toney, T.R. Croley, Liquid Chromatography/Mass Spectrometry Characterization of Escherichia coli and Shigella Species, Journal of the American Society for Mass Spectrometry, 19 (2008) 1621-1628.
[25] N. Singhal, M. Kumar, P.K. Kanaujia, J.S. Virdi, MALDI-TOF mass spectrometry: an emerging technology for microbial identification and diagnosis, Frontiers in microbiology, 6 (2015) 791.
[26] C.K. Fagerquist, B.R. Garbus, W.G. Miller, K.E. Williams, E. Yee, A.H. Bates, S. Boyle, L.A. Harden, M.B. Cooley, R.E. Mandrell, Rapid identification of protein biomarkers of Escherichia coli O157: H7 by matrix-assisted laser desorption ionization-time-of-flight− time-of-flight mass spectrometry and top-down proteomics, Analytical chemistry, 82 (2010) 2717-2725.
[27] B. Fuchs, R. Süß, J. Schiller, An update of MALDI-TOF mass spectrometry in lipid research, Progress in lipid research, 49 (2010) 450-475.
[28] W. Yan, J. Qian, Y. Ge, K. Ye, C. Zhou, H. Zhang, Principal component analysis of MALDI-TOF MS of whole-cell foodborne pathogenic bacteria, Analytical biochemistry, 592 (2020) 113582.
[29] X. Xu, N. Xiao, M. Yang, Y. Su, Y. Guo, Discrimination of the microbial subspecies using the ribosomal protein spectra coupled with the metabolite high resolution mass spectra, Talanta, 208 (2020) 120361.

[30] A.E. Clark, E.J. Kaleta, A. Arora, D.M. Wolk, Matrix-assisted laser desorption ionization–time of flight mass spectrometry: a fundamental shift in the routine practice of clinical microbiology, Clinical microbiology reviews, 26 (2013) 547-603.
[31] D.C. Marko, R.T. Saffert, S.A. Cunningham, J. Hyman, J. Walsh, S. Arbefeville, W. Howard, J. Pruessner, N. Safwat, F.R. Cockerill, Evaluation of the Bruker Biotyper and Vitek MS matrix-assisted laser desorption ionization–time of flight mass spectrometry systems for identification of nonfermenting Gram-negative bacilli isolated from cultures from cystic fibrosis patients, Journal of clinical microbiology, 50 (2012) 2034-2039.
[32] T.R. Sandrin, J.E. Goldstein, S. Schumaker, MALDI TOF MS profiling of bacteria at the strain level: a review, Mass spectrometry reviews, 32 (2013) 188-217.
[33] A. Freiwald, S. Sauer, Phylogenetic classification and identification of bacteria by mass spectrometry, Nature protocols, 4 (2009) 732-742.
[34] B. Feng, H. Shi, F. Xu, F. Hu, J. He, H. Yang, C. Ding, W. Chen, S. Yu, FTIR-assisted MALDI-TOF MS for the identification and typing of bacteria, Anal Chim Acta, 1111 (2020) 75-82.
[35] E.M. Berendsen, E. Levin, R. Braakman, D.v. der Riet-van Oeveren, N.J. Sedee, A. Paauw, Identification of microorganisms grown in blood culture flasks using liquid chromatography–tandem mass spectrometry, Future Microbiology, 12 (2017) 1135-1145.
[36] S.N. Jackson, M. Ugarov, T. Egan, J.D. Post, D. Langlais, J. Albert Schultz, A.S. Woods, MALDI-ion mobility-TOFMS imaging of lipids in rat brain tissue, Journal of Mass Spectrometry, 42 (2007) 1093-1098.
[37] D. Oros, M. Ceprnja, J. Zucko, M. Cindric, A. Hozic, J. Skrlin, K. Barisic, E. Melvan, K. Uroic, B. Kos, Identification of pathogens from native urine samples by MALDI-TOF/TOF tandem mass spectrometry, Clinical proteomics, 17 (2020) 1-9.
[38] C.K. Fagerquist, B.R. Garbus, W.G. Miller, K.E. Williams, E. Yee, A.H. Bates, S. Boyle, L.A. Harden, M.B. Cooley, R.E. Mandrell, Rapid Identification of Protein Biomarkers of Escherichia coli O157:H7 by Matrix-Assisted Laser Desorption Ionization-Time-of-Flight-Time-of-Flight Mass Spectrometry and Top-Down Proteomics, Analytical Chemistry, 82 (2010) 2717-2725.
[39] D. Oursel, C. Loutelier-Bourhis, N. Orange, S. Chevalier, V. Norris, C.M. Lange, Lipid composition of membranes of Escherichia coli by liquid chromatography/tandem mass spectrometry using negative electrospray ionization, Rapid Communications in Mass Spectrometry, 21 (2007) 1721-1728.
[40] T.L. Williams, S.R. Monday, S. Edelson-Mammel, R. Buchanan, S.M. Musser, A top-down proteomics approach for differentiating thermal resistant strains of Enterobacter sakazakii, PROTEOMICS, 5 (2005) 4161-4169.
[41] T.L. Williams, S.R. Monday, P.C. Feng, S.M. Musser, Identifying new PCR targets for pathogenic bacteria using top-down LC/MS protein discovery, J Biomol Tech, 16 (2005) 134-142.
[42] T.L. Williams, S.M. Musser, J.L. Nordstrom, A. DePaola, S.R. Monday, Identification of a protein biomarker unique to the pandemic O3 : K6 clone of Vibrio parahaemolyticus, Journal of Clinical Microbiology, 42 (2004) 1657-1665.
[43] N. Almasoud, Y. Xu, D.K. Trivedi, S. Salivo, T. Abban, N.J.W. Rattray, E. Szula, H. Alrabiah, A. Sayqal, R. Goodacre, Classification of Bacillus and Brevibacillus species using rapid analysis of lipids by mass spectrometry, Analytical and Bioanalytical Chemistry, 408 (2016) 7865-7878.

[44] H. Chen, G. Gamez, R. Zenobi, What can we learn from ambient ionization techniques?, Journal of the American Society for Mass Spectrometry, 20 (2011) 1947-1963.
[45] C.L. Feider, A. Krieger, R.J. Dehoog, L.S. Eberlin, Ambient Ionization Mass Spectrometry: Recent Developments and Applications, Anal Chem, 91 (2019) 4266-4290.
[46] S. Rankin-Turner, J.C. Reynolds, M.A. Turner, L.M. Heaney, Applications of ambient ionization mass spectrometry in 2021: An annual review, Analytical Science Advances, 3 (2022) 67-89.
[47] Y. Song, N. Talaty, W.A. Tao, Z. Pan, R.G. Cooks, Rapid ambient mass spectrometric profiling of intact, untreated bacteria using desorption electrospray ionization, Chem. Commun., (2007) 61-63.
[48] J.I. Zhang, A.B. Costa, W.A. Tao, R.G. Cooks, Direct detection of fatty acid ethyl esters using low temperature plasma (LTP) ambient ionization mass spectrometry for rapid bacterial differentiation, Analyst, 136 (2011) 3091-3097.
[49] S.N. Nguyen, A.V. Liyu, R.K. Chu, C.R. Anderton, J. Laskin, Constant-distance mode nanospray desorption electrospray ionization mass spectrometry imaging of biological samples with complex topography, Analytical chemistry, 89 (2017) 1131-1137.
[50] C.-C. Hsu, M.S. ElNaggar, Y. Peng, J. Fang, L.M. Sanchez, S.J. Mascuch, K.A. Møller, E.K. Alazzeh, J. Pikula, R.A. Quinn, Real-time metabolomics on living microorganisms using ambient electrospray ionization flow-probe, Analytical chemistry, 85 (2013) 7014-7018.
[51] N. Strittmatter, E.A. Jones, K.A. Veselkov, M. Rebec, J.G. Bundy, Z. Takats, Analysis of intact bacteria using rapid evaporative ionisation mass spectrometry, Chemical communications, 49 (2013) 6188-6190.
[52] H. Li, P. Balan, A. Vertes, Molecular imaging of growth, metabolism, and antibiotic inhibition in bacterial colonies by laser ablation electrospray ionization mass spectrometry, Angewandte Chemie, 128 (2016) 15259-15263.
[53] A.M. Hamid, A.K. Jarmusch, V. Pirro, D.H. Pincus, B.G. Clay, G. Gervasi, R.G. Cooks, Rapid discrimination of bacteria by paper spray mass spectrometry, Anal Chem, 86 (2014) 7500-7507.
[54] K.S. Kerian, A.K. Jarmusch, R.G. Cooks, Touch spray mass spectrometry for in situ analysis of complex samples, Analyst, 139 (2014) 2714-2720.
[55] C.Y. Pierce, J.R. Barr, R.B. Cody, R.F. Massung, A.R. Woolfitt, H. Moura, H.A. Thompson, F.M. Fernandez, Ambient generation of fatty acid methyl ester ions from bacterial whole cells by direct analysis in real time (DART) mass spectrometry, Chemical Communications, (2007) 807-809.
[56] J.I. Zhang, N. Talaty, A.B. Costa, Y. Xia, W.A. Tao, R. Bell, J.H. Callahan, R.G. Cooks, Rapid direct lipid profiling of bacteria using desorption electrospray ionization mass spectrometry, International Journal of Mass Spectrometry, 301 (2011) 37-44.
[57] A.M. Hamid, P. Wei, A.K. Jarmusch, V. Pirro, R.G. Cooks, Discrimination of Candida species by paper spray mass spectrometry, International Journal of Mass Spectrometry, 378 (2015) 288-293.
[58] C.L. Feider, N. Elizondo, L.S. Eberlin, Ambient ionization and FAIMS mass spectrometry for enhanced imaging of multiply charged molecular ions in biological tissues, Analytical chemistry, 88 (2016) 11533-11541.
[59] N.E. Manicke, M. Belford, Separation of Opiate Isomers Using Electrospray Ionization and Paper Spray Coupled to High-Field Asymmetric Waveform Ion Mobility Spectrometry, Journal of The American Society for Mass Spectrometry, 26 (2015) 701-705.

[60] H. Borsdorf, T. Mayer, M. Zarejousheghani, G.A. Eiceman, Recent Developments in Ion Mobility Spectrometry, Applied Spectroscopy Reviews, 46 (2011) 472-521.
[61] R.L. Griffiths, A. Dexter, A.J. Creese, H.J. Cooper, Liquid extraction surface analysis field asymmetric waveform ion mobility spectrometry mass spectrometry for the analysis of dried blood spots, Analyst, 140 (2015) 6879-6885.
[62] E.S. Rivera, K.V. Djambazova, E.K. Neumann, R.M. Caprioli, J.M. Spraggins, Integrating ion mobility and imaging mass spectrometry for comprehensive analysis of biological tissues: A brief review and perspective, Journal of Mass Spectrometry, 55 (2020) e4614.
[63] T. Luzzatto-Knaan, A.V. Melnik, P.C. Dorrestein, Mass spectrometry tools and workflows for revealing microbial chemistry, Analyst, 140 (2015) 4949-4966.
[64] W. Cao, S. Cheng, J. Yang, J. Feng, W. Zhang, Z. Li, Q. Chen, Y. Xia, Z. Ouyang, X. Ma, Large-scale lipid analysis with C= C location and sn-position isomer resolving power, Nat Commun, 11 (2020) 1-11.
[65] D. Oursel, C. Loutelier-Bourhis, N. Orange, S. Chevalier, V. Norris, C.M. Lange, Lipid composition of membranes ofEscherichia coli by liquid chromatography/tandem mass spectrometry using negative electrospray ionization, Rapid Communications in Mass Spectrometry, 21 (2007) 1721-1728.
[66] D. Unsihuay, P. Su, H. Hu, J. Qiu, S. Kuang, Y. Li, X. Sun, S.K. Dey, J. Laskin, Imaging and Analysis of Isomeric Unsaturated Lipids through Online Photochemical Derivatization of Carbon-Carbon Double Bonds*, Angew Chem Int Ed Engl, 60 (2021) 7559-7563.
[67] B.L. Poad, X. Zheng, T.W. Mitchell, R.D. Smith, E.S. Baker, S.J. Blanksby, Online ozonolysis combined with ion mobility-mass spectrometry provides a new platform for lipid isomer analyses, Analytical chemistry, 90 (2018) 1292-1300.
[68] W. Cao, S. Cheng, J. Yang, J. Feng, W. Zhang, Z. Li, Q. Chen, Y. Xia, Z. Ouyang, X. Ma, Large-scale lipid analysis with C=C location and sn-position isomer resolving power, Nature Communications, 11 (2020).
[69] L. Liu, Z. Wang, Q. Zhang, Y. Mei, L. Li, H. Liu, Z. Wang, L. Yang, Ion Mobility Mass Spectrometry for the Separation and Characterization of Small Molecules, Analytical Chemistry, 95 (2023) 134-151.
[70] A.L. Rister, E.D. Dodds, Liquid chromatography-ion mobility spectrometry-mass spectrometry analysis of multiple classes of steroid hormone isomers in a mixture, Journal of Chromatography B, 1137 (2020) 121941.
[71] J.N. Dodds, E.S. Baker, Ion mobility spectrometry: fundamental concepts, instrumentation, applications, and the road ahead, Journal of the American Society for Mass Spectrometry, 30 (2019) 2185-2195.
[72] T. Li, Y. Yin, Z. Zhou, J. Qiu, W. Liu, X. Zhang, K. He, Y. Cai, Z.-J. Zhu, Ion mobility-based sterolomics reveals spatially and temporally distinctive sterol lipids in the mouse brain, Nat Commun, 12 (2021) 4343.
[73] M. Kliman, J.C. May, J.A. McLean, Lipid analysis and lipidomics by structurally selective ion mobility-mass spectrometry, Biochimica et Biophysica Acta (BBA)-Molecular and Cell Biology of Lipids, 1811 (2011) 935-945.
[74] K.Y. Kartowikromo, O.E. Olajide, A.M. Hamid, Collision cross section measurement and prediction methods in omics, Journal of Mass Spectrometry, 58 (2023) e4973.
[75] O.E. Olajide, K.Y. Kartowikromo, A.M. Hamid, Ion Mobility Mass Spectrometry: Instrumentation and Applications, (2023).

[76] A. Technologies, Agilent 1290 Infinity LC system: System Manual and Quick Reference, 2012.
[77] O.E. Olajide, Y. Yi, J. Zheng, A.M. Hamid, Strain-Level Discrimination of Bacteria by Liquid Chromatography and Paper Spray Ion Mobility Mass Spectrometry, Journal of the American Society for Mass Spectrometry, (2023).
[78] A. Mack, Retaining and Separating Polar Molecules - A Detailed Investigation of When to Use HILIC Versus a Reveresed-Phase Column, in: Small Molecule Pharma, 2019.
[79] A. Technologies, Agilent 6200 Series TOF and 6500 Series Q-TOF LC/MS System, in, 2017.
[80] M. Wilm, Principles of electrospray ionization, Molecular & cellular proteomics, 10 (2011).
[81] M.-N. Li, B.-Q. Shen, X. Lu, W. Gao, S.-S. Wen, X. Zhang, H. Yang, P. Li, An integrated two-step filtering strategy of collision cross-section interval predicting and mass defect filtering for targeted identification of analogues in herbal medicines using liquid chromatography-ion mobility-mass spectrometry, Journal of Chromatography A, 1657 (2021) 462572.
[82] F. Fenaille, P.B. Saint-Hilaire, K. Rousseau, C. Junot, Data acquisition workflows in liquid chromatography coupled to high resolution mass spectrometry-based metabolomics: Where do we stand?, Journal of Chromatography a, 1526 (2017) 1-12.
[83] Z. Zhou, J. Tu, Z.-J. Zhu, Advancing the large-scale CCS database for metabolomics and lipidomics at the machine-learning era, Current Opinion in Chemical Biology, 42 (2018) 34-41.
[84] S.M. Stow, T.J. Causon, X. Zheng, R.T. Kurulugama, T. Mairinger, J.C. May, E.E. Rennie, E.S. Baker, R.D. Smith, J.A. McLean, An interlaboratory evaluation of drift tube ion mobility–mass spectrometry collision cross section measurements, Analytical chemistry, 89 (2017) 9048-9055.
[85] S.M. Stow, T.J. Causon, X. Zheng, R.T. Kurulugama, T. Mairinger, J.C. May, E.E. Rennie, E.S. Baker, R.D. Smith, J.A. McLean, S. Hann, J.C. Fjeldsted, An Interlaboratory Evaluation of Drift Tube Ion Mobility–Mass Spectrometry Collision Cross Section Measurements, Analytical Chemistry, 89 (2017) 9048-9055.
[86] O.E. Olajide, B. Donkor, A.M. Hamid, Systematic Optimization of Ambient Ionization Ion Mobility Mass Spectrometry for Rapid Separation of Isomers, Journal of the American Society for Mass Spectrometry, 33 (2022) 160-171.
[87] M. Frisch, G. Trucks, H. Schlegel, G. Scuseria, M. Robb, J. Cheeseman, G. Scalmani, V. Barone, G. Petersson, H. Nakatsuji, Gaussian 16, in, Gaussian, Inc. Wallingford, CT, 2016.
[88] D. Böck, A. Beuchel, R. Goddard, A. Richter, P. Imming, R.W. Seidel, Protonation sites and hydrogen bonding in mono-hydrobromide salts of two N, 4-diheteroaryl 2-aminothiazoles, Structural Chemistry, 32 (2021) 989-996.
[89] A. Halder, S. Bhattacharya, A. Datta, D. Bhattacharyya, A. Mitra, The role of N7 protonation of guanine in determining the structure, stability and function of RNA base pairs, Physical Chemistry Chemical Physics, 17 (2015) 26249-26263.
[90] I. Campuzano, M.F. Bush, C.V. Robinson, C. Beaumont, K. Richardson, H. Kim, H.I. Kim, Structural characterization of drug-like compounds by ion mobility mass spectrometry: comparison of theoretical and experimentally derived nitrogen collision cross sections, Analytical chemistry, 84 (2012) 1026-1033.
[91] V. Shrivastav, M. Nahin, C.J. Hogan, C. Larriba-Andaluz, Benchmark Comparison for a Multi-Processing Ion Mobility Calculator in the Free Molecular Regime, Journal of The American Society for Mass Spectrometry, 28 (2017) 1540-1551.

[92] S. Plimpton, Fast Parallel Algorithms for Short-Range Molecular Dynamics, Journal of Computational Physics, 117 (1995) 1-19.
[93] J.C. May, R. Knochenmuss, J.C. Fjeldsted, J.A. McLean, Resolution of isomeric mixtures in ion mobility using a combined demultiplexing and peak deconvolution technique, Anal Chem, 92 (2020) 9482-9492.
[94] A. Bilbao, B.C. Gibbons, S.M. Stow, J.E. Kyle, K.J. Bloodsworth, S.H. Payne, R.D. Smith, Y.M. Ibrahim, E.S. Baker, J.C. Fjeldsted, A preprocessing tool for enhanced ion mobility–mass spectrometry-based omics workflows, Journal of proteome research, 21 (2021) 798-807.
[95] J.N. Dodds, E.S. Baker, Improving the Speed and Selectivity of Newborn Screening Using Ion Mobility Spectrometry–Mass Spectrometry, Anal Chem, 93 (2021) 17094-17102.
[96] G.W. Vandergrift, A.J. Hessels, J. Palaty, E.T. Krogh, C.G. Gill, Paper spray mass spectrometry for the direct, semi-quantitative measurement of fentanyl and norfentanyl in complex matrices, Clinical Biochemistry, 54 (2018) 106-111.
[97] R. Jett, C. Skaggs, N.E. Manicke, Drug screening method development for paper spray coupled to a triple quadrupole mass spectrometer, Analytical Methods, 9 (2017) 5037-5043.
[98] J.A. Michely, M.R. Meyer, H.H. Maurer, Paper Spray Ionization Coupled to High Resolution Tandem Mass Spectrometry for Comprehensive Urine Drug Testing in Comparison to Liquid Chromatography-Coupled Techniques after Urine Precipitation or Dried Urine Spot Workup, Anal Chem, 89 (2017) 11779-11786.
[99] R.G. Cooks, A.M. Hamid, A.K. Jarmusch, Z. Ouyang, Mass spectrometry analysis of microorganisms in samples, in, Google Patents, 2014.
[100] R.-Z. Shi, E.T.M. El Gierari, J.D. Faix, N.E. Manicke, Rapid Measurement of Cyclosporine and Sirolimus in Whole Blood by Paper Spray–Tandem Mass Spectrometry, Clinical Chemistry, 62 (2016) 295-297.
[101] I. Pereira, S.R.M. Rodrigues, T.C. De Carvalho, V.V. Carvalho, G.S. Lobón, J.F.P. Bassane, E. Domingos, W. Romão, R. Augusti, B.G. Vaz, Rapid screening of agrochemicals by paper spray ionization and leaf spray mass spectrometry: which technique is more appropriate?, Analytical Methods, 8 (2016) 6023-6029.
[102] Y.-C. Huang, H.-H. Chung, E.P. Dutkiewicz, C.-L. Chen, H.-Y. Hsieh, B.-R. Chen, M.-Y. Wang, C.-C. Hsu, Predicting Breast Cancer by Paper Spray Ion Mobility Spectrometry Mass Spectrometry and Machine Learning, Analytical Chemistry, 92 (2020) 1653-1657.
[103] T. Zargar, T. Khayamian, M.T. Jafari, Aptamer-modified carbon nanomaterial based sorption coupled to paper spray ion mobility spectrometry for highly sensitive and selective determination of methamphetamine, Microchimica Acta, 185 (2018).
[104] M. Li, J. Zhang, J. Jiang, J. Zhang, J. Gao, X. Qiao, Rapid, in situ detection of cocaine residues based on paper spray ionization coupled with ion mobility spectrometry, The Analyst, 139 (2014) 1687.
[105] T.K. Zargar, T., Jafari, M. T., Immobilized aptamer paper spray ionization source for ion mobility spectrometry. , Journal of Pharmaceutical and Biomedical Analysis (2017) 232-237.
[106] G. Greco, Boltner, A., Letzel, T., Agilent 1260 Infinity Analytical SFC system with Agilent 6230 ESI-TOF-MS. Optimization of Jet Stream ESI parameters. Pub Num 5991-4510EN, in, 2014.
[107] M. Wleklinski, Y. Li, S. Bag, D. Sarkar, R. Narayanan, T. Pradeep, R.G. Cooks, Zero Volt Paper Spray Ionization and Its Mechanism, Anal Chem, 87 (2015) 6786-6793.

[108] D. Kim, J. Lee, B. Kim, S. Kim, Optimization and Application of Paper-Based Spray Ionization Mass Spectrometry for Analysis of Natural Organic Matter, Anal Chem, 90 (2018) 12027-12034.
[109] J.W. Deng, Y.Y. Yang, Chemical fingerprint analysis for quality assessment and control of Bansha herbal tea using paper spray mass spectrometry, Analytica Chimica Acta, 785 (2013) 82-90.
[110] Y. Cao, G. Huang, A facile approach to improve the spray time and stability of paper spray ionization mass spectrometry with a Teflon tube, Analytical Methods, 10 (2018) 5540-5546.
[111] L. Chytil, B. Štrauch, J. Cvačka, V. Marešová, J. Widimský Jr, R. Holaj, O. Slanař, Determination of doxazosin and verapamil in human serum by fast LC–MS/MS: Application to document non-compliance of patients, Journal of Chromatography B, 878 (2010) 3167-3173.
[112] D. Baviskar, R. Sharma, D. Jain, Determination of Verapamil in Human Plasma by Tandem Mass Spectrometry, Asian J Chem, 21 (2009) 6785-6791.
[113] C.Y. Zhu, M.M. Wan, H.L. Cheng, H. Wang, M.S. Zhu, C.S. Wu, Rapid detection and structural characterization of verapamil metabolites in rats by UPLC-MSE and UNIFI platform, Biomed Chromatogr, 34 (2020).
[114] J.C. May, J.A. McLean, A Comprehensive Ion Mobility Characterization of Calibration Compounds Used in Mass Spectrometry, in: 66th Annual ASMS Conference on Mass Spectrometry, San Diego, CA, June 2018.
[115] R. Lai, E.D. Dodds, H. Li, Molecular dynamics simulation of ion mobility in gases, The Journal of Chemical Physics, 148 (2018) 064109.
[116] K.M. Hines, D.H. Ross, K.L. Davidson, M.F. Bush, L. Xu, Large-Scale Structural Characterization of Drug and Drug-Like Compounds by High-Throughput Ion Mobility-Mass Spectrometry, Anal Chem, 89 (2017) 9023-9030.
[117] Z.W. Zhou, J. Tu, X. Xiong, X.T. Shen, Z.J. Zhu, LipidCCS: Prediction of Collision Cross-Section Values for Lipids with High Precision To Support Ion Mobility-Mass Spectrometry-Based Lipidomics, Analytical Chemistry, 89 (2017) 9559-9566.
[118] S.S. Bird, V.R. Marur, I.G. Stavrovskaya, B.S. Kristal, Separation of Cis-Trans Phospholipid Isomers Using Reversed Phase LC with High Resolution MS Detection, Anal Chem, 84 (2012) 5509-5517.
[119] C.W. Damen, G. Isaac, J. Langridge, T. Hankemeier, R.J. Vreeken, Enhanced lipid isomer separation in human plasma using reversed-phase UPLC with ion-mobility/high-resolution MS detection, J Lipid Res, 55 (2014) 1772-1783.
[120] K. Jeanne Dit Fouque, C.E. Ramirez, R.L. Lewis, J.P. Koelmel, T.J. Garrett, R.A. Yost, F. Fernandez-Lima, Effective Liquid Chromatography–Trapped Ion Mobility Spectrometry–Mass Spectrometry Separation of Isomeric Lipid Species, Analytical Chemistry, 91 (2019) 5021-5027.
[121] A. Bauer, J. Kuballa, S. Rohn, E. Jantzen, J. Luetjohann, Evaluation and validation of an ion mobility quadrupole time-of-flight mass spectrometry pesticide screening approach, Journal of Separation Science, 41 (2018) 2178-2187.
[122] L. Yetukuri, M. Katajamaa, G. Medina-Gomez, T. Seppanen-Laakso, A. Vidal-Puig, M. Oresic, Bioinformatics strategies for lipidomics analysis: characterization of obesity related hepatic steatosis, Bmc Syst Biol, 1 (2007).
[123] R.J. Perry, V.T. Samuel, K.F. Petersen, G.I. Shulman, The role of hepatic lipids in hepatic insulin resistance and type 2 diabetes, Nature, 510 (2014) 84-91.
[124] T. M Jeitner, I. Voloshyna, A. B Reiss, Oxysterol derivatives of cholesterol in neurodegenerative disorders, Current medicinal chemistry, 18 (2011) 1515-1525.

[125] C.W.N. Damen, G. Isaac, J. Langridge, T. Hankemeier, R.J. Vreeken, Enhanced lipid isomer separation in human plasma using reversed-phase UPLC with ion-mobility/high-resolution MS detection, Journal of Lipid Research, 55 (2014) 1772-1783.
[126] J.E. Kyle, X. Zhang, K.K. Weitz, M.E. Monroe, Y.M. Ibrahim, R.J. Moore, J. Cha, X. Sun, E.S. Lovelace, J. Wagoner, S.J. Polyak, T.O. Metz, S.K. Dey, R.D. Smith, K.E. Burnum-Johnson, E.S. Baker, Uncovering biologically significant lipid isomers with liquid chromatography, ion mobility spectrometry and mass spectrometry, The Analyst, 141 (2016) 1649-1659.
[127] X. Zheng, N.A. Aly, Y. Zhou, K.T. Dupuis, A. Bilbao, Vanessa, D.J. Orton, R. Wilson, S.H. Payne, R.D. Smith, E.S. Baker, A structural examination and collision cross section database for over 500 metabolites and xenobiotics using drift tube ion mobility spectrometry, Chem. Sci., 8 (2017) 7724-7736.
[128] R.L. Griffiths, A.J. Creese, A.M. Race, J. Bunch, H.J. Cooper, LESA FAIMS mass spectrometry for the spatial profiling of proteins from tissue, Analytical chemistry, 88 (2016) 6758-6766.
[129] E.S. Baker, K. Tang, W.F. Danielson, D.C. Prior, R.D. Smith, Simultaneous fragmentation of multiple ions using IMS drift time dependent collision energies, Journal of the American Society for Mass Spectrometry, 19 (2008) 411-419.
[130] W. Niessen, Group-specific fragmentation of pesticides and related compounds in liquid chromatography–tandem mass spectrometry, Journal of Chromatography A, 1217 (2010) 4061-4070.
[131] E. Gikas, N.G. Papadopoulos, F.N. Bazoti, G. Zalidis, A. Tsarbopoulos, Use of liquid chromatography/electrospray ionization tandem mass spectrometry to study the degradation pathways of terbuthylazine (TER) by Typha latifolia in constructed wetlands: identification of a new TER metabolite, Rapid Communications in Mass Spectrometry, 26 (2012) 181-188.
[132] A.-M. Svennerholm, J. Holmgren, Identification ofEscherichia coli heat-labile enterotoxin by means of a ganglioside immunosorbent assay (GM1-ELISA) procedure, Current Microbiology, 1 (1978) 19-23.
[133] S. Mansour, Re: Prenatal diagnosis using combined quantitative fluorescent polymerase chain reaction and array comparative genomic hybridization analysis as a first-line test: results from over 1000 consecutive cases. F. Scott, K. Murphy, L. Carey, W. Greville, N. Mansfield, P. Barahona, R. Robertson and A. McLennan. Ultrasound Obstet Gynecol 2013; 41: 500-507., Ultrasound Obst Gyn, 41 (2013).
[134] E. Malinen, T. Rinttilä, K. Kajander, J. Mättö, A. Kassinen, L. Krogius, M. Saarela, R. Korpela, A. Palva, Analysis of the fecal microbiota of irritable bowel syndrome patients and healthy controls with real-time PCR, Am J Gastroenterol, 100 (2005) 373-382.
[135] Y. Wu, L. Li, Development of isotope labeling liquid chromatography–mass spectrometry for metabolic profiling of bacterial cells and its application for bacterial differentiation, Analytical chemistry, 85 (2013) 5755-5763.
[136] V. Havlicek, K. Lemr, K.A. Schug, Current trends in microbial diagnostics based on mass spectrometry, Analytical chemistry, 85 (2013) 790-797.
[137] N. Singhal, M. Kumar, P.K. Kanaujia, J.S. Virdi, MALDI-TOF mass spectrometry: an emerging technology for microbial identification and diagnosis, Frontiers in Microbiology, 6 (2015).
[138] S. Lee, K. Chintalapudi, A.K. Badu-Tawiah, Clinical Chemistry for Developing Countries: Mass Spectrometry, Annual Review of Analytical Chemistry, 14 (2021).

[139] C.J. Pulliam, P. Wei, D.T. Snyder, X. Wang, Z. Ouyang, R.M. Pielak, R.G. Cooks, Rapid discrimination of bacteria using a miniature mass spectrometer, Analyst, 141 (2016) 1633-1636.
[140] C.A. Chamberlain, V.Y. Rubio, T.J. Garrett, Strain-level differentiation of bacteria by paper spray ionization mass spectrometry, Analytical chemistry, 91 (2019) 4964-4968.
[141] A. Bilbao, B.C. Gibbons, S.M. Stow, J.E. Kyle, K.J. Bloodsworth, S.H. Payne, R.D. Smith, Y.M. Ibrahim, E.S. Baker, J.C. Fjeldsted, A Preprocessing Tool for Enhanced Ion Mobility-Mass Spectrometry-Based Omics Workflows, J Proteome Res, 21 (2022) 798-807.
[142] S. Wold, K. Esbensen, P. Geladi, Principal component analysis, Chemometrics and intelligent laboratory systems, 2 (1987) 37-52.
[143] P. Xanthopoulos, P.M. Pardalos, T.B. Trafalis, Linear discriminant analysis, in: Robust data mining, Springer, 2013, pp. 27-33.
[144] M.W. Browne, Cross-validation methods, Journal of mathematical psychology, 44 (2000) 108-132.
[145] N.T. Popovic, S.P. Kazazic, K. Bojanic, I. Strunjak-Perovic, R. Coz-Rakovac, Sample preparation and culture condition effects on MALDI-TOF MS identification of bacteria: A review, Mass Spectrom Rev, (2021).
[146] X. Pennanec, A. Dufour, D. Haras, K. Réhel, A quick and easy method to identify bacteria by matrix-assisted laser desorption/ionisation time-of-flight mass spectrometry, Rapid Communications in Mass Spectrometry, 24 (2010) 384-392.
[147] E. Carbonnelle, J.-L. Beretti, S. Cottyn, G. Quesne, P. Berche, X. Nassif, A. Ferroni, Rapid Identification of Staphylococci Isolated in Clinical Microbiology Laboratories by Matrix-Assisted Laser Desorption Ionization-Time of Flight Mass Spectrometry, Journal of Clinical Microbiology, 45 (2007) 2156-2161.
[148] N. Riboni, A. Quaranta, H.V. Motwani, N. Österlund, A. Gräslund, F. Bianchi, L.L. Ilag, Solvent-Assisted Paper Spray Ionization Mass Spectrometry (SAPSI-MS) for the Analysis of Biomolecules and Biofluids, Scientific Reports, 9 (2019).
[149] M. Abroodi, A. Bagheri, B.M. Razavizadeh, Surface Tension of Binary and Ternary Systems Containing Monoethanolamine (MEA), Water and Alcohols (Methanol, Ethanol, and Isopropanol) at 303.15 K, Journal of Chemical & Engineering Data, 65 (2020) 3173-3182.
[150] A. Badu-Tawiah, R.G. Cooks, Enhanced Ion Signals in Desorption Electrospray Ionization Using Surfactant Spray Solutions, Journal of the American Society for Mass Spectrometry, 21 (2010) 1423-1431.
[151] P. Bernat, K. Paraszkiewicz, P. Siewiera, M. Moryl, G. Płaza, J. Chojniak, Lipid composition in a strain of Bacillus subtilis, a producer of iturin A lipopeptides that are active against uropathogenic bacteria, World Journal of Microbiology and Biotechnology, 32 (2016) 157.
[152] V. Manzulli, V. Rondinone, A. Buchicchio, L. Serrecchia, D. Cipolletta, A. Fasanella, A. Parisi, L. Difato, M. Iatarola, A. Aceti, E. Poppa, F. Tolve, L. Pace, F. Petruzzi, I.D. Rovere, D.A. Raele, L. Del Sambro, L. Giangrossi, D. Galante, Discrimination of Bacillus cereus Group Members by MALDI-TOF Mass Spectrometry, Microorganisms, 9 (2021) 1202.
[153] L. Szalwinski, L.E. Gonzalez, N.M. Morato, B. Marsch, R.G. Cooks, Bacterial Growth Monitored by Two-Dimensional Tandem Mass Spectrometry, Analyst, (2022).
[154] Z. Zhou, J. Tu, X. Xiong, X. Shen, Z.-J. Zhu, LipidCCS: Prediction of Collision Cross-Section Values for Lipids with High Precision To Support Ion Mobility–Mass Spectrometry-Based Lipidomics, Analytical Chemistry, 89 (2017) 9559-9566.

[155] G. Favaro, S. Bogialli, I.M. Di Gangi, S. Nigris, E. Baldan, A. Squartini, P. Pastore, B. Baldan, Characterization of lipopeptides produced by Bacillus licheniformis using liquid chromatography with accurate tandem mass spectrometry, Rapid Communications in Mass Spectrometry, 30 (2016) 2237-2252.
[156] A. Théatre, C. Cano-Prieto, M. Bartolini, Y. Laurin, M. Deleu, J. Niehren, T. Fida, S. Gerbinet, M. Alanjary, M.H. Medema, A. Léonard, L. Lins, A. Arabolaza, H. Gramajo, H. Gross, P. Jacques, The Surfactin-Like Lipopeptides From Bacillus spp.: Natural Biodiversity and Synthetic Biology for a Broader Application Range, Frontiers in Bioengineering and Biotechnology, 9 (2021).
[157] J.A. Picache, B.S. Rose, A. Balinski, Katrina, S.D. Sherrod, J.C. May, J.A. McLean, Collision cross section compendium to annotate and predict multi-omic compound identities, Chemical Science, 10 (2019) 983-993.
[158] A. Kecskeméti, A. Bartal, B. Bóka, L. Kredics, L. Manczinger, K. Shine, N. Alharby, J. Khaled, M. Varga, C. Vágvölgyi, A. Szekeres, High-Frequency Occurrence of Surfactin Monomethyl Isoforms in the Ferment Broth of a Bacillus subtilis Strain Revealed by Ion Trap Mass Spectrometry, Molecules, 23 (2018) 2224.
[159] (CDC), National Shiga toxin-producing *Escherichia coli* (STEC) surveillance overview. Atlanta, Georgia: US Department of Health and Human Services, CDC, in, 2012.
[160] NCDHHS, *Escherichia coli (E. coli)* Infections, in, 2019, Decemeber 19.
[161] J.B. Kaper, J.P. Nataro, H.L. Mobley, Pathogenic escherichia coli, Nature reviews microbiology, 2 (2004) 123-140.
[162] E.M. Berendsen, E. Levin, R. Braakman, D. van der Riet-van Oeveren, N.J.A. Sedee, A. Paauw, Identification of microorganisms grown in blood culture flasks using liquid chromatography-tandem mass spectrometry, Future Microbiol, 12 (2017) 1135-1145.
[163] J.E. Camara, F.A. Hays, Discrimination between wild-type and ampicillin-resistant Escherichia coli by matrix-assisted laser desorption/ionization time-of-flight mass spectrometry, Analytical and Bioanalytical Chemistry, 389 (2007) 1633-1638.
[164] P. Dalgaard, T. Ross, L. Kamperman, K. Neumeyer, T.A. McMeekin, Estimation of bacterial growth rates from turbidimetric and viable count data, International journal of food microbiology, 23 (1994) 391-404.
[165] L.F. Eggers, D. Schwudke, Liquid Extraction: Folch, in: M.R. Wenk (Ed.) Encyclopedia of Lipidomics, Springer Netherlands, Dordrecht, 2016, pp. 1-6.
[166] Y.-Y. Zhang, Y.-X. Liu, Z. Zhou, D.-Y. Zhou, M. Du, B.-W. Zhu, L. Qin, Improving Lipidomic Coverage Using UPLC-ESI-Q-TOF-MS for Marine Shellfish by Optimizing the Mobile Phase and Resuspension Solvents, Journal of Agricultural and Food Chemistry, 67 (2019) 8677-8688.
[167] A. Bilbao, B.C. Gibbons, S.M. Stow, J.E. Kyle, K.J. Bloodsworth, S.H. Payne, R.D. Smith, Y.M. Ibrahim, E.S. Baker, J.C. Fjeldsted, A Preprocessing Tool for Enhanced Ion Mobility–Mass Spectrometry-Based Omics Workflows, Journal of Proteome Research, (2021).
[168] J.P. Koelmel, X. Li, S.M. Stow, M.J. Sartain, A. Murali, R. Kemperman, H. Tsugawa, M. Takahashi, V. Vasiliou, J.A. Bowden, R.A. Yost, T.J. Garrett, N. Kitagawa, Lipid Annotator: Towards Accurate Annotation in Non-Targeted Liquid Chromatography High-Resolution Tandem Mass Spectrometry (LC-HRMS/MS) Lipidomics Using a Rapid and User-Friendly Software, Metabolites, 10 (2020) 101.

[169] Y. Huang, E.D. Dodds, Ion Mobility Studies of Carbohydrates as Group I Adducts: Isomer Specific Collisional Cross Section Dependence on Metal Ion Radius, Anal Chem, 85 (2013) 9728-9735.
[170] M. Groessl, S. Graf, R. Knochenmuss, High resolution ion mobility-mass spectrometry for separation and identification of isomeric lipids, The Analyst, 140 (2015) 6904-6911.
[171] H.I. Kim, H. Kim, E.S. Pang, E.K. Ryu, L.W. Beegle, J.A. Loo, W.A. Goddard, I. Kanik, Structural Characterization of Unsaturated Phosphatidylcholines Using Traveling Wave Ion Mobility Spectrometry, Analytical Chemistry, 81 (2009) 8289-8297.
[172] J.J. Pi, X. Wu, Y.F. Feng, Fragmentation patterns of five types of phospholipids by ultra-high-performance liquid chromatography electrospray ionization quadrupole time-of-flight tandem mass spectrometry, Analytical Methods, 8 (2016) 1319-1332.
[173] K.D. Pruitt, T. Tatusova, D.R. Maglott, NCBI reference sequences (RefSeq): a curated non-redundant sequence database of genomes, transcripts and proteins, Nucleic acids research, 35 (2007) D61-D65.
[174] R.S. Kaas, P. Leekitcharoenphon, F.M. Aarestrup, O. Lund, Solving the problem of comparing whole bacterial genomes across different sequencing platforms, PloS one, 9 (2014) e104984.
[175] J.T. Shelley, G.M. Hieftje, Ionization matrix effects in plasma-based ambient mass spectrometry sources, Journal of Analytical Atomic Spectrometry, 25 (2010) 345-350.
[176] J.Y. Lim, J.W. Yoon, C.J. Hovde, A brief overview of Escherichia coli O157: H7 and its plasmid O157, Journal of microbiology and biotechnology, 20 (2010) 5.
[177] J.P. Nataro, J.B. Kaper, Diarrheagenic escherichia coli, Clinical microbiology reviews, 11 (1998) 142-201.
[178] A. Sakudo, T. Misawa, Antibiotic-resistant and non-resistant bacteria display similar susceptibility to dielectric barrier discharge plasma, International journal of molecular sciences, 21 (2020) 6326.
[179] M. Yu, H. Shi, H. Shen, X. Chen, L. Zhang, J. Zhu, G. Qian, B. Feng, S. Yu, Simple and Rapid Discrimination of Methicillin-Resistant Staphylococcus aureus Based on Gram Staining and Machine Vision, Microbiology Spectrum, 11 (2023) e05282-05222.
[180] S. Lakhundi, K. Zhang, Methicillin-resistant Staphylococcus aureus: molecular characterization, evolution, and epidemiology, Clinical microbiology reviews, 31 (2018) 10.1128/cmr. 00020-00018.
[181] A.S. Lee, H. De Lencastre, J. Garau, J. Kluytmans, S. Malhotra-Kumar, A. Peschel, S. Harbarth, Methicillin-resistant Staphylococcus aureus, Nature reviews Disease primers, 4 (2018) 1-23.
[182] O.E. Olajide, Y. Yi, J. Zheng, A.M. Hamid, Species-level discrimination of microorganisms by high-resolution paper spray–Ion mobility–Mass spectrometry, International Journal of Mass Spectrometry, 478 (2022) 116871.
[183] N. Topić Popović, S.P. Kazazić, K. Bojanić, I. Strunjak-Perović, R. Čož-Rakovac, Sample preparation and culture condition effects on MALDI-TOF MS identification of bacteria: A review, Mass spectrometry reviews, 42 (2023) 1589-1603.
[184] X. Pennanec, A. Dufour, D. Haras, K. Réhel, A quick and easy method to identify bacteria by matrix-assisted laser desorption/ionisation time-of-flight mass spectrometry, Rapid Communications in Mass Spectrometry, 24 (2010) 384-392.
[185] J.M. Carpenter, H.M. Hynds, K. Bimpeh, K.M. Hines, HILIC-IM-MS for Simultaneous Lipid and Metabolite Profiling of Bacteria, ACS Measurement Science Au, (2023).

[186] D. Janiszewska, M. Szultka-Młyńska, P. Pomastowski, B. Buszewski, “Omic” Approaches to Bacteria and Antibiotic Resistance Identification, International Journal of Molecular Sciences, 23 (2022) 9601.
[187] B.K. Sharma-Kuinkel, T.H. Rude, V.G. Fowler, Pulse field gel electrophoresis, The Genetic Manipulation of Staphylococci: Methods and Protocols, (2016) 117-130.
[188] O.E. Olajide, M. Zirpoli, J. Zheng, A.M. Hamid, Pathogenic and Non-pathogenic E. coli Strains Discrimination in Urine Samples by Liquid Chromatography - Ion Mobility - Tandem Mass Spectrometry and Machine Learning in: A. University (Ed.), 2024.
[189] P. Virtanen, R. Gommers, T.E. Oliphant, M. Haberland, T. Reddy, D. Cournapeau, E. Burovski, P. Peterson, W. Weckesser, J. Bright, SciPy 1.0: fundamental algorithms for scientific computing in Python, Nature methods, 17 (2020) 261-272.
[190] W. Luo, C. Brouwer, Pathview: an R/Bioconductor package for pathway-based data integration and visualization, Bioinformatics, 29 (2013) 1830-1831.
[191] G.J. Aroeira, M.M. Davis, J.M. Turney, H.F. Schaefer III, Fermi. jl: a modern design for quantum chemistry, Journal of chemical theory and computation, 18 (2022) 677-686.
[192] S. Kotwal, P. Rani, T. Arif, J. Manhas, S. Sharma, Automated bacterial classifications using machine learning based computational techniques: Architectures, challenges and open research issues, Archives of Computational Methods in Engineering, (2022) 1-22.
[193] M. Sans, J. Zhang, J.Q. Lin, C.L. Feider, N. Giese, M.T. Breen, K. Sebastian, J. Liu, A.K. Sood, L.S. Eberlin, Performance of the MasSpec Pen for rapid diagnosis of ovarian cancer, Clinical chemistry, 65 (2019) 674-683.
[194] L.E. Gonzalez, D.T. Snyder, H. Casey, Y. Hu, D.M. Wang, M. Guetzloff, N. Huckaby, E.T. Dziekonski, J.M. Wells, R.G. Cooks, Machine-Learning Classification of Bacteria Using Two-Dimensional Tandem Mass Spectrometry, Analytical Chemistry, 95 (2023) 17082-17088.
[195] J. Tu, Z. Zhou, T. Li, Z.-J. Zhu, The emerging role of ion mobility-mass spectrometry in lipidomics to facilitate lipid separation and identification, TrAC Trends in Analytical Chemistry, 116 (2019) 332-339.
[196] Y.M. Ibrahim, A.M. Hamid, L. Deng, S.V. Garimella, I.K. Webb, E.S. Baker, R.D. Smith, New frontiers for mass spectrometry based upon structures for lossless ion manipulations, Analyst, 142 (2017) 1010-1021.
[197] L. Deng, I.K. Webb, S.V. Garimella, A.M. Hamid, X. Zheng, R.V. Norheim, S.A. Prost, G.A. Anderson, J.A. Sandoval, E.S. Baker, Serpentine ultralong path with extended routing (SUPER) high resolution traveling wave ion mobility-MS using structures for lossless ion manipulations, Anal Chem, 89 (2017) 4628-4634.

Publications

1. Olajide, Orobola E., Yuyan Yi, Jingyi Zheng, and Ahmed M. Hamid. "Strain-Level Discrimination of Bacteria by Liquid Chromatography and Paper Spray Ion Mobility Mass Spectrometry." *Journal of the American Society for Mass Spectrometry* (2023).
2. Olajide, Orobola E., Yuyan Yi, Jingyi Zheng, and Ahmed M. Hamid. "Species-level discrimination of microorganisms by high-resolution paper spray–Ion mobility–Mass spectrometry." *International Journal of Mass Spectrometry* 478 (2022): 116871.
3. Olajide, Orobola E., Benedicta Donkor, and Ahmed M. Hamid. "Systematic optimization of ambient ionization ion mobility mass spectrometry for rapid separation of isomers." *Journal of the American Society for Mass Spectrometry* 33, no. 1 (2021): 160-171.
4. Kartowikromo, Kimberly Y., Orobola E. Olajide, and Ahmed M. Hamid. "Collision cross section measurement and prediction methods in omics." *Journal of Mass Spectrometry* 58, no. 9 (2023): e4973.
5. Olajide, Orobola E., Kimberly Y. Kartowikromo, and Ahmed M. Hamid. "Ion Mobility Mass Spectrometry: Instrumentation and Applications." (2023).
6. Olajide, Orobola E., Michael Zirpoli, Jingyi Zheng, Ahmed M. Hamid. “Pathogenic and Non-pathogenic *E. coli* Strains Discrimination in Urine Samples by Liquid Chromatography - Ion Mobility - Tandem Mass Spectrometry and Machine Learning in: A. University (Ed.), 2024.